Capacitive Resonant Single-Conductor System for Wireless Power Transfer to Devices with Metallic Embodiments

by

Susanna Vital de Campos de Freitas

A thesis submitted in partial fulfillment of the requirements for the degree of

Master of Science

in

Electromagnetics and Microwaves

Department of Electrical and Computer Engineering

University of Alberta

Abstract

Although wireless power transfer (WPT) evolved drastically over the past decades, it still strives to be widely commercialized. The most two common methods of near-field contactless power transfer - inductive and capacitive power transfer - face significant obstacles regarding the misalignment and distance between receiver and transmitter devices. Moreover, these techniques are either not able to efficiently provide power while facing a conductive obstacle, or require multiple metallic plates to work.

In order to power an electronic device with a metallic cover, a mixture of inductive, capacitive and single-conductor power transfers is proposed, being called as "Capacitive Resonant Single-Conductor". The components of the system are described, designed, simulated and measured in the scope of this thesis. The proposed technology is designed to work according to the widely accepted AirFuel standard, at 6.78 MHz. Furthermore, variations to the final system are analyzed, while discussing its limitations.

Finally, the structure's impedances are affected by load variations, objects in its vicinity and relative position between transmitter and receiver devices. Therefore, adaptive matching circuits are of interest in WPT. The proposed circuit uses a transistor to control the amount of time that a capacitor is conducting, so that the resulting capacitance between this and other components creates a variable reactance related to the transistor's base voltage. The final described adaptive matching is then applied to a regular 2-coil inductive link, to show its impact on this system's self-resonance.

Preface

This thesis contains information about a project developed by the author and another student, called Fabiano Cezar Domingos. The present thesis focuses on: planar spiral resonators, impact caused by system's variations, design of capacitive plates composed of multiple cells, and matching networks. The other student's thesis pivots around helical resonators, analysis of quality factors and losses in the system, and rectifier circuits.

Section 2.3 of this thesis has been published as F. C. Domingos, S. V. de C. de Freitas, and P. Mousavi, "Capacitive Power Transfer based on Compensation Circuit for Class E Resonant Full-Wave Rectifier," *Wireless Power Transfer Conference (WPTC), 2018 IEEE*, 2018. Fabiano received the Best Student Paper Award for this paper.

Section 2.4 of this thesis has been published as F. C. Domingos, S. V. de C. de Freitas, and P. Mousavi, "Overview of Single Conductor Power Transfer With Open-Ended Helical Resonators," *18th International Symposium on Antenna Technology and Applied Electromagnetics (ANTEM)*, 2018.

Chapter 3 of this thesis has been published as S. V. de C. de Freitas, F. C. Domingos, R. Mirzavand, and P. Mousavi, "Contactless Power Transfer Using Capacitive Resonant Single-Conductor Structure," *Wireless Power Transfer Conference (WPTC), 2018 IEEE*, 2018. The author of the present document received the Best Student Paper Award for this paper.

Additionally, a provisional patent application has been filed based on this technology: S. V. de C. de Freitas, F. C. Domingos, R. Mirzavand, and P. Mousavi, "Systems and Methods for Wireless Power Transmission", US Patent 15/745,692, filed December, 2017.

To my family

For supporting all my crazy dreams and ideas.

When you have exhausted all possibilities, remember this: you haven't.

– Thomas A. Edison.

Acknowledgements

I would like to thank my supervisor, Dr. Pedram Mousavi. His willingness to take this and other students' projects to another level, patenting and commercializing them, have made me aware of the industrial potential and impact that students can create with their researches. He always offered his support and mentorship whenever needed, which was essential to the conclusion of this project.

To my parents, Luciana Vital and Marcos de Freitas, my love and gratitude for making me who I am today. They raised me to pursue my dreams, always providing me unconditional love and support to achieve my goals, even when I decided to live half-globe away to pursue this Master's program. I would not be half of the person that I am without them.

My little sister, Amanda Vital, is always there to make my day brighter. She offered her support when I needed someone to share my struggles with, in a way that only a sister can do. She even provided me advices about my thesis, which were appreciated and paid back with laughs and action figures.

Most importantly, I want to express my love and appreciation to my husband, Fabiano Cezar Domingos, who is my partner not only in this project, but also in life. I cannot express in words how blessed I feel for being able to share my life with him. His support allows me to be my best self everyday, and I am sure we will continue to grow together, living our lives to the best.

Contents

List of Tables

List of Figures

List of Symbols

β — Current gain of a transistor

δ — Skin depth

ε — Permittivity

ε_0 — Permittivity of free space

λ — Free space wavelength

μ — Magnetic permeability

μ_0 — Magnetic permeability of free space

ρ — Resistivity

Φ — Magnetic flux

Ψ — Proximity factor

ω — Angular frequency

ω_0 — Angular frequency of free space

A_{eff} — Effective area

C — Capacitance

D — Diameter of a coil/resonator

d — Cross sectional diameter of wire used to build a coil/resonator

f_0 — Operation or center frequency

k — Coupling coefficient

L — Inductance

l — Length of wire required to build a coil/resonator

M — Mutual inductance

N — Number of turns of a coil/resonator

Q — Quality factor

R — Resistance

List of Abbreviations

AC	Alternating Current
AGM	Arithmetic-Geometric Mean
AWG	American Wire Gauge
CPT	Capacitive Power Transfer
DC	Direct Current
EMI	Electromagnetic Interference
ESR	Equivalent Series Resistance
IPT	Inductive Power Transfer
ISM	Industrial, Scientific and Medical
PCB	Printed Circuit Board
RF	Radio Frequency
SC	Single-Conductor
$SCPT$	Single-Conductor Power Transfer
$TCVC$	Transistor-Controlled Variable Capacitor
VCO	Variable-Controlled Oscillator
VNA	Vector Network Analyzer
WPT	Wireless Power Transfer

Chapter 1

Introduction

The semiconductor industry alone generated over 412 billion US dollars in revenue, in 2017 [1]. This impressive number reveals that the production of electronic devices occupies a significant portion of the global economy. Therefore, companies and researchers are devoted to improve the performance of such equipments. Throughout the years, people have struggled to minimize the size of gadgets that are present in our daily lives. The current limiter to further decrease electronic devices' dimensions is the necessity of bulky connectors and power sources or batteries attached to the equipment. A battery, for example, occupies a substantial amount of space and requires constant maintenance to be replaced. Wireless power transfer (WPT) is an interesting alternative to minimize these problems [2].

1.1   Background and Motivation

Power cords constrain the device and user's position, while portable batteries provide limited autonomy. To overcome such restrictions, two categories of WPT are highlighted: inductive power transfer (IPT) [3], [4] and capacitive power transfer (CPT) [5], [6]. However, such techniques of contactless power transfer are still striving to gain freedom regarding the alignment and distance between receiver and transmitter coils [3], [7]–[9] and plates [10], respectively. Moreover, existing WPT techniques struggle to transfer power to devices that are built within metallic cases or bodies.

In IPT, the wireless power transfer is achieved by near-field magnetic cou-

pling between two or more coils (Fig. 1.1). Even though such technique is able to efficiently transfer significant amounts of power [11], it is extremely susceptible to the position and alignment between the coils. Additionally, when a conductive obstacle (such as a metallic case, for example) is added between the coils, the efficiency drops drastically due to current being induced in the obstacle instead the receiver [12]. Furthermore, the leakage magnetic field might even heat up foreign metallic objects because of parasitic eddy currents generated in them.
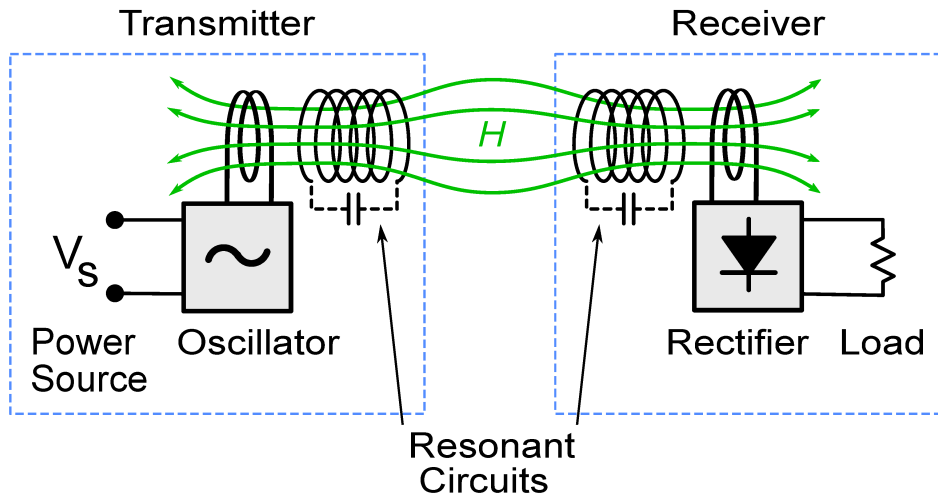
Figure 1.1: Inductive power transfer

Alternatively, CPT technology utilizes electric field coupling to transfer power between two pairs of electrodes (usually conceived as metallic plates), as in Fig. 1.2. This technique is often limited to low and medium power range, with few high power applications [13], because of the significantly large electric field intensity that it generates. Nevertheless, capacitive power transfer suffers from the same positioning problems of IPT [14], with two pairs of elements requiring correct alignment. In order to charge an electronic device with a metallic case using this technique, it would be necessary to change its design, so that the two required plates on the receiver side can be incorporated, which is usually not an appealing option to industry.

2
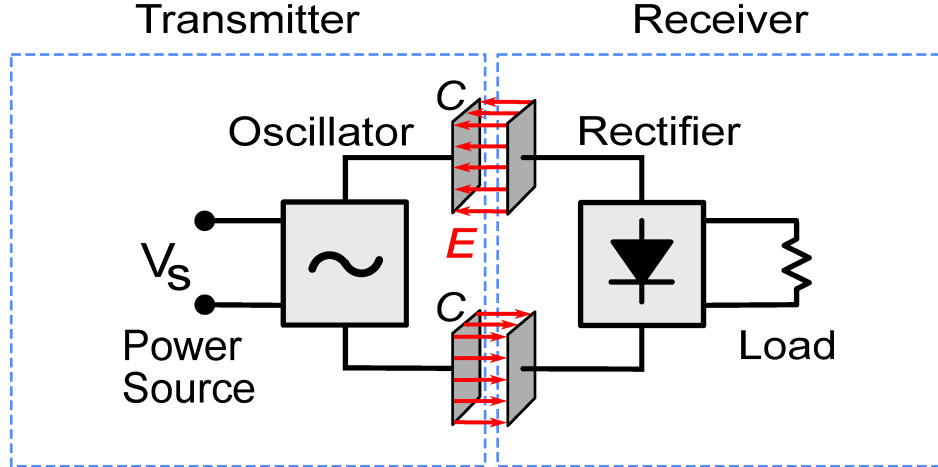
Figure 1.2: Capacitive power transfer

Moreover, research presents the single-conductor power transfer (SCPT) as an alternative solution to some of the problems that still plague IPT and CPT [15], [16]. This technique was firstly conceived as a way to excite a surface wave over a conducting structure, using massive horn launchers to excite the needed propagation mode in the structure [17], [18]. Recent approaches present another way to transfer power over the single-conductor structure: using open-ended helical resonators [15], [16], [19] to excite a standing wave in it (Fig. 1.3). This method allows efficient power transfer over a metallic structure, being of extreme interest for powering devices and sensors placed on metallic shelves, desks, or pipelines. However, if one imagine this metallic structure as the embodiment of an electronic device, it would be necessary to have one resonator inside the device, and another one outside. Such arrangement is not attractive to users, and they would still be limited to the relative position between their device and the charging unit.
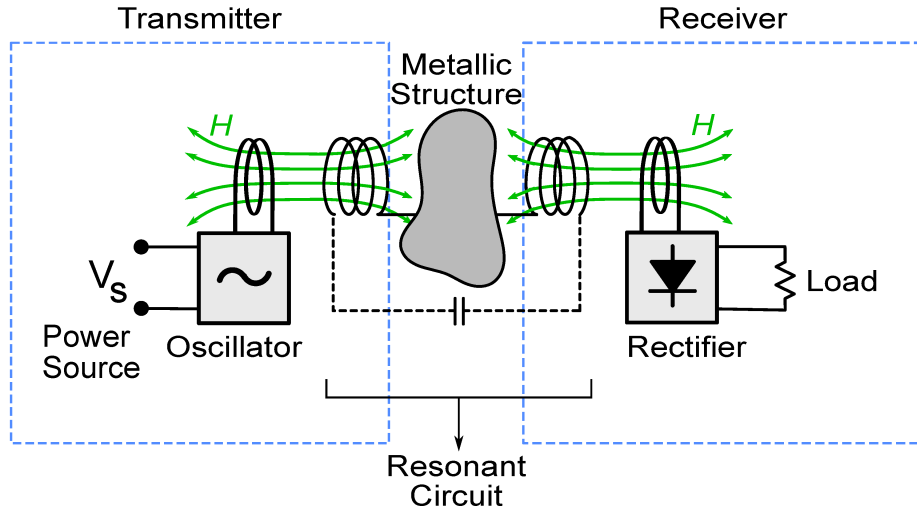
Figure 1.3: Single-conductor power transfer

Finally, in order to address the charging of devices with metallic embodiments, this thesis analyzes a new system that proposes the insertion of a discontinuity in the regular single-conductor structure (Fig. 1.4). Capacitive plates are added in the middle of the metallic structure, such that the receiver plate would be the embodiment of the electronic device, while the other plate would be in the charging unit. This addition allows the efficient power transfer to a device that possesses a metallic case by utilizing a mixture of magnetic and electric fields.
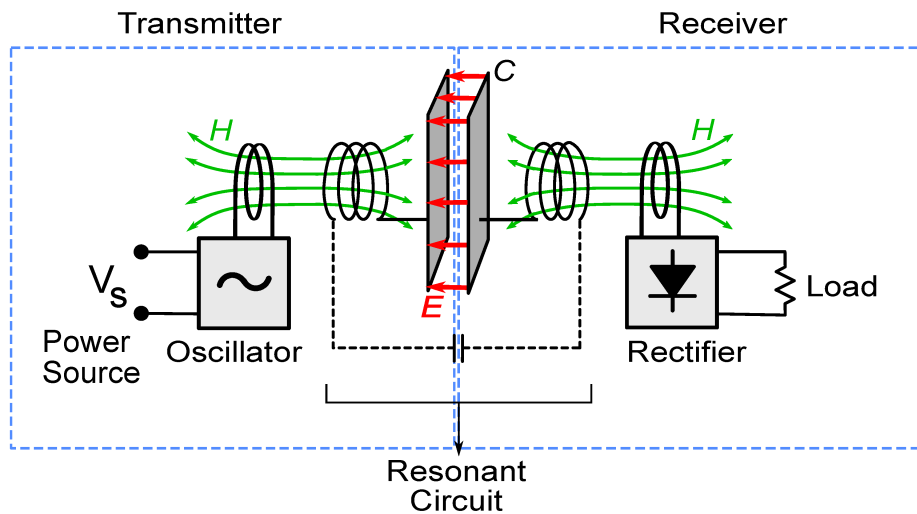
Figure 1.4: Capacitive resonant single-conductor power transfer

The proposed system requires only one pair of capacitive plates, opposing regular CPT that requires at least two pairs of electrodes. Furthermore, this approach maintains the benefits of feeding the structure using resonators, similar to SCPT. Furthermore, since there is no direct magnetic coupling between the transmitter and the receiver, and the plates do not necessarily have the same dimensions, the receiver position is only constrained by the area that the transmitter plate covers.
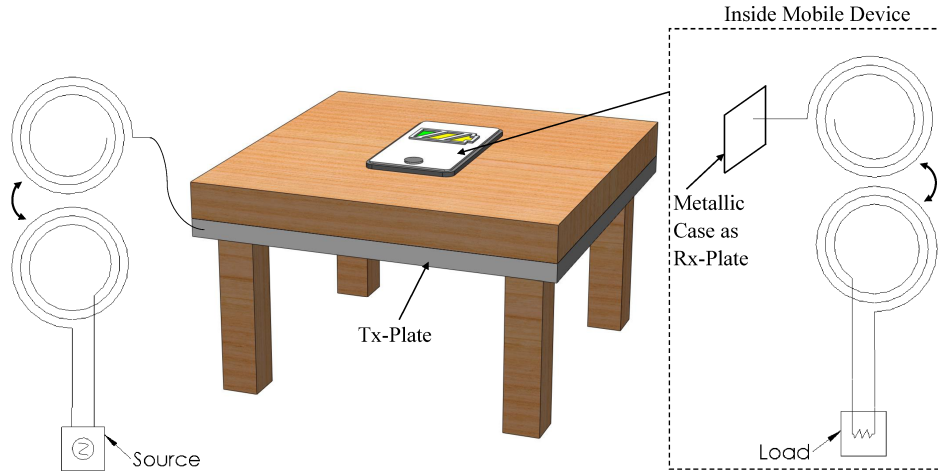
Figure 1.5: Capacitive resonant single-conductor used as a charger on a table

Fig. 1.5 illustrates a possible application of this technology. The transmitter capacitive plate covers the entire bottom side of the tabletop, so that a receiver with a metallic cover can be charged when placed anywhere on top of the furniture.

1.2 Objective

This thesis aims to design a method to efficiently transfer power to an electronic device with a metallic embodiment, using this conductive object as part of the system. In order to accomplish such goal, a mixture of IPT, CPT and SCPT is proposed.

The analysis is performed by defining the equivalent electric circuit model of the system, and by conducting simulations and measurements with the designed structure. Furthermore, the developed technology is analyzed over

different conditions, such as: variations in the matching and tuning networks, modifications in the physical dimensions of the transmitter and receiver structures, and changes in the relative position of the different parts that compose the system. Since distance between coils and resonators is of minor interest for the proposed WPT, such parameter will not be optimized.

1.3 Thesis Structure

This thesis is composed of five chapters. In Chapter 2, a general explanation of all the components of the system is presented, which includes: the coils and resonators, the capacitive plates, and the overall single-conductor. Firstly, in order to understand the concept that motivated the creation of such technology, inductive coupling is explained, justifying the chosen topology for the coils and resonators. Capacitive coupling is then studied in order to determine the capacitance between the metallic plates added to the system. Next, the single-conductor fed by open-ended resonators is presented, emphasizing its difference from single-conductor structures excited by launching horns. Moreover, the construction of each system's component is explained, and further simulated, built and measured.

The system proposed by this thesis (the single-conductor with a capacitive discontinuity) is presented in Chapter 3, uniting all the previously described concepts. The final system is simulated and measured, with the results being further analyzed.

Chapter 4 presents variations to the system described in Chapter 3, such as: the use of asymmetric capacitive plates, the implementation of multiple transmitter cells, and the variation of receiver's position on top of the transmitter.

Correct matching and tuning is essential to achieve high efficiency at the desired frequency. Generally, matching networks are used to ensure minimal reflection on the 50 Ω ports of the measurement device. However, the impedance of the system might change depending on the distance between the plates and their physical dimensions. Furthermore, different receiver devices

may provide varied load impedances. Thus, it is desirable to study an adaptive matching circuit. Chapter 5 describes the developed adaptive matching circuit, providing its impact in regular inductive power transfer.

The final conclusions obtained from this thesis are presented in Chapter 6, as well as the proposed future work and further improvements for this area of research.

Chapter 2

Theory Behind the System

This thesis presents the analysis of the addition of a discontinuity, conceived as capacitive plates, in a single-conductor structure fed by open-ended resonators. Although different papers exist about the single-conductor being excited by such structures, the new structure proposed in this thesis requires further explanation of the theoretical background and simulations. Thus, in order to appropriately add the discontinuity to the system, a proper introduction must be presented.

2.1 Inductive Power Transfer

As explained in the previous section, the chosen method to power the single-conductor is to use near-field inductive coupling. Thus, it is necessary to first analyze the inductive power transfer separately, before introducing the single-conductor structure to the system.

IPT systems work based on near-field magnetic coupling for non-radiative mid-range power transfer. There are basically three different topologies of inductive power transfer: non-resonant inductive topology, low-Q resonant inductive topology and high-Q resonant inductive topology [20].

2.1.1 Non-resonant Inductive Topology

The non-resonant IPT (Fig. 2.1) consists of at least two coils, denominated in this document as transmitter and receiver, forming together a transformer. An alternating power source generates an alternating current on the transmit-

ter coil. By Ampere's law, this alternating current generates an alternating magnetic field around the structure. This field, by Faraday's law, will induce an alternating voltage in a receiver coil that is placed in the proximity of the transmitter coil. This voltage creates an alternating current on the receiver coil, that can be rectified and transferred to a load.

Since the coils are not resonating at the frequency of the current generated by the source, the overall efficiency of the system is extremely dependent of the coupling coefficient (k) between the coils [21]. Equation (2.1) shows that this coefficient depends on the inductance of the coils (L_1 and L_2) and their mutual inductance (M).

$$k = \frac{M}{\sqrt{L_1 L_2}} \tag{2.1}$$

$$M = M_{12} = M_{21} \tag{2.2}$$

$$M_{21} = \frac{N_2 \Phi_{21}}{I_1} \tag{2.3}$$

The variable Φ_{21}, in Eq. (2.3), is the magnetic flux through one turn of the receiver coil due to the current on the transmitter coil (I_1). Therefore, the efficiency of the system depends mainly on the geometrical properties of the coils and their relative position. For example, if the distance between the coils increases, the amount of magnetic field that reaches the receiver reduces. Consequently, Φ_{21} will be smaller, reducing M and k. Thus, the non-resonant inductive topology is restricted to cases where significant distance between the coils is not necessary [22].
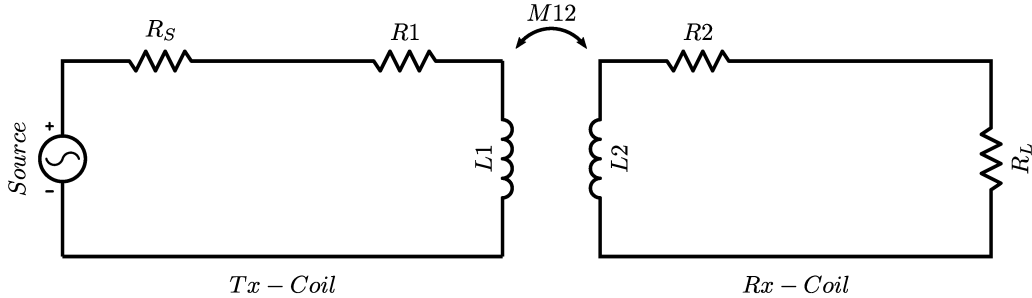
Figure 2.1: Non-resonant inductive topology

2.1.2   Low-Q Resonant Inductive Topology

This topology is similar to the previous one, but capacitors are added in series or parallel with the coils in order to create resonance at the desired frequency, following Eq. (2.4).

$$f = \frac{1}{2\pi\sqrt{L_x C_x}} \tag{2.4}$$

This approach allows increased independence from the coupling coefficient k. However, it narrows the system's frequency of operation [23]. According to [21], [23], [24], the series-parallel configuration (Fig. 2.2) of tuning capacitors provides significant advantages to improve the links efficiency.

The series capacitor on the primary side alters the voltage gain of the system, without changing the efficiency whatsoever. The addition of such capacitor increases the voltage that is applied to transmitter coil and, by consequence, proportionally increases the voltage on the receiver. However, since the ratio between received and sent power is not altered, the efficiency is kept constant. This voltage increase on the transmitter side is due to the fact that the capacitor compensates impedances added by the self-inductance of the coils, generating less losses due to the system's reactance at this particular frequency [24]. Furthermore, a series configuration creates a low impedance loading the system, which reduces losses [21]. The parallel capacitor on the secondary side changes the voltage gain and the efficiency of the system [21].

These impedances added to the system make it less sensitive to the coupling coefficient k, and more related to its resonance. Therefore, this topology is

10

extremely limited regarding the frequency of operation. In other words, it provides higher gain and efficiency for a restricted range of frequency.

Furthermore, this topology does not provide a high quality (Q) link. This happens due to the loading effect created by the source and load resistances on the primary and secondary sides of the system, respectively [25].
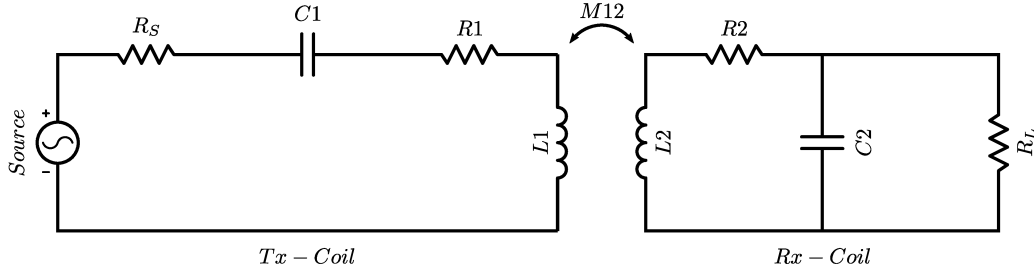
Figure 2.2: Low-Q resonant inductive topology

2.1.3   High-Q Resonant Inductive Topology

This variation of the IPT technology has at least one extra intermediate resonant circuit (denominated as resonator) between the transmitter and receiver coils of the non-resonant inductive topology from 2.1.1. As illustrated in Fig. 2.3, two resonators will be used in this thesis, when utilizing the high-Q IPT topology. This approach allows higher Q because the loading effect is minimized, since the resistance of the source and load are not in series with the resonating structures anymore [21]. Additionally, if necessary, series and parallel capacitors may be added to the Tx and Rx coils, following the explanation provided in the previous section.
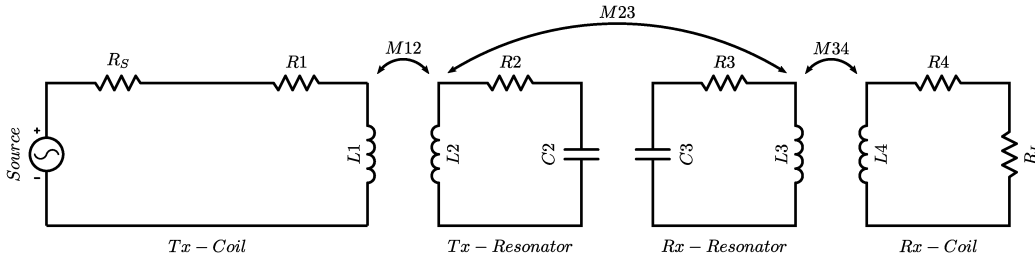
Figure 2.3: High-Q resonant inductive topology

11

2.2 4-Coil Inductive Power Transfer

Since the topology described in Section 2.1.3 allows the highest efficiency among all the presented topologies, it will be used for further studies in this section.

2.2.1 Coil Design

First, it is necessary to design the coils and resonators that are going to be used in the system. Due to physical constraints, it was decided that the maximum diameter of the feeding coils would be 10 cm, while the maximum diameter of the resonators would be 12 cm. Furthermore, since the Q factor of the coils increases if their resistance is reduced [26] (Eq. (2.5)), the coils were built with the thicker solid copper wire available for the project, which is a 16 AWG magnet wire.

$$Q = \frac{\omega L}{R} \tag{2.5}$$

The operation frequency, or center frequency, f_0 is chosen to be at 6.78 MHz, since it is one of the industrial, scientific and medical (ISM) radio bands. Furthermore, a significant portion of the WPT devices work at this frequency because of the Airfuel standard for wireless power transfer [27].

For simplicity, the coils and resonators are designed with only one turn each. Eq. (2.6) can be used to calculate their individual self-inductance (in μH) [28]. The variable D represents the diameter of the coil/resonator in millimeters, while d is the cross sectional diameter of the wire utilized to build the structures, also in millimeter.

$$L = 0.0002\pi D \left[ln\left(\frac{8D}{d}\right) - 1.75 \right] \tag{2.6}$$

Based on the previous equation, the self-inductance of the coils are $L_1 = L_4 = 0.294$ μH, while the self-inductance of the resonators are $L_2 = L_3 = 0.367$ μH. Moreover, capacitors must be added to the resonators in order to achieve resonance. From Eq. (2.4), it can be determined that the resonators require

12

capacitors of approximately $C_2 = C_3 = 1.5$ nF in order to resonate at the desired frequency.

To calculate the Q of the coils and resonators, one more parameter must be inferred: the equivalent series resistance (represented as R) of each element. This value can be calculated using Eq. (2.7) [29].

$$R = R_{AC} = \frac{\rho l}{A_{eff}} \tag{2.7}$$

$$l = 2\pi(D/2) \tag{2.8}$$

$$A_{eff} = \pi\left((d/2)^2 - \left((d/2) - \delta\right)^2\right) \tag{2.9}$$

$$\delta = \sqrt{\frac{\rho}{\pi f \mu}} \tag{2.10}$$

$$\rho_{copper} = 1.68 \times 10^{-8}[\Omega m] \quad \text{and} \quad \mu_{copper} \approx \mu_0 = 4\pi \times 10^{-7}[H/m] \tag{2.11}$$

The previous equations emphasize that the resistance of the structure must take into consideration the skin depth (δ) effect created by the AC current only flowing through the edges of the wire of diameter d [29].

Applying the previous equations, the resistances obtained for each coil and resonator are: $R_1 = R_4 = 0.0530$ Ω and $R_2 = R_3 = 0.0636$ Ω. Then, the Q factor for each structure can be calculated using Eq. 2.5: $Q_1 = Q_4 = 236.2955$ and $Q_2 = Q_3 = 245.5010$.

$$Q_C = \frac{X_C}{R_C} = \frac{1}{\omega_0 C R_C} \tag{2.12}$$

Additionally, the capacitors added to the resonators must have extremely high quality factors. From Eq. (2.12), it can be observed that a higher Q will result in less series resistance added by the capacitor to the system [29].

2.2.2 Analysis of Designed Coils

Based on the theory provided on the previous section, the details of the coils and resonators of the preliminary IPT system are provided on Table 2.1, and the measured inductive link is depicted in Fig. 2.4.

Table 2.1: Calculated parameters of designed coils and resonators for a high-Q resonant IPT system at 6.78 MHz

Parameter	Tx-Coil	Tx-Resonator	Rx-Resonator	Rx-Coil
D [mm]	100	120	120	100
d [mm]	1.29	1.29	1.29	1.29
N	1	1	1	1
L [μH]	0.294	0.367	0.367	0.294
R [Ω]	0.0530	0.0636	0.0636	0.0530
Q	236.2955	245.5010	245.5010	236.2955
C [nF]	-	1.5	1.5	-
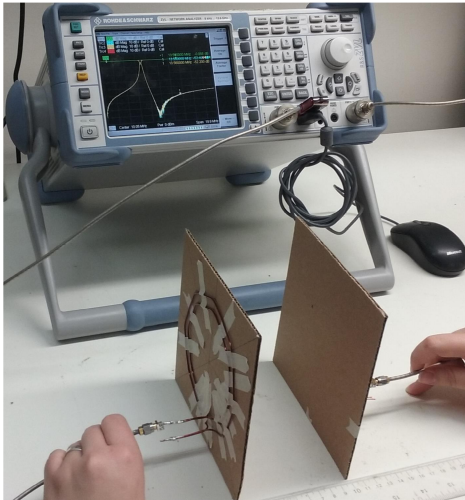
(a) Measurement of built coils and resonators
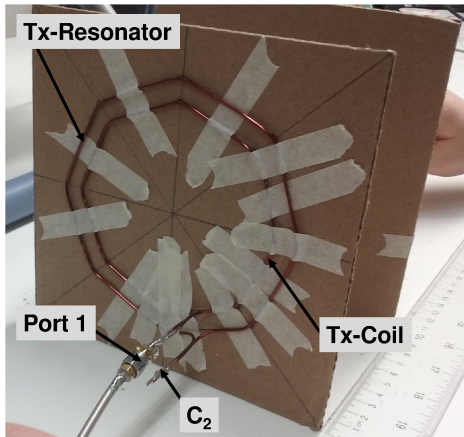
(b) Diagram explaining the measured system

Figure 2.4: Built coils and resonators

In order to obtain resonance at the desired frequency, capacitors of 1.47 nF are added to the resonators, since this is the closest commercial value available for the calculated C_2 and C_3. The chosen capacitors are RF ultra low ESR components from the company AVX RF. It was decided to use the SQCB

series of capacitors, since such components have a maximum ESR of 0.1 Ω at the desired frequency for capacitor values between 100 pF and 1000 pF [30].

Moreover, it was decided to simulate and build octagonal coils/resonators in order to reduce mesh complexity and simulation time, without significantly changing the behavior of the system [31]. Although the time saved in simulations with only the 4-coil system is not noticeable, it will significantly help in the next sections, when more complex structures are attached to the coils. Additionally, it is easier to shape and center polygons instead of circles when the coils and resonators are physically built.

Such system will be used as the beginning of this study. Several simulations and measurements are performed with the designed coils/resonators. All electromagnetic simulations were obtained in the software Ansys HFSS using the driven modal solution. Meshing was performed using mixed-order basis functions and minimum eight consecutive adaptive passes after convergence. The measurements were performed using a calibrated Rohde&Schwarz ZVL13 Vector Network Analyzer (VNA).

First, the performance of the coils and resonators is analyzed according to the distance between transmitter and receiver structures. Fig. 2.5 contains the simulation results obtained by varying the distance between the transmitter and receiver structures, while maintaining the capacitance of both resonators fixed at 1470 pF.
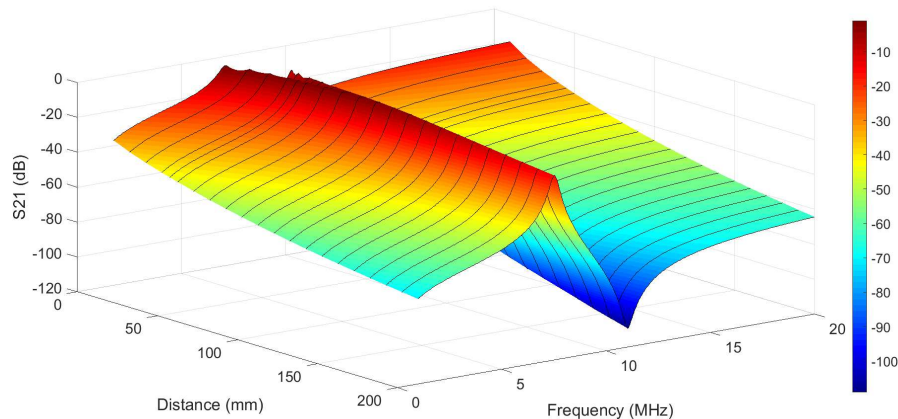
Figure 2.5: Simulation demonstrating the effect of varying the distance between transmitter and receiver coils/resonators, while keeping the capacitance of the resonators fixed at 1470 pF

The above figure illustrates that there is a distance between the coils (approximately 80 mm) that provides a critical coupling point [32]. When the distance between the coils is reduced, a phenomenon called "frequency splitting" is noticeable due to the fact that the coils are over coupled, which means that the coupling coefficient k is higher than the one required for critical coupling between the structures. Additionally, when this distance is increased beyond the critical coupling point, the efficiency will drastically decrease [32].

When the coupling between two coils is higher than the critical coupling, the frequency response of the system changes from a single-peak curve to a double-peak curve, which is the reason for calling this phenomenon as frequency splitting. Furthermore, the higher the coupling, the further apart these two peaks will be from each other [33]. These peaks are called even and odd splitting frequencies, and usually only one of these peaks will carry the maximum efficiency of a system for a certain coupling coefficient [33].

Fig. 2.6 contains cross sections of the previous image, also showing the measured S21 and resonant frequency for a certain distance between the receiver and transmitter. There are two markers positioned on each image, showing the data on the peak of the first resonant frequency of the measured and simulated curves, respectively.

16

(a) 20 mm

(b) 40 mm

(c) 45 mm

17
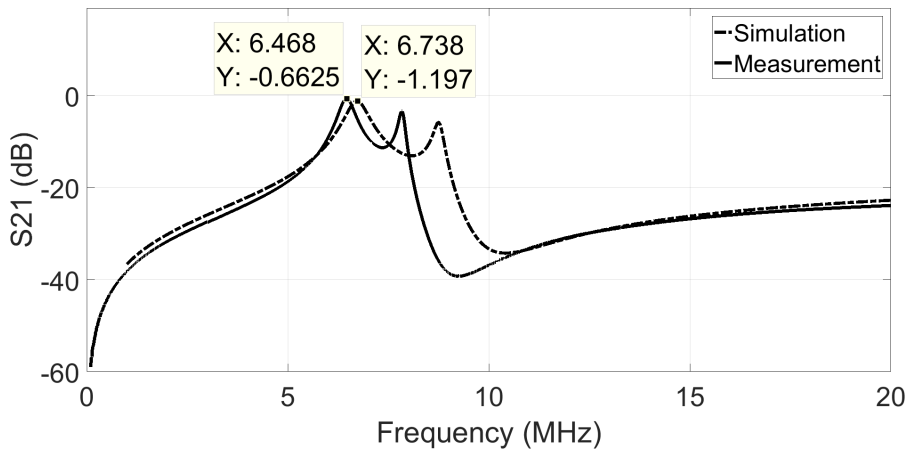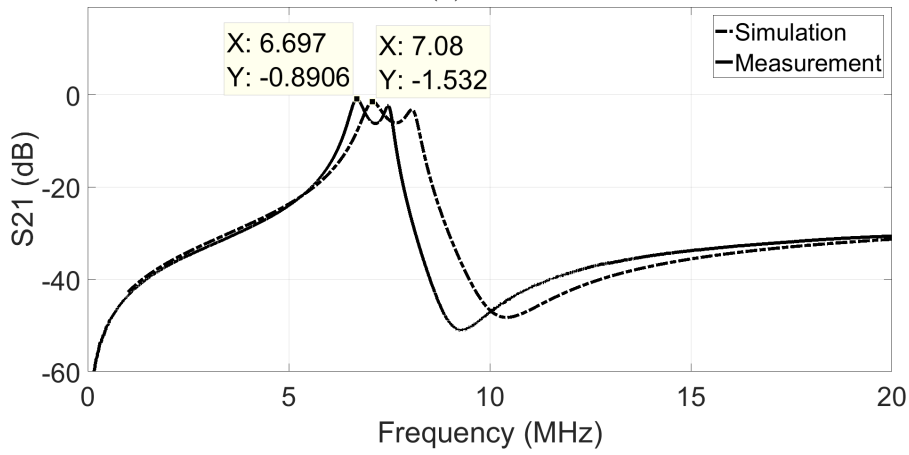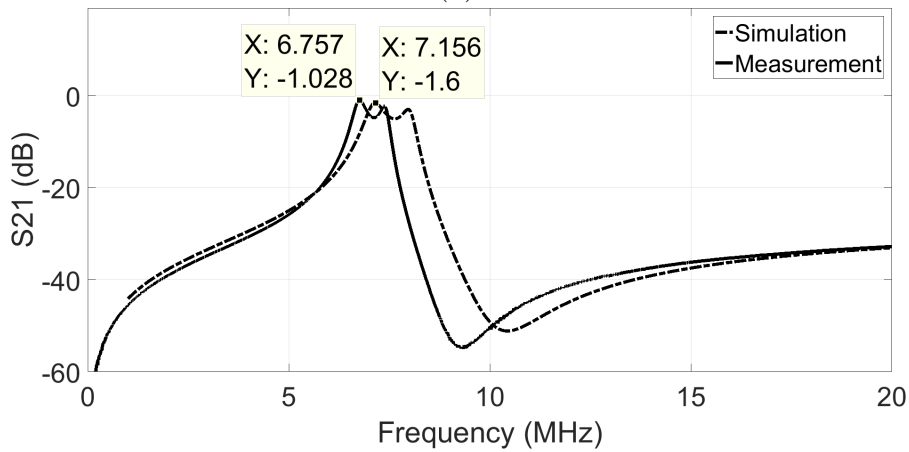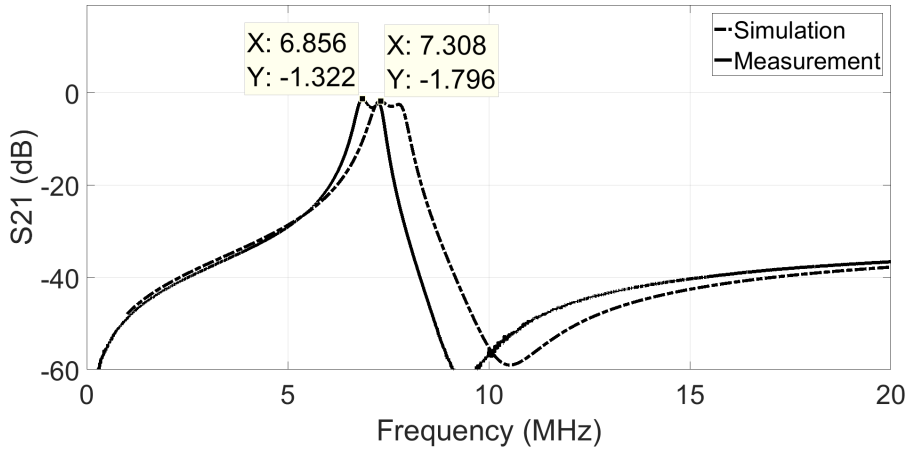
(d) 60 mm
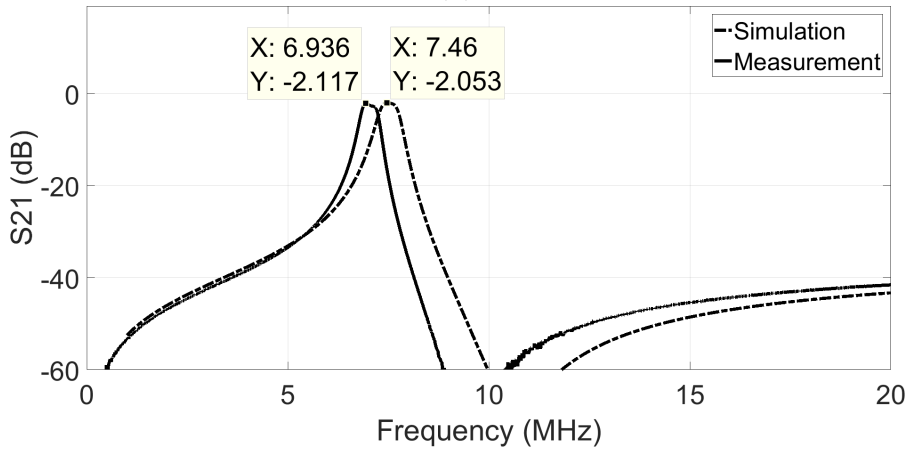
(e) 80 mm
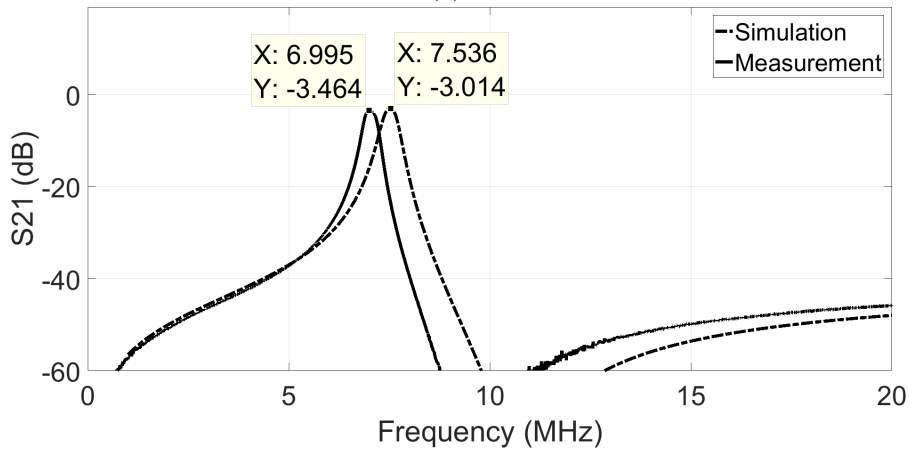
(f) 100 mm

Figure 2.6: Measurements and simulations showing the S21 of the system over different distances between transmitter and receiver, while keeping the capacitance of the resonators fixed at 1470 pF

18

The previous images evidentiate that as the distance between transmitter and receiver structures increases, the resonance splitting effect is minimized, with the efficiency of the system dropping after the critical coupling point. Furthermore, the slight frequency variation between measured and simulated results can be justified by the 10% tolerance that the chosen capacitors have [30].

Moreover, the previous results show that the resonant frequency of the designed inductive link is around the desired 6.78 MHz. The efficiency of the coils/resonators is significantly high, dropping to below 50% only with 10 cm of spacing between the structures (equivalent to S21 = -3 dB).

Next, the capacitor of both resonators is changed simultaneously in order to analyze its effect on the system, while the distance is kept constant at 45 mm. The simulations of the described situation are depicted in Fig. 2.7.
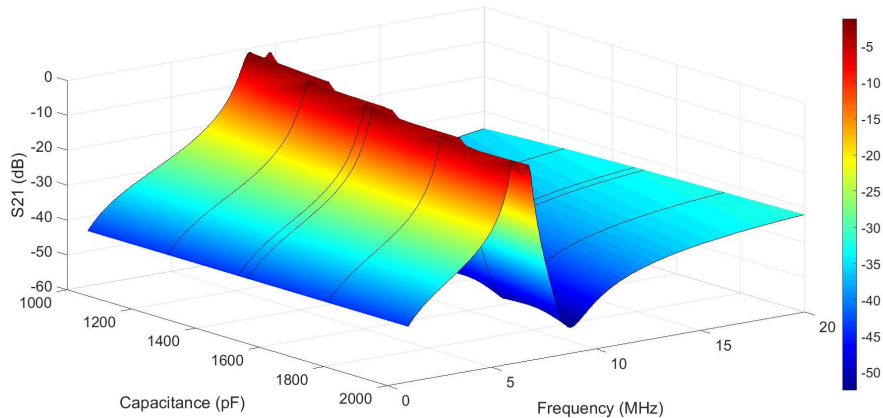
Figure 2.7: Simulation demonstrating the effect of varying the capacitance of both resonators simultaneously, while keeping the distance between receiver and transmitter devices at 45 mm

The distance of 45 mm between the structures illustrated on the previous image is in the over coupled region (noticeable by the two resonances for each capacitor value). This value was chosen for this simulation because both resonances present high efficiency, which facilitates the visualization of the frequency shifting due to alteration of the resonators' capacitance. Thus, one can conclude that the capacitance is mainly responsible for establishing the

19

resonance of the system, having minor impact in the system's efficiency.

Fig. 2.8 contains cross sections of the previous image, also showing the measured S21 and resonant frequency for a certain value of resonators' capacitance. Again, two markers are positioned on each image, showing the data on the peak of the first resonant frequency of the measured and simulated curves, respectively.

From these results it is visible that the calculated capacitance of 1.5 nF and the actual used value of 1.47 nF provide the closest resonance to 6.78 MHz, when compared to the other tested capacitors. Therefore, this capacitance will be the one used during the preliminary simulations of the final capacitive resonant single-conductor structure, in the next chapter.
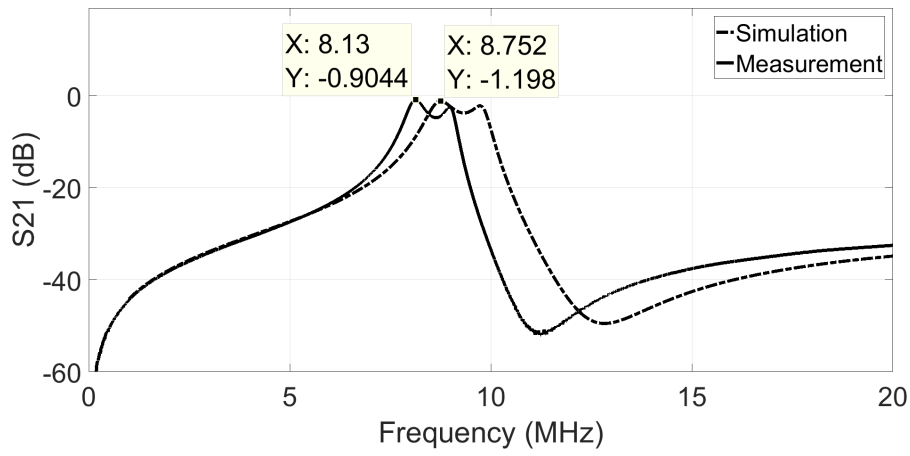
(a) 1000 pF

(b) 1250 pF

(c) 1470 pF

21
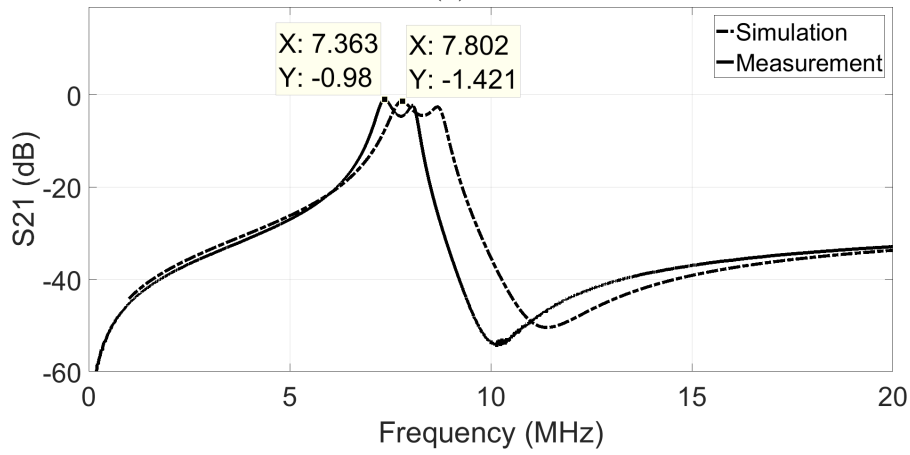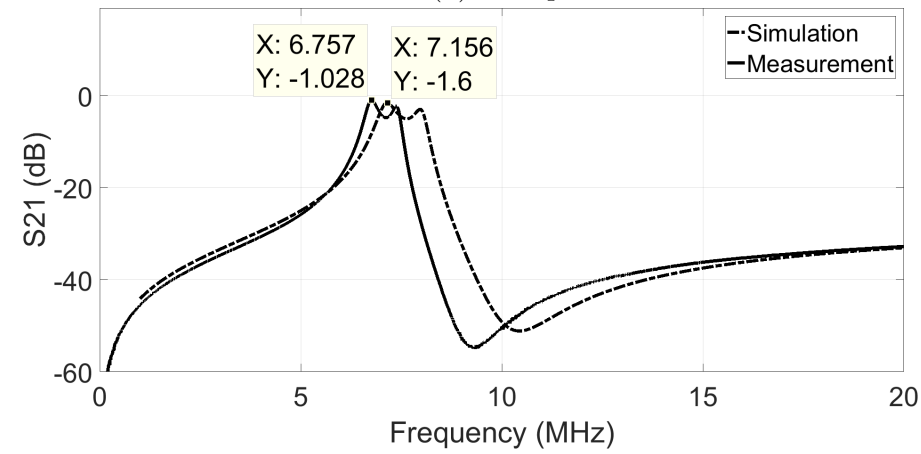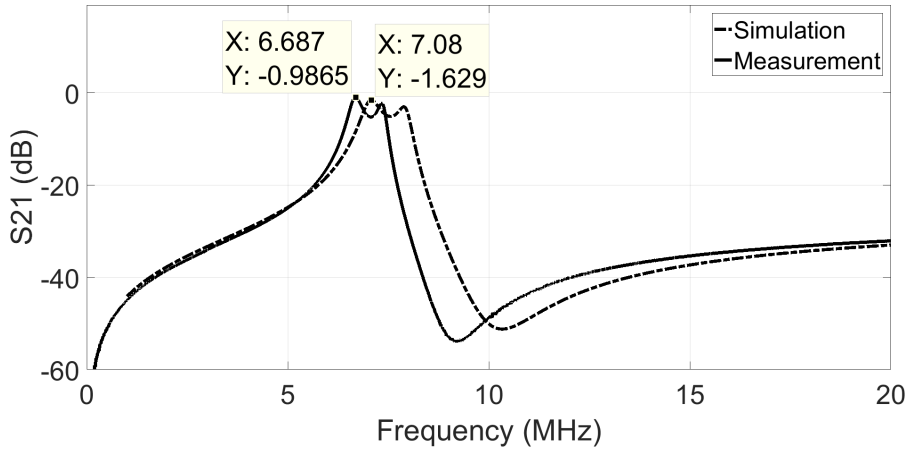
(d) 1500 pF
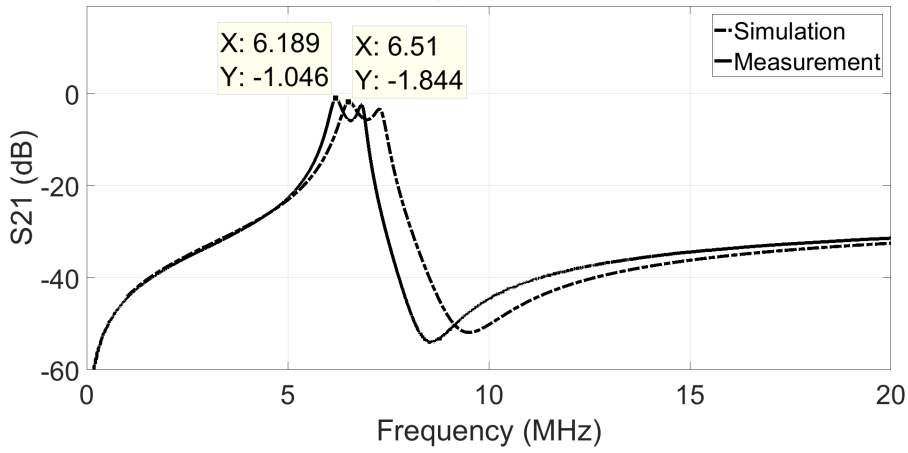
(e) 1750 pF
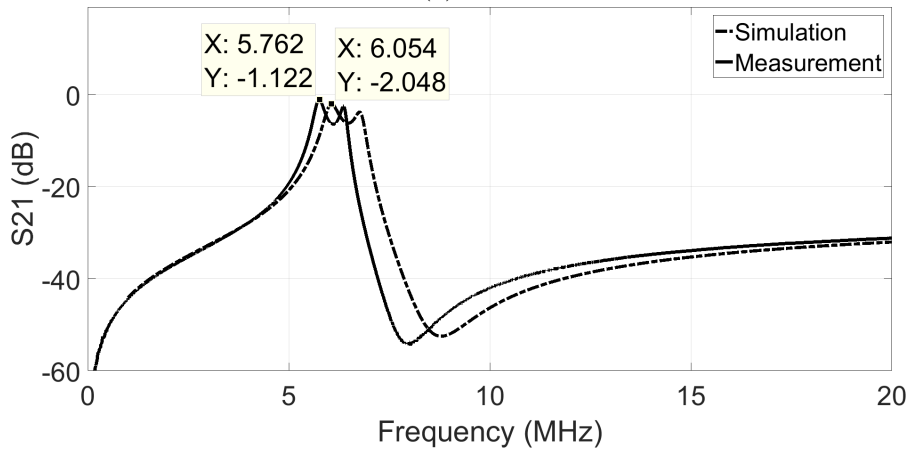
(f) 2000 pF

Figure 2.8: Measurements and simulations demonstrating the effect of varying the resonators' capacitors, while keeping the distance between structures fixed at 45 mm

From the provided results, it is reasonable to assume that the designed coils/resonators are able to efficiently transfer power at the desired frequency range.

In section 2.2.3, such topology will be challenged by the addition of a metallic obstacle between the transmitter and receiver devices.

Addition of capacitors to the coils

In the previous simulations and measurements, only the resonators had capacitors to create their resonance. Now, the further addition of capacitors to the transmitter and receiver coils (Fig. 2.9) will be analyzed. In theory, the incorporation of such components increases the efficiency of the system, since it makes the coils resonate at the same frequency of the source and resonators.
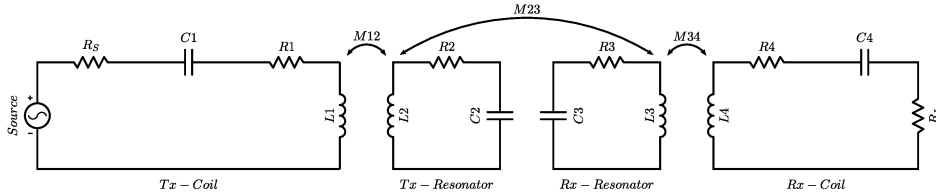
Figure 2.9: High-Q resonant inductive topology with coil capacitors

Following the previously described approach, one can calculate that the capacitance required to generate the resonance on the coils at 6.78 MHz is C_1 = C_4 = 1.87 nF.

Fig. 2.10 illustrates the coils' capacitors effect on the system. In this case, C_2 and C_3 are kept constant at 1.47 nF, and the distance between transmitter and receiver is fixed at 45 mm, while the coils' capacitances are varied simultaneously.

23
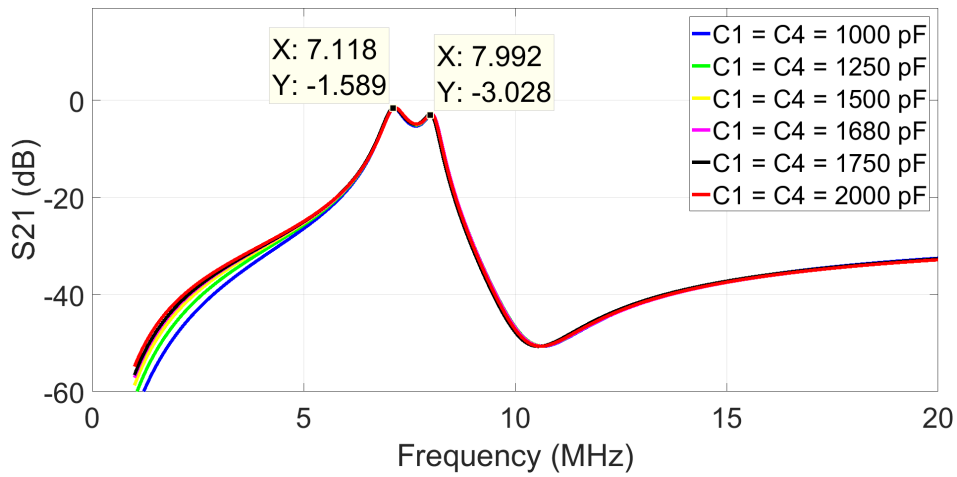
(a) Wide-frequency spectrum
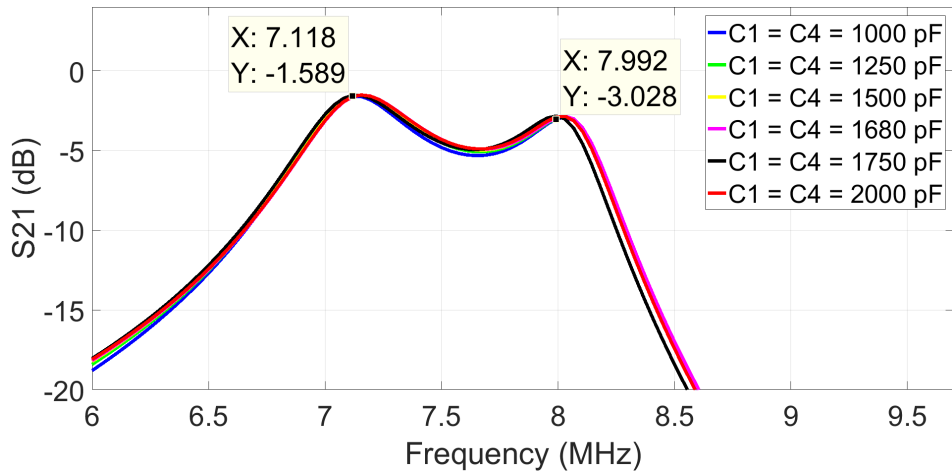
(b) Zoom in the resonant frequencies

Figure 2.10: Simulation demonstrating the effect of varying the coils' capacitance, while keeping the capacitance of the resonators fixed at 1470 pF and the distance between transmitter and receiver at 45 mm

24

Comparing the results presented in the previous image with the ones in Fig. 2.8c, it is visible that the improvement caused by the addition of the coils' capacitors is minimal at the operating frequency. With the additional capacitors, the highest S21 was -1.589 dB, compared to -1.6 dB when no capacitor is added to the coils (according to the previously simulated results). Additionally, even when C_1 and C_4 are drastically changed, the resonant frequency is not significantly affected. Therefore, henceforth, coils' capacitors will not be maintained in the system.

2.2.3   Adding a Metallic Obstacle Between the Coils

In the previous sections it was demonstrated that the designed coils/resonators are suitable for regular IPT applications at the desired frequency. In this section, metallic obstacles are added between the coils, aiming to prove that the metallic embodiment of an electronic device is enough to significantly decrease the efficiency of an inductive link.

As before, simulations were performed to sustain such claims, following the approach described in the previous sections. Fig. 2.11 presents the S21 of the 4-coil system with a metallic obstacle placed midway the transmitter and receiver, composed of a 30x30 cm copper sheet with 90 μm of thickness, over a variety of distances between the devices.
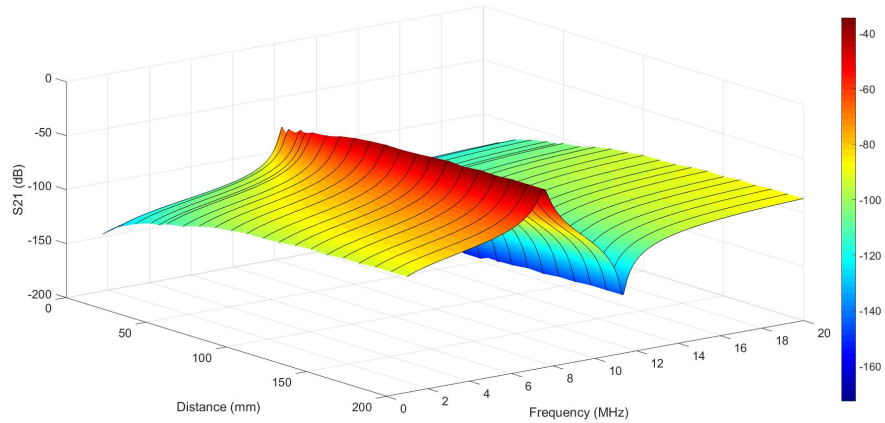
Figure 2.11: Simulation demonstrating the effect of varying the distance between transmitter and receiver coils when a metallic obstacle is added between the devices, while keeping the capacitance of the resonators fixed at 1470 pF

From the previous image, one can deduce that the addition of the metallic obstacle was enough to completely stop the power transfer, since the S21 dropped bellow -40 dB. Since the capacitor alone would not be able to improve this efficiency, as shown in the previous sections, the plots presenting the capacitors variation will be omitted for this case.

Additionally, it is noticeable that the efficiency of the system increases as the distance between the devices is higher. This phenomenon happens because a greater distance between devices means that the distance from coils/resonators to the metallic obstacle increases as well. Thus, the magnetic fields have more freedom to move around the obstacle as the resonating structures are separated from it [34].

2.3 Capacitive Power Transfer

Capacitive power transfer utilizes near-field electric field coupling to achieve contactless power transfer [6]. In CPT systems, pairs of metallic electrodes work as capacitors that transfer power from the transmitter to the receiver side. An alternating source creates an alternating voltage that is applied to the capacitive plates. This voltage will charge and discharge the capacitor, con-

sequently generating an alternating current on the receiver side. The voltage difference between the two plates will create an electric field in the capacitor's dielectric. A capacitor will offer an impedance to any alternating current applied to it, which is known as reactance (X_C), determined as in Eq. (2.13) [29].

$$X_C = \frac{1}{j\omega C} = \frac{1}{j2\pi f C} \qquad (2.13)$$

The most common form of capacitive power transfer is called bipolar CPT, which utilizes two pairs of active plates (Fig. 2.12). One pair is the forward capacitor, while the other is the return capacitor. Since these capacitors usually add a relatively small capacitance to the system, they impose a large reactance to the current. Thus, compensation circuits are required to minimize the effect of the plates in the system [5], [35].
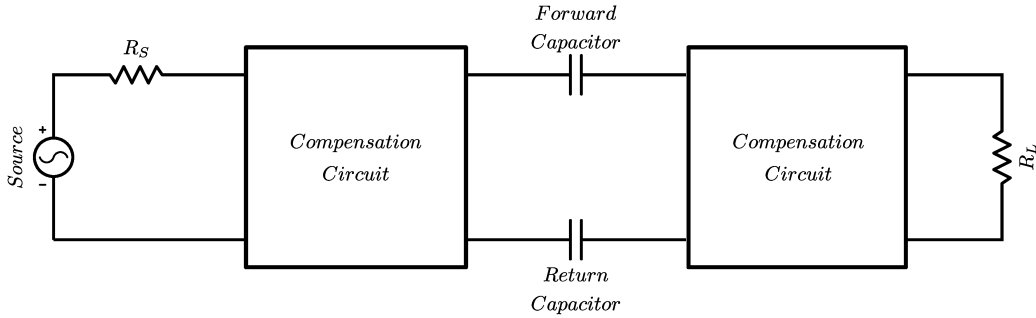
Figure 2.12: Capacitive power Transfer Block Diagram

Capacitive power transfer is not widely utilized in commercial applications due to the fact that the electric field intensity present in the system will significantly increase as the power rises [36]. Although such technique has a limited capability for high power applications, some recent research focus on utilizing this technology to power electric vehicles [13]. Furthermore, when compared to IPT, the CPT is less susceptible to electromagnetic interference (EMI) [5] and has insignificant losses due to eddy currents created in nearby metallic objects [6] because the capacitive plates may also act as a shield, not allowing a significant quantity of fields to reach other objects.

In order to determine the plates capacitance, Eq. (2.14) can be used, since

the capacitors are composed of relatively simple structures. Additionally, such formula is a fair approximation because the size of the plates is significantly larger than the distance between them.

$$C = \frac{\varepsilon A}{d} \tag{2.14}$$

In the previous equation, ε is the permittivity of the dielectric between the plates (which is considered to be air, $\varepsilon_0 = 8.85 \times 10^{-12}$ F/m), A is the area of the plates, and d is the distance between them. For a capacitor composed of two 30x30 cm copper sheets, with 90 μm of thickness and placed 5 mm apart, the calculated capacitance is $C_{Plates} = 159.3$ pF. This will be the capacitance of the initial state of the capacitive resonant single-conductor system presented in the next chapter.

2.4 Single-Conductor

In order to understand the single-conductor concept presented in this thesis, first, it is necessary to differentiate the behavior of the proposed system from the notorious Goubau single-conductor structure [17], [37]. Goubau's structure was proposed as a particular example of Sommerfeld waves on dielectric coated wires. Thus, the latter system works by exciting surface waves on a conducting structure [38]. Although it provides efficiency comparable to coaxial power transfer [39], [40] and it has potential for long-distance low loss power transmission at high frequencies [41], Goubau's single-conductor can be extremely difficult to design and requires massive horn launchers to excite the required propagation mode on top of the structure [37].

On the other hand, the system proposed in this thesis utilizes open-ended resonators to provide a standing wave (not a surface wave, as in the previous case) in the single-conductor structure [15], [16], [19], [42]–[44]. Such approach allows efficient power transfer over a conducting structure in the kHz and MHz range, presenting smaller overall size and lower radiation losses. An open-ended resonator supports a current wave distribution that presents a boundary condition of zero current at the open-ends [43]–[45]. In order to

characterize the open-ended resonator, previous applications relied on simulations [15], [16], [19], [42], [43], measurements on near-field coupled coils [15], [16], power delivered to a load [15], [16], [42], [43], or assumptions of current or voltage distribution [43]–[45], since a complete theoretical description of the resonator has not been realized due to its complex behavior and difficulty to derive an accurate circuit model solely based on the resonator's dimensions.

Different approaches utilizing open-ended resonators to transfer power over a single-conductor include: a direct feeding by single-ended input port [19], [42], [44], a direct feeding by capacitive coupling [43], and a direct feeding by near-field coupling [15], [16]. This thesis follows the near-field coupling feeding approach presented in [15], [16]. The proposed method uses one open-ended resonator connected at the transmitter side to enable single-conductor power transfer to another resonator at the receiver side. While the input power is applied to a transmitting coil, which is magnetically coupled to the first resonator, the second resonator is coupled to a receiving coil that delivers power to a load, permitting the use of an electrically small conducting structure to provide the current path between resonators. Therefore, it primarily provides a nearly uniform voltage distribution over the conductive structure, while using resonators with significantly large electrical length, but compact overall dimensions.

Although electrically large structures can be used as the single-conductor structure with this method, current literature and applications have focused in power distribution through structures smaller than a wavelength. Using the combined single-conductor and wireless power transfer methods, it is possible to achieve more freedom regarding the misalignment and distance between the transmitter and receiver devices, in comparison with the conventional WPT systems.
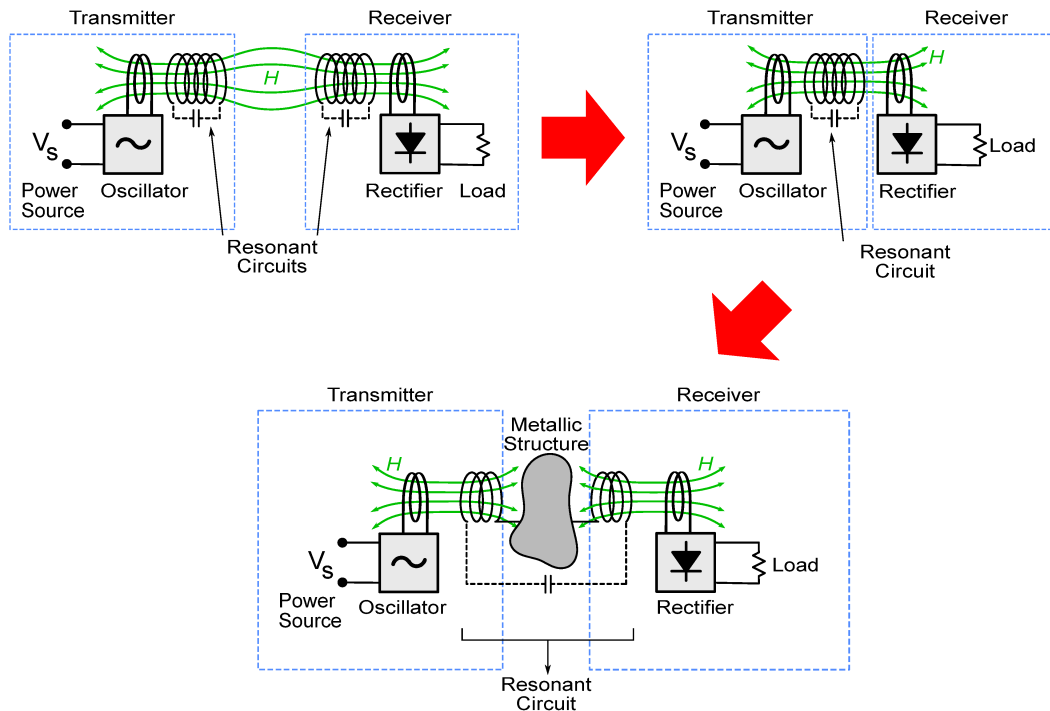
Figure 2.13: Derivation of single-conductor

Fig. 2.13 presents a simplified explanation of how to derive the single-conductor fed with open-end resonators. Firstly, one must imagine a high-Q resonant IPT system, as described in Section 2.1.3. When distance between transmitter and receiver is not of interest, it is possible to remove one resonator, while bringing the receiver closer to the transmitter. Next, this one resonator can be fragmented into two parts with a metallic structure in the middle, composing together the single-conductor structure. This means that the final single-conductor structure must have all its parts designed to guarantee that together they became a resonator at the desired frequency.

2.5 Chapter Summary

In this chapter each individual part of the capacitive resonant single-conductor was separately described: coils/resonators, capacitive plates and single-conductor. Firstly, the advantages of using a high-Q inductive topology in this project were shown. Then the required coils/resonators were designed to provide high efficiency power transfer at 6.78 MHz.

Then, the utilized capacitive plates were analyzed, with its capacitance being calculated for the distance of 5 mm between the plates, which will be the minimal distance used in future simulations and measurements.

Finally, the single-conductor was explained, showing the basic concepts behind its functioning. Further details of the entire system and its components will be provided in the next chapter.

Chapter 3

Single-Conductor With a Capacitive Discontinuity

Now that each individual component of the system has been further described, the previous concepts will be put together to explain the structure proposed by this thesis: the single-conductor fed by open-ended resonators with a capacitive discontinuity, also called as "Capacitive Resonant Single-Conductor".

3.1 Capacitive Resonant Single-Conductor

As previously presented, the capacitive resonant single-conductor technology proposes a discontinuity in the metallic structure of a regular SCPT system fed by coils coupled to open-ended resonators. This discontinuity is conceived as one pair of metallic plates, which already presents an advantage over regular CPT, that requires at least two pairs of plates. The addition of these capacitive plates in the conductive path allows contactless power transfer, while maintaining the advantages of the SCPT [46].

Fig. 3.1 presents the basic diagram of the system. The capacitive resonant single-conductor structure is added in the middle of the high-Q inductive link presented previously. This single-conductor structure with a discontinuity can be compared to a regular resonator, as explained in Section 2.4. Therefore, all the components of this part of the system must be designed in order to create resonance at the desired frequency.
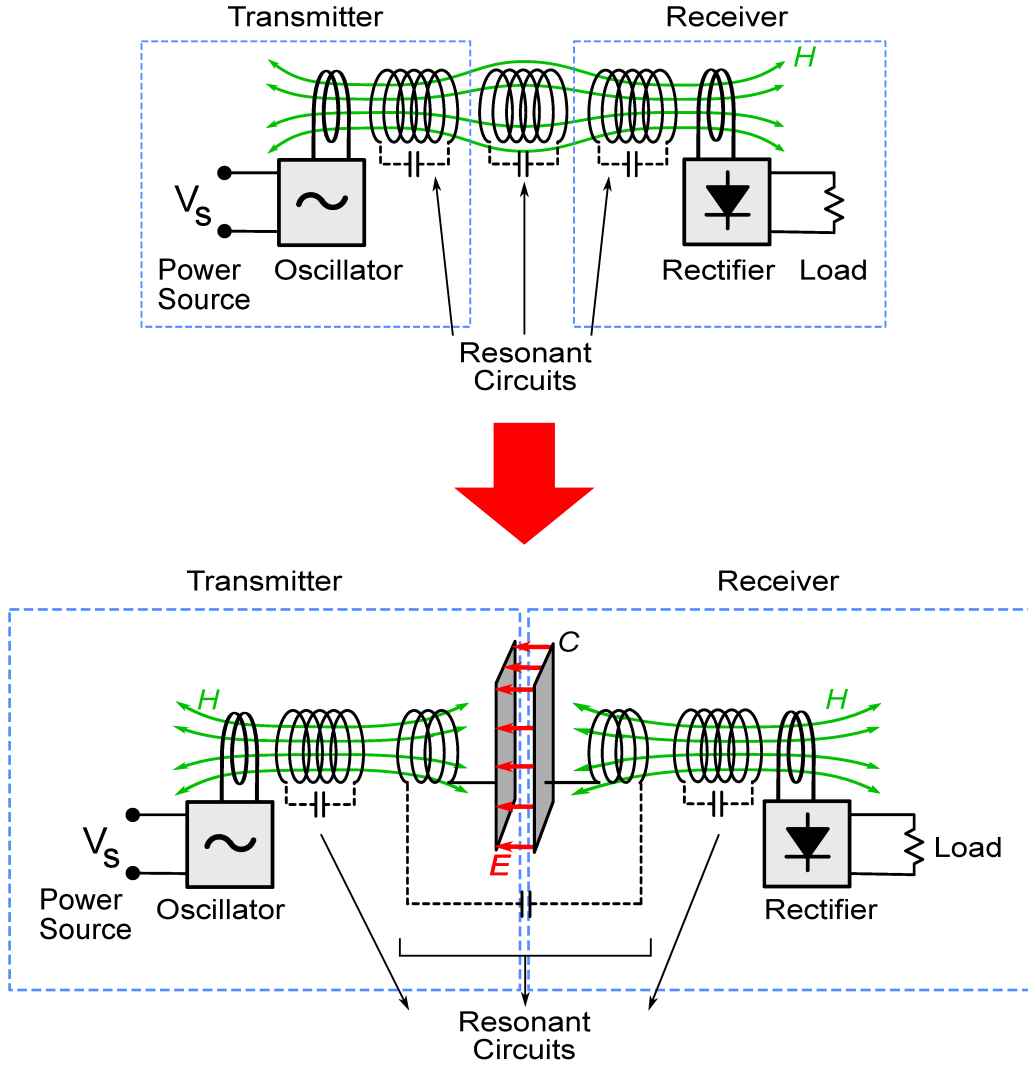
Figure 3.1: Capacitive resonant single-conductor power transfer diagram

Furthermore, the chosen working frequency for this project is 6.78 MHz because it is one of the ISM radio bands, and it is the frequency used by the Airfuel standard [27]. Due to the use of higher frequency when compared to [15]–[17], the structures presented in this thesis can be physically compact.

As explained in Section 2.13, SCPT can be achieved by fragmenting one resonator and adding a metallic structure in the middle, as long as this conductor is electrically small when compared to the wavelength at this frequency (λ = 44.25 m). Then, the entire single-conductor structure, including resonators and metallic plates must resonate together at the desired frequency.

In Section 2.3, it was explained that when capacitive plates are added to

33

the system, a reactive impedance is inserted to the circuit, which alters the system's resonance and, thus, must be compensated for. This compensation is performed by including series inductors to the plates.

Fig. 3.2 provides the circuit model created for the system, while Table 3.1 presents the numerical values calculated for each element of the diagram.
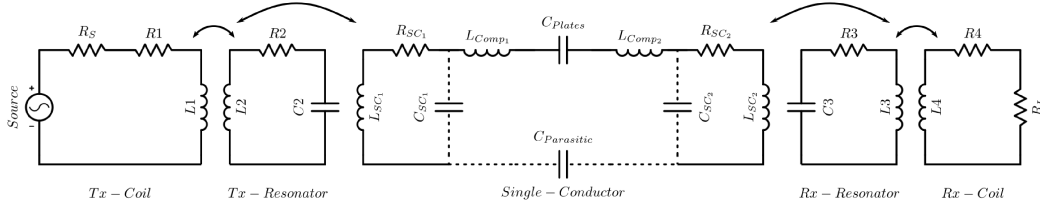
Figure 3.2: Capacitive resonant single-conductor power transfer circuit model

The values for the components that compose the coils, resonators and capacitive plates were calculated in the previous chapter. Therefore, this chapter will focus on the remaining parts of the circuit, which are the ones that form the capacitive resonant single-conductor structure.

In the next sections, calculations will be performed to determine the self-inductance (L_{SC_1} and L_{SC_2}), self-capacitance (C_{SC_1} and C_{SC_2}) and equivalent series resistance (R_{SC_1} and R_{SC_2}) of the fragments of resonator that are connected to the capacitive plates.

Then, the parasitic capacitance ($C_{Parasitic}$) between the open-ends of the fragments of resonator will be determined, followed by the calculation of the compensation inductors (L_{Comp_1} and L_{Comp_2}).

Table 3.1: Calculated parameters of designed capacitive resonant
single-conductor system at 6.78 MHz

	C_1	-
Tx-Coil	L_1	0.294 μH
	R_1	0.1773 Ω
	C_2	1.5 nF
Tx-Resonator	L_2	0.367 μH
	R_2	0.2128 Ω
	C_{SC_1}	5.06 pF
Tx-SCPT	L_{SC_1}	18.825 μH
	R_{SC_1}	0.6892 Ω
	C_{SC_2}	5.06 pF
Rx-SCPT	L_{SC_2}	18.825 μH
	R_{SC_2}	0.6892 Ω
	C_3	1.5 nF
Rx-Resonator	L_3	0.367 μH
	R_3	0.2128 Ω
	C_4	-
Rx-Coil	L_4	0.294 μH
	R_4	0.1773 Ω
Compensation	L_{Comp_1}	69.067 μH
	L_{Comp_2}	69.067 μH
Capacitive Plates	C_{Plates}	0.1593 nF
Parasitic Capacitance	$C_{Parasitic}$	0.0032 nF
Source	R_S	50 Ω
Load	R_L	50 Ω

In the next sections, the parameters that were not obtained in Chapter 2, but already presented in the previous table, will be explained.

3.1.1 Fragments of Resonator Attached to the Metallic Plates

In order to determine the parameters of the fragments of resonator connected to the single-conductor structure, the method presented in the previous chapter cannot be used to determine the parameters of these coils. Due to physical constraints, they are conceived as spiral coils with multiple turns, therefore, their radius changes on each turn. Thus, a different approach will be used to determine its parameters.

Self-Inductance

In order to calculate the inductance of these fragments of resonator, it is necessary to calculated the mutual inductance that each loop of the coil has with all the other loops, including itself, and add all these values together. Therefore, it will be necessary to make N^2 operations to obtain the inductance of these structures, where N is the number of turns of a coil. In [47], Maxwell presents an expression (Eq. (3.1)) to calculate the mutual inductance between two parallel circular loops, like the ones in Fig. 3.3.
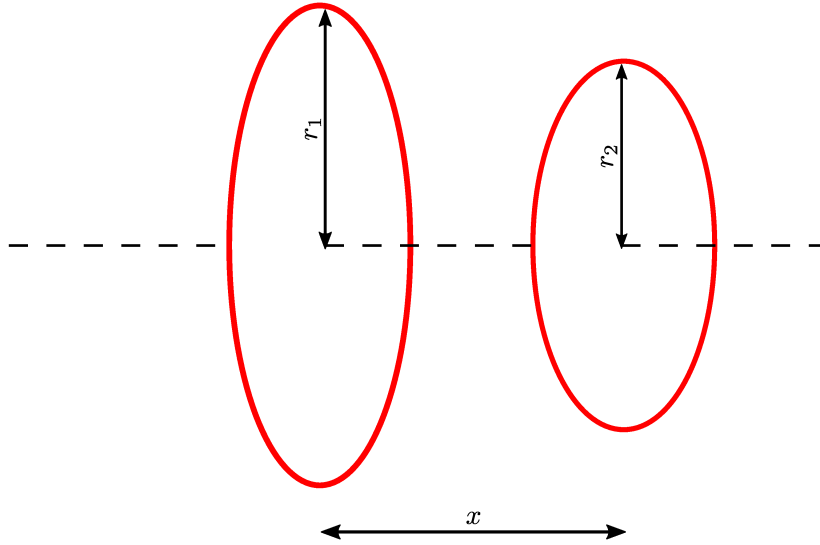
Figure 3.3: Diagram of Two Parallel Circular Loops

$$M = \frac{8\pi\sqrt{r_1 r_2}}{\sqrt{e}}\left[K\left(e\right) - E\left(e\right)\right] \tag{3.1}$$

In Eq. (3.1), $K(e)$ and $E(e)$ are the elliptic integrals of the first and second kind, respectively, of modulus e.

$$e = \frac{x_1 - x_2}{x_1 + x_2} \tag{3.2}$$

In the previous equation, x_1 and x_2 are the closest and furthest distances between the loops, respectively. Therefore:

$$x_1 = \sqrt{(r_1 + r_2)^2 + x^2} \tag{3.3}$$

36

$$x_2 = \sqrt{(r_1 - r_2)^2 + x^2} \tag{3.4}$$

In [48], Equations (3.5), (3.6) and (3.7) are used to obtain a simplified version of Maxwell's mutual inductance expression, presented as Eq. (3.8). This is the expression that will be used to calculate the mutual inductance between two loops.

$$K(e) - E(e) = c_s K(e) \tag{3.5}$$

$$K(e) = \frac{\pi}{2a} \tag{3.6}$$

$$c_s = \frac{1}{2} \sum_{n=1}^{\infty} 2^n c_n^2 \tag{3.7}$$

$$M = \frac{2\pi^2}{a} \sum_{n=1}^{\infty} 2^{n-1} c_n^2 \tag{3.8}$$

In the previous equation, a is the AGM (Arithmetic-Geometric Mean) related to the elliptical integral $K(e)$. The arithmetic mean of two numbers is the numbers added together and then divided by two. Meanwhile, the geometric mean of two numbers is the square root of those two numbers multiplied. If one repeats the arithmetic and geometric means between two numbers a_0 and b_0, as presented in (3.9) and (3.10), these values will converge to the same result after several iterations, this converged result is the arithmetic-geometric mean.

$$a_n = (a_{n-1} + b_{n-1})/2 \tag{3.9}$$

$$b_n = \sqrt{a_{n-1} \times b_{n-1}} \tag{3.10}$$

$$c_n = (a_{n-1} - b_{n-1})/2 \tag{3.11}$$

However, in order to calculate the mutual inductance of a loop and itself, especial attention is required. Because Eq. (3.8) would not work with a value of $x = 0$, an approximation is made to assume $x = 0.7788 \times (d/2)$, according to [47], for this particular situation.

A Matlab code was then written to calculate the mutual inductance that each loop of the coil has with the others, including itself (also known as the self-inductance of each loop), using Eq. (3.8) and adding all these values together to obtain the inductance of the fragments of resonator.

These structures have an inner diameter of $D = 64$ mm and are built with a 16 AWG wire ($d = 1.29$ mm), using a radius variation of 3 mm between each loop, and $N = 13$ turns. This results in $L_{SC_1} = L_{SC_2} = 19.8156$ μH.

However, the method utilized to calculate these inductances does not take into account factors like the proximity effect, the non-constant radius in a single-turn and the polygonal shape of the coils, for example. Therefore, an error of up to 5% can be expect in the obtained results [49].

Assuming the maximum error, the final inductances of the fragments of resonator would be $L_{SC_1} = L_{SC_2} = 18.82482$ μH.

Self-Capacitance

Now that the inductance of the coils was calculated, its self-capacitance will be found by Ansys HFSS simulations. With only one of those fragments of resonator being simulated alone (detached from the system), as in Fig. 3.4, the resonance of this structure is used to determine its capacitance.
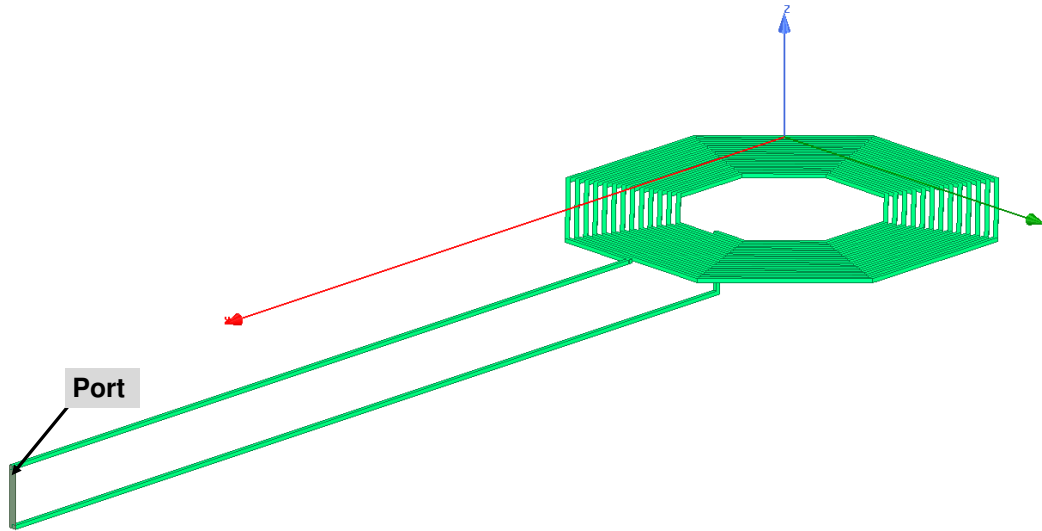
Figure 3.4: Image of the simulated system to obtain the self-capacitance of each fragment of resonator

By performing the one-port simulation in HFSS of each fragment, as depicted in the previous image, the self-resonance of these structures can be found (Fig. 3.5). The resonance occurs when the imaginary impedance of the one-port simulation of the coil is equal to zero. This means that, at this frequency, the self-capacitance and self-inductance of the coil impose the same magnitude of reactance to the system, being added to zero.
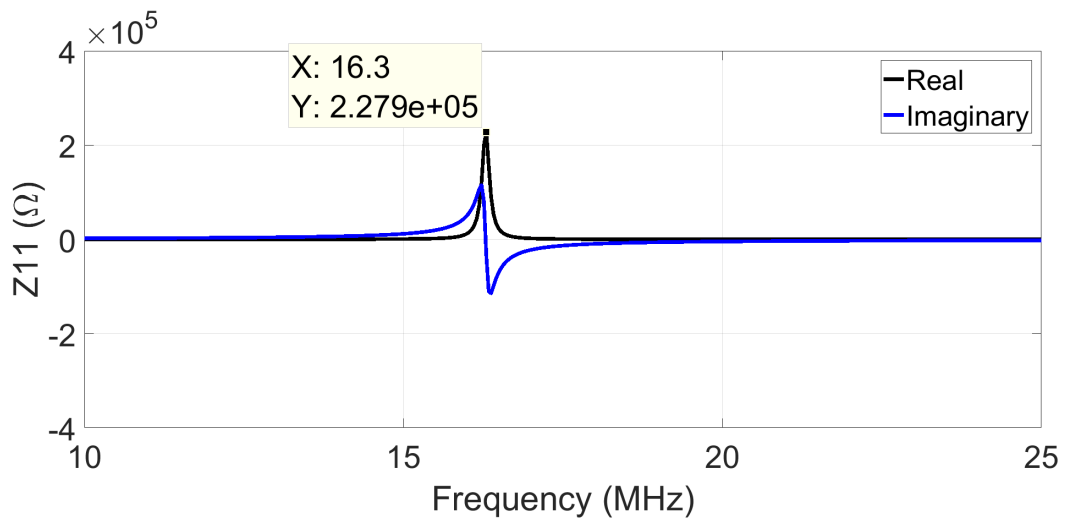
Figure 3.5: Real and imaginary impedances of the fragment of resonator

With a self-resonance occurring at 16.3 MHz and a self-inductance of 18.825 μH, one can use Eq. (2.4) to find the self-capacitance of each fragment of resonator as $C_{SC_1} = C_{SC_2} = 4.8$ pF.

ESR

In order to calculate the ESR (Equivalent Series Resistance) of these fragments of resonator (R_{SC_1} and R_{SC_2}), first their wire DC resistance must be calculated using Eq. (3.12).

$$R_{DC} = \rho l / A \tag{3.12}$$

$$l = \sum_{n=0}^{N-1} 2\pi(D/2 + np) \tag{3.13}$$

$$A = \pi(d/2)^2 \tag{3.14}$$

In Eq. (3.13), l is the total length of wire used to build these fragments of resonator. Because these particular coils are planar, the radius ($D/2$) will change every turn by a constant pitch (p). Therefore, a sum is required to add the circumference of all turns together, until all N turns are considered in this equation.

In Eq. (3.14), A is the cross section area of the 16 AWG wire used to build these coils, with diameter d.

From previous sections, we know that $D = 64$ mm, $N = 13$, $p = 3$ mm and $d = 1.29$ mm. Applying these values in the previous equations, one can obtain that $A = 1.31 \times 10^{-6}$ m^2 and $l = 4.08$ m, which gives $R_{DC} = 0.0525$ Ω, for a copper wire ($\rho = 1.68 \times 10^{-8}$ Ωm).

However, since the system is operating at relatively high frequency, the skin effect phenomenon will increase the ESR due to the fact that current will only flow on the wire's surface. The skin depth, which is the depth that the current actually uses to flow, can be obtained through Eq. (2.7), using $\mu_{copper} \approx \mu_0 = 4\pi \times 10^{-7}$, as $\delta = 25.053 \times 10^{-6}$ m.

From the same equations provided in Section 2.2.1, one can calculate that $A_{eff} = 99.559 \times 10^{-9}$ m^2 and, therefore, $R_{SC_1} = R_{SC_2} = R_{AC} = 0.6892$ Ω.

3.1.2 Parasitic Capacitance

To continue the system's analysis, it is necessary to obtain the theoretical value of the parasitic capacitance ($C_{Parasitic}$) between the two open-ends of the fragments of resonator. To achieve this, Ansys HFSS is used to perform simulations with only the single-conductor structure and a port connected between the open-ends of each fragment of resonator, as depicted in Fig. 3.6.

This one-port simulation is performed to find the self-resonance of the capacitive single-conductor structure, so that its self-capacitance (here named as $C_{Parasitic}$) can be determined using a similar approach to the one explained in Section 3.1.1.
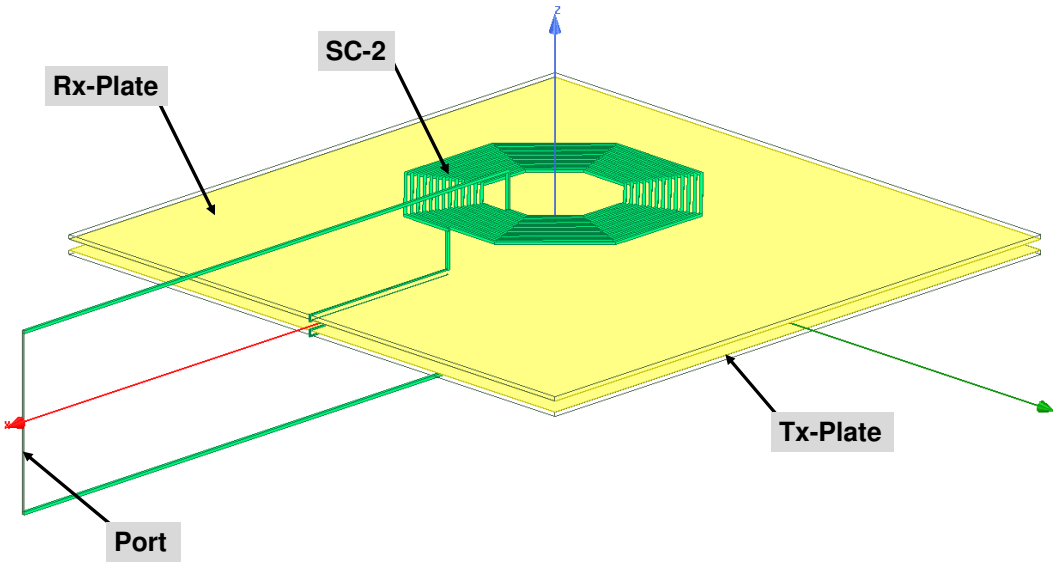
Figure 3.6: Image of the simulated system to obtain the self-capacitance of the capacitive resonant single-conductor structure

With the found resonance of this structure, one can calculate its self-capacitance ($C_{Parasitic}$) by applying the following equations:

$$X_{L_{SC1}} = j\omega L_{SC_1} \tag{3.15}$$

41

$$X_{L_{SC2}} = j\omega L_{SC_2} \tag{3.16}$$

$$X_{C_{Plates}} = \frac{1}{j\omega C_{Plates}} \tag{3.17}$$

$$X_{C_{Parasitic}} = -(X_{L_{SC1}} + X_{C_{Plates}} + X_{L_{SC2}}) \tag{3.18}$$

$$C_{Parasitic} = \frac{1}{j\omega X_{C_{Parasitic}}} \tag{3.19}$$

Moreover, one can observe that the self-capacitance of the fragments of resonator (C_{SC_1} and C_{SC_2}) are not taken into consideration in Eq. (3.18). This was done because, in reality, this is not the only parasitic capacitance present in the middle of the single-conductor structure. The capacitance between coils/resonators and the capacitive plates, for instance, represents even more impact in the system. Therefore, for simplicity, none of these values is taken into consideration at this point.

From the previous section, we know that $L_{SC_1} = L_{SC_2} = 18.825$ μH, and from Section 2.3, we know that $C_{Plates} = 159.3$ pF. The simulations show that the first resonant frequency of the capacitive resonant single-conductor structure is at 14.65 MHz (Fig. 3.7). At this frequency, one can calculate that $X_{L_{SC1}} = X_{L_{SC2}} = $ j1733.0 Ω and that $X_{C_{Plates}} = $ -j68.2 Ω. Applying these values to Eq. (3.18), we obtain $X_{C_{Parasitic}} = $ -j3397.4 Ω, which results in $C_{Parasitic} = 3.2$ pF.
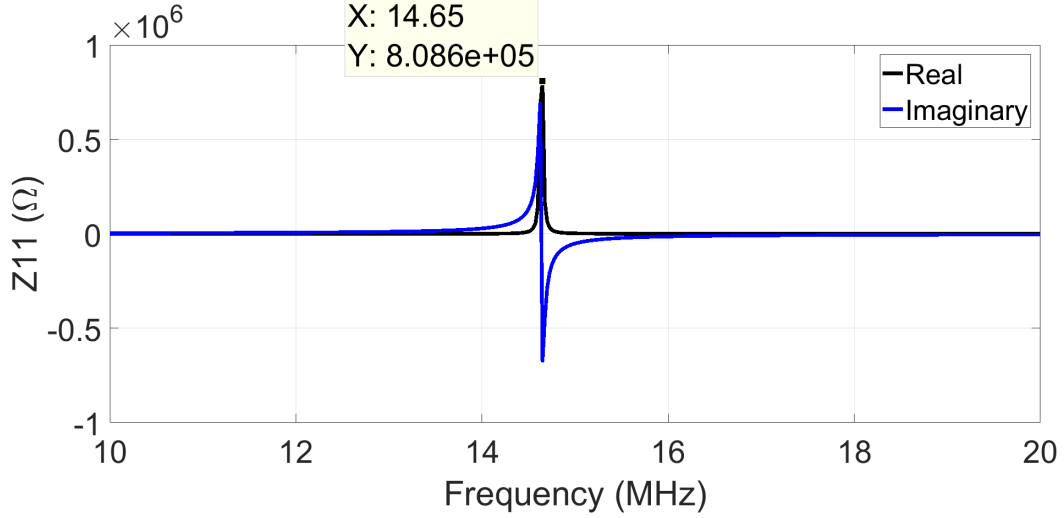
Figure 3.7: Real and Imaginary Impedances of the Single-Conductor Structure

However, in order to make the structure resonate at 6.78 MHz, it will be necessary to add compensation inductors to balance the reactance inserted by the capacitive plates.

3.1.3 Compensation Inductors

As explained in Section 2.3, it is important to add compensation circuits when capacitive plates are used in the system, so that their large reactance is canceled out [5], [35]. The design of the compensation inductors L_{Comp_1} and L_{Comp_2} depends on the following equation:

$$X_{C_{Parasitic}} = -(X_{L_{SC1}} + X_{LComp_1} + X_{C_{Plates}} + X_{LComp_2} + X_{L_{SC2}}) \quad (3.20)$$

Using the same method provided in the previous section, one can obtain the following values at 6.78 MHz: $X_{L_{SC1}} = X_{L_{SC2}} =$ j801.94 Ω, $X_{C_{Plates}} =$ -j147.36 Ω and $X_{C_{Parasitic}} =$ -j7341.0 Ω. For simplicity, it is established that both compensation inductors are equal, which results in $X_{LComp_1} = X_{LComp_2}$ = j2942.2 Ω. From this, one can obtain that $L_{Comp_1} = L_{Comp_2} = 69.067$ μH.

3.2 Simulated System

After obtaining all the theoretical values on Table 3.1, the entire system was simulated using Ansys HFSS. Although the values calculated in the previous sections are fairly close approximations, they still present errors in their final results. These errors are due to the octagonal shape of the coils/resonators, pieces of cardboard and styrofoam added to support the built system, additional parasitic capacitances that were not take into account in the calculations (such as the capacitance between coils/resonators and the metallic plates), among other uncertainties in the system. Therefore, the simulations will help to optimize the calculated values in order to obtain the best version of the system to be built in the laboratory.
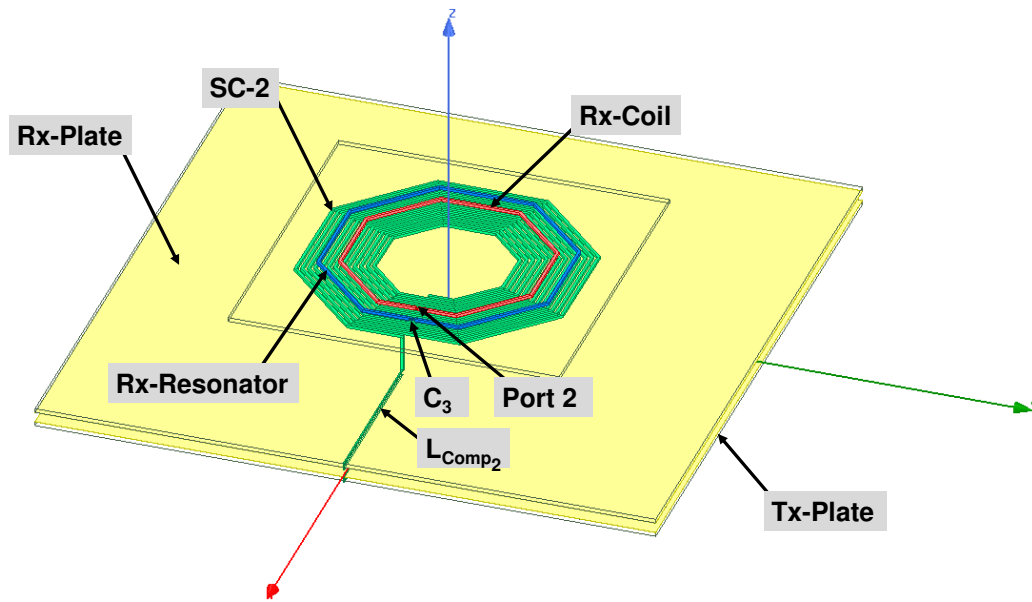
Figure 3.8: Image of the simulated system in HFSS

Fig. 3.8 depicts the simulated system, created based on the values already calculated in this document. Furthermore, one can observe that the fragments of resonator were placed with a distance of 1 cm from the capacitive plates, so that the losses due to eddy currents generated in the copper plates because of the magnetic field created by the coils/resonators would be minimized [34].

44
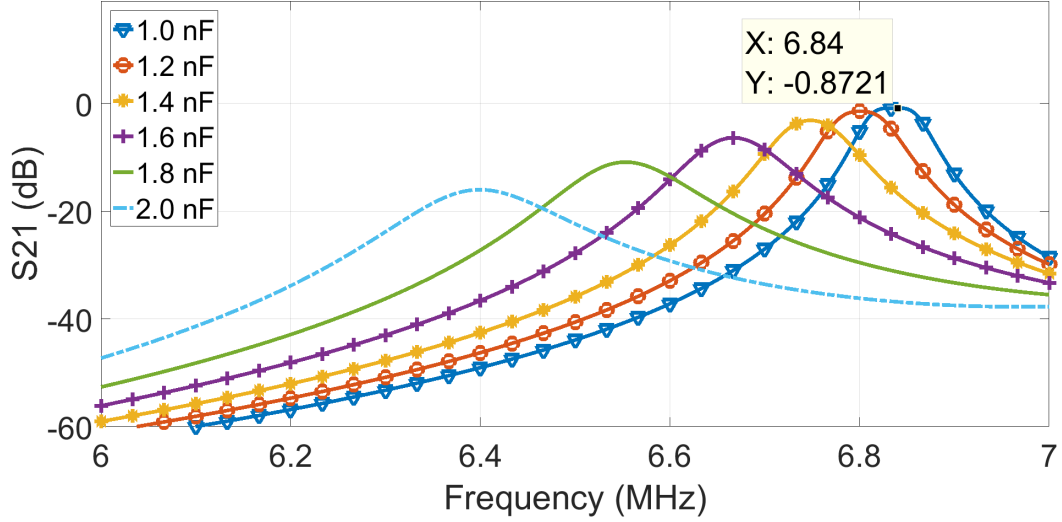
Figure 3.9: Varying parameters (C_2 and C_3) of the complete system, while keeping $L_{Comp_1} = L_{Comp_2} = 40\ \mu$H

From the simulated results (Fig. 3.9), it is visible that the calculated compensation inductors L_{Comp_1} and L_{Comp_2} are actually bigger than required to make the system resonate at 6.78 MHz. Therefore, simulations were performed reducing their values, until finding the more appropriate one, which is $L_{Comp_1} = L_{Comp_2} = 40\ \mu$H. These simulations were performed keeping all the other components as specified in the previous sections, while varying C_2 and C_3.

3.2.1 Compensation Inductors' Resistance

Furthermore, because the system is resonating at a relatively high frequency (6.78 MHz), the resistance added by the compensation inductors becomes extremely large, significantly impacting the system's efficiency on the measured results. Thus, such resistance is also added to the simulations, in order to accurately match the results obtained in reality.

Eq. (2.5) can be used to determine the resistance added by each inductor, based on the Q factor provided by the manufacturer's datasheet of each specific component. The Q factor of an inductor is inversely proportional to its ESR. However, a commercially available inductor at this frequency, with the desired inductance, can only provide a Q factor as high as 31, which would insert at least 8.7 Ω, for each inductor of 40 μH. Thus, it was decided to build an

inductor from scratch. Although this results in a physically large component, its quality factor can be improved when compared to off-the-shelf ones.

The built compensation inductors were designed using a 24 AWG wire (d = 0.51 mm), with 85 turns and diameter D = 17 mm. Using the methodology explained in Section 3.1.1, one can calculate that the inductance of the built components is equal to $L_{Comp_1} = L_{Comp_2} = 36.9234 \ \mu$H, without considering the proximity effect.

Moreover, one can calculate the ESR of the built capacitors, by applying the same method explained in Section 3.1.1, which results in a DC resistance of 0.3733 Ω and an AC resistance of 1.9981 Ω. However, the AC resistance cannot be only calculated by the previously provided method. This happens because the pitch between the turns is small when compared to the wire diameter [50]. This means that the proximity effect will extremely affect the component's resistance, due to the eddy currents that one loop of wire generates in the other ones. To solve this problem, a proximity factor (Ψ) can be used to calculate the correct ESR [50], as expressed in Eq. (3.21)

$$ESR = R_{AC} \times \Psi \tag{3.21}$$

In [50], a table is provided to determine the value of Ψ. For the designed inductor, Ψ = 3.54, which gives the final resistance of ESR = 7.0446 Ω, for each compensation inductor.
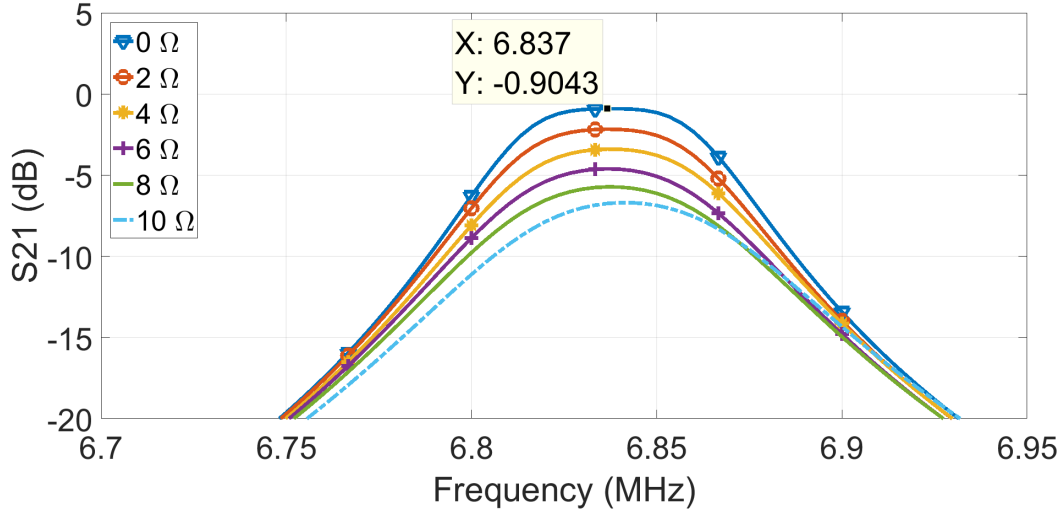
Figure 3.10: Varying resistance of the compensation inductors, while keeping $L_{Comp_1} = L_{Comp_2} = 40 \ \mu H$, and $C_2 = C_3 = 1$ nF

Fig. 3.10 provides the simulation of the entire system, maintaining the best value components previously obtained ($L_{Comp_1} = L_{Comp_2} = 40 \ \mu H$ and $C_2 = C_3 = 1$ nF). In this plot, the resistance of the compensation inductors L_{Comp_1} and L_{Comp_2} is varied simultaneously. It is visible that the ESR added by these components extremely affects the performance of the system. Therefore, the rest of the simulations presented in this chapter will account for these losses, in order to accurately match the measurement results.

3.3   Built System

Now that all components in the system have been properly described, designed and simulated, a complete system can be derived.

Fig. 3.11 provides a sketch of how this system is assembled, showing an exploded vision of the actual built system in the laboratory. The Tx-Coil and the Tx-Resonator are placed on the same plane. Then, a piece of cardboard provides a small spacing from these objects to the fragment of resonator SC_1, that is connected to the Tx-Plate (for clarity, this connection is not shown in Fig. 3.11, but in reality it is just a straight wire going through the other layers). To provide the spacing between SC_1 and the Tx-Plate, a piece of styrofoam is used. The Tx-Plate is built as a copper sheet sticked to a bigger

piece of cardboard. The receiver side of the system is built following the same logic.
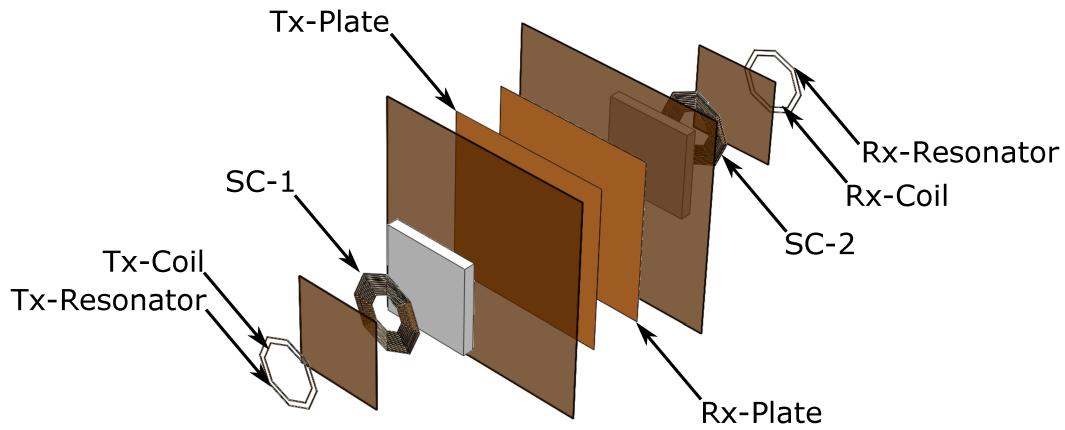
Figure 3.11: Diagram of how the system is assembled

Fig. 3.12 provides a picture of the actual built structure in the lab, based on the previously presented diagram. In Fig. 3.12a an exploded view of the system is presented, in order to show how the fragments of resonator SC_1 and SC_2 were built. Their respective styrofoam is carved with the shape of these structures. Then the 16 AWG wire is placed in the created grooves, with its feeding wire coming out at the bottom of the styrofoam (visible in Fig. 3.12c).
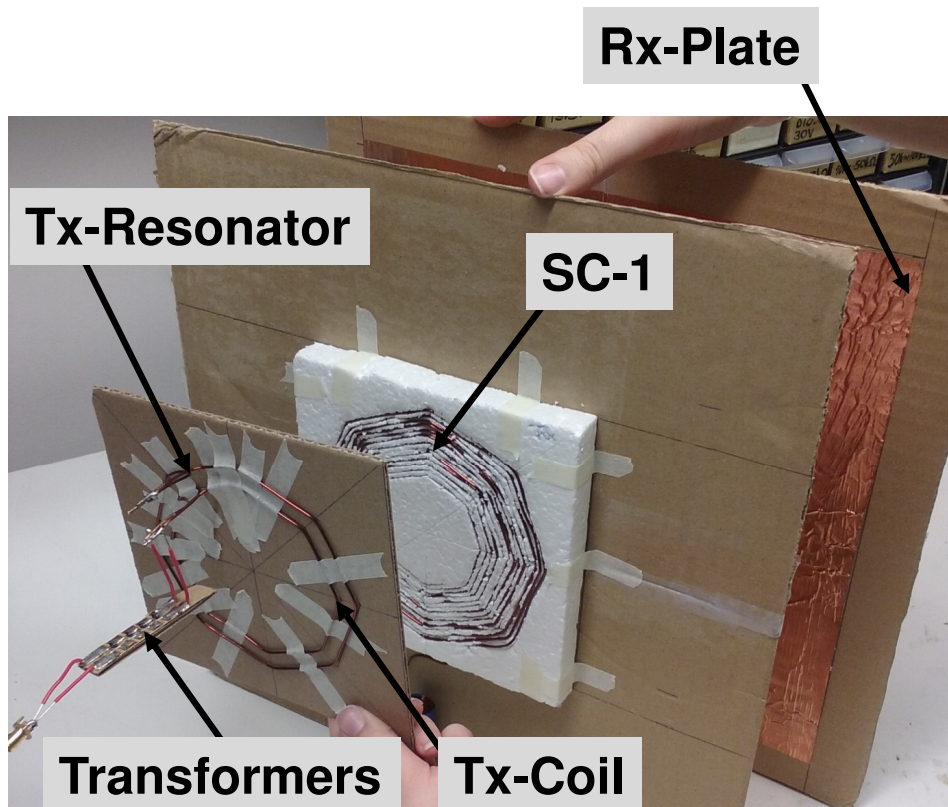
(a) Exploded View
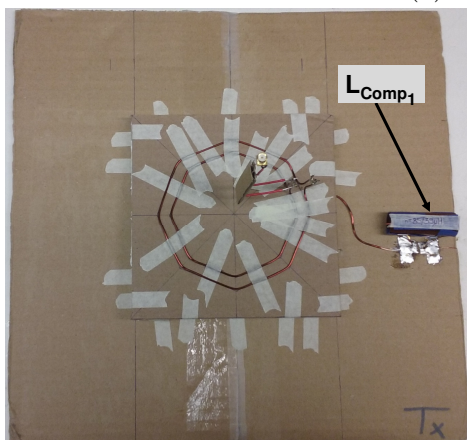
(b) Top view
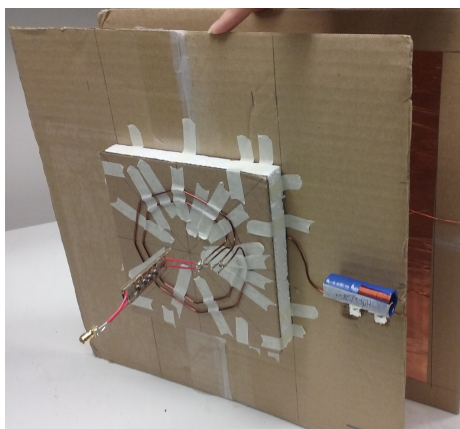
(c) Lateral view

Figure 3.12: Built system with planar coils

3.4 Results

In this section, both the simulations and measurements of the previously built system will be presented, compared and analyzed.

The simulations were performed as explained in Section 3.2, while the measurements were executed using a calibrated Rohde&Schwarz ZVL13 VNA.

3.4.1 Measurement With Transformers

In these measurements, transformers are added to the ports of the measuring device, in order to avoid current flowing back from the system to the outer surface of the feeding cable. According to [51], as the quantity of cascaded transformers increases, the amount of current that goes to the feeding cable is minimized. Moreover, in these measurements it was decided to use four 1:1 transformers cascaded to create the isolation of the system. Fig. 3.13 illustrates how these components are attached to the system.

The chosen transformers were the MABAES0060 manufactured by Macon Technology Solutions. These components were selected because of their extremely low insertion loss added to the system [52].
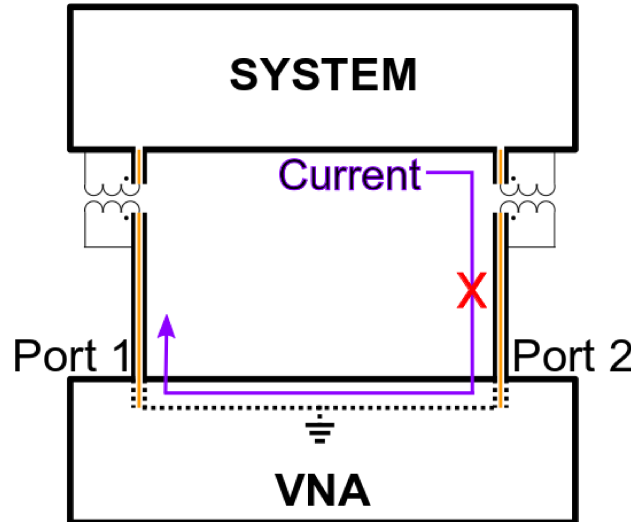
Figure 3.13: Diagram of transformers' placement

However, the added transformers will also insert losses to the system. Therefore, in order to accurately compare the measurement results to the sim-

ulated ones, this isolation circuit is de-embedded in the final presented plots in Section 3.4.2, using Matlab and the s-parameter measurements of the four cascaded transformers on each side of the system.

3.4.2 Comparison Between Simulations and Measurements

Fig. 3.14 provides the results obtained using the system described in Fig. 3.11. This image provides the results for the measured system, with and without considering the losses in the transformers. Also, it shows the ideal and real simulation results, with the latter taking into account the resistance added by the compensation inductors.
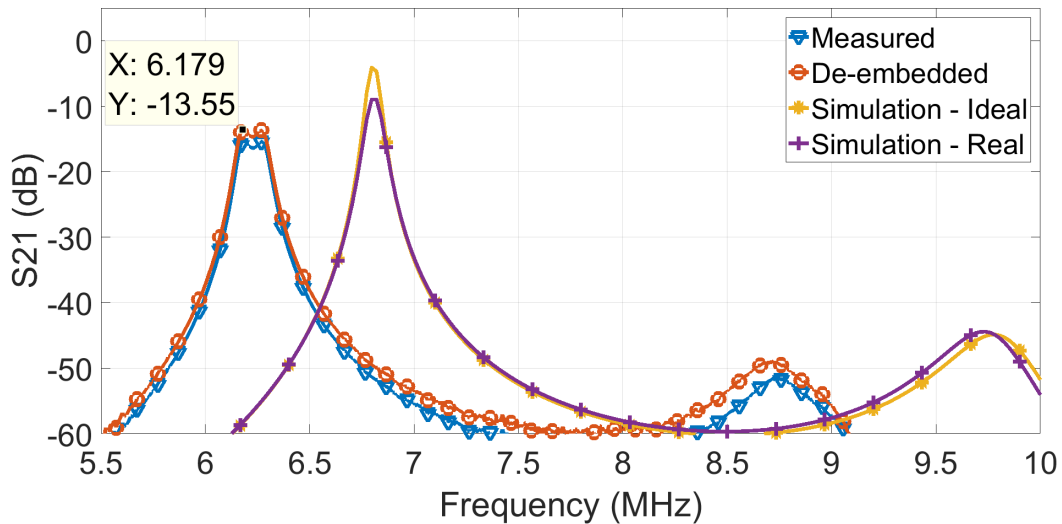
Figure 3.14: Comparison Between Simulated and Measured Results

Minor discrepancies between simulation and measurements can be seen in the previous image, and will be justified in the next section.

3.5 Addressing Measurement and Simulation Discrepancies

From the results presented in the previous section, it is visible that the peak S21 is slightly lower in the measurements, when compared to the simulations. This difference is due to uncertainties created by the handmade coils, since it

is impossible to physically build them exactly like the simulation setup using wrapped coils. In order to prove this statement, planar coils printed on a FR4 substrate (as in Fig. 3.15) were built, simulated and measured, so these uncertainties could be minimized.

(a) Top view   (b) Lateral view
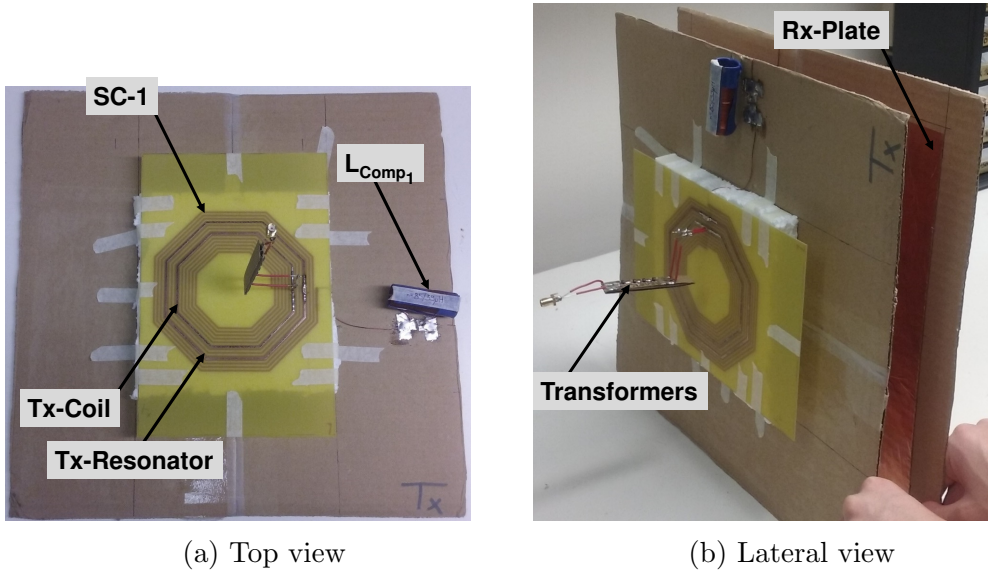
Figure 3.15: Built system with planar printed coils

Fig. 3.16 contains the results obtained with the planar printed coils. This data proves that the wrapped coils' uncertainties are responsible for the previously found discrepancies. Using the wrapped coils, the peak S21 is approximately 4 dB lower than expected from simulations. The measurements with planar printed coils provide a perfect match of the peak S21, when comparing de-embedded measurements with simulations that take into account the inductor's ESR.

However, the printed coils contribute to a less efficient system in the simulations because these structures present a higher resistance to the current. This happens due to the limited copper cross section area that they have. Thus, the wrapped coils will be used for future analysis.
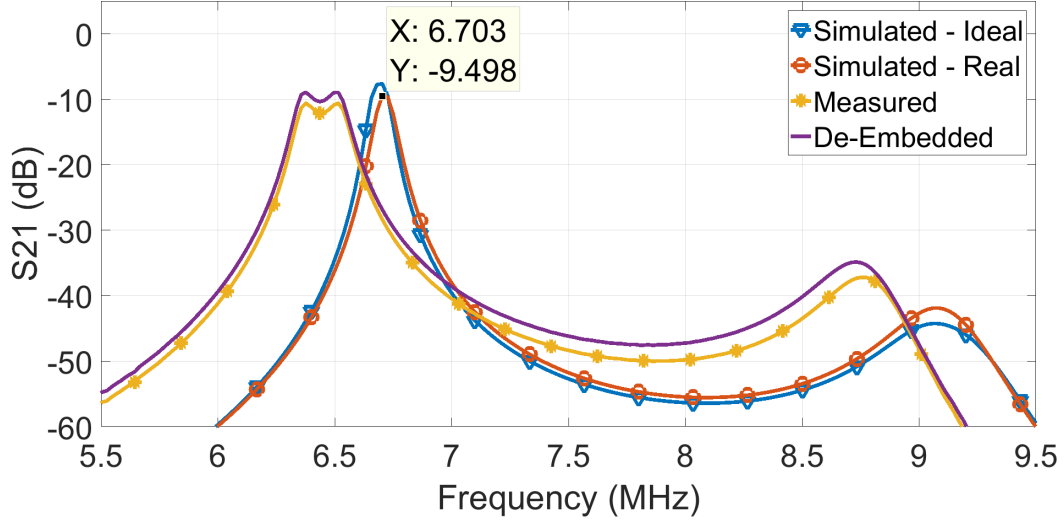
Figure 3.16: Comparison between simulated and measured results of the planar printed coils/resonators

Additionally, similar to the measurement and simulations obtained in Section 2.2.2, a small frequency shift can be observed when comparing the results. This is again attributed to the 10% tolerance of the used capacitors [30].

3.6   Field Analysis

A conductive material that has a voltage applied to it, has the possibility to create potential differences along the system. In the proposed system, an AC voltage is created on the single-conductor structure, by induction between the coils and resonators present in the system [15]. This time-varying magnetic field generates the standing wave being transferred, which creates voltage differences along the single-conductor [53]. This is due to the fact that a standing wave occurs when a time-varying wave reaches a disturbance in the system, such as the open-end of the fragments of resonator, and gets reflected on top of the same structure, creating the illusion that the wave is not moving.

One evident electric field generated in the system is the one between the capacitive plates. In this case, positive charges are concentrated on the plate that has a positive voltage applied to it at the moment, while the other plate will have negative charges on it. This charge pattern will change as the AC wave varies in time, switching which plates have the positive and negative

53

charges. Then, these charges will influence the ones in the dielectric between the capacitive plates (which is air in the presented system), polarizing and aligning them, which creates an electric field between the capacitive plates. Furthermore, when the width and length of the metallic plates is much larger than the spacing between them, a uniform distribution of charges can be assumed in the plates [54].

However, another electric field is generated in the system. According to the Faraday's law, a time-varying magnetic field generates an electric field and, as previously explained, there will be a potential difference between the two open-ends of the fragments of resonator. Thus, a significant electric field is generated between these two points, which is actually responsible for "closing" the circuit of the single-conductor structure, being represented as $C_{Parasitic}$ in previous sections.

First, in order to understand the behavior of the electric field around the structure, it is necessary to comprehend the current in the system. In regular high-Q IPT, a resonator presents zero current at its open-ends, and maximum current in the middle of the structure [45]. In the capacitive resonant single-conductor structure, the current behavior is similar, however it will differ from the previous case due to the capacitive plates added in the middle system.

Because the current is minimal at the open-ends of the single-conductor structure, the voltage will be maximum at these points. Since the wave is varying in time, the two open-ends will introduce a potential difference to the system. This electric field can then be modeled by Eq. (3.22), where q is the charge held by a capacitor, V is the voltage applied to it, E is electric field generated by it and d is the thickness of the dielectric.

$$C = \frac{q}{V} = \frac{q}{Ed} \qquad (3.22)$$

Furthermore, it is visible that the electric fields around the structure can be relatively high because $C_{Parasitic}$ is extremely small, specially considering that the input power used during the simulations on HFSS was only 1W. As presented in [55], the IEEE C95.1-2005 general public exposure limit of

electrical field intensity, at 6.78 MHz, is close to 100 V_{rms}/m. With the electric field intensity around the proposed structure easily surpassing 1000 V/m (as depicted in Fig. 3.17), the designed system is obviously mainly suitable for low power applications (below 100 mW), in order to guarantee the compliance to safety standards for human exposure.
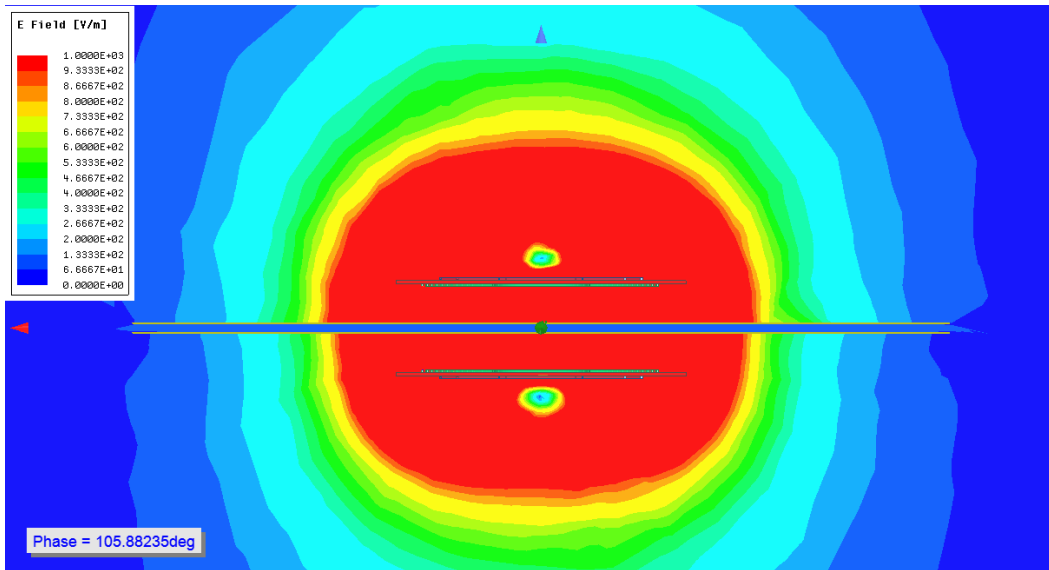
Figure 3.17: Example of electric field intensity around the final structure

The objective of the present document is to analyze the behavior of the capacitive resonant single-conductor structure, and show its performance when transferring power to devices with a metallic case. Therefore, electric field minimization and optimization are out of the scope of this thesis.

In future studies, a few options can be explored to reduce the electric field around the structure, such as: increasing the parasitic capacitance between the two open-ends of the fragments of resonator, redesigning the plates to restrain the fields to a specific area, or adding shields to the system.

3.7 Chapter Summary

The final capacitive resonant single-conductor structure was explained in this chapter. The parts derived in Chapter 2 were utilized, with the addition of the single-conductor path. Each remaining parameter of the system was explained

and simulated in this chapter, such as the self-inductance, self-capacitance and ESR of the fragments of resonator, the parasitic capacitance of the system, and the compensation inductors.

Moreover, simulations were performed with the complete system in order to optimize the previously obtained values for each component. Then, the entire final capacitive resonant single-conductor structure was built and measured.

The measurement and simulation results are presented and compared, explaining any possible difference found between them. Lastly, the electric field analysis of the system is performed.

Chapter 4

Varying Capacitive Plates

This chapter contains possible variations to the system proposed previously. Firstly, the distance between transmitter and receiver plates is varied. Then, with the system back to the initial distance (5 mm), asymmetric plates are tested in the system, having the receiver significantly smaller than the transmitter. Finally, further designs are tested for the transmitter plate, in order to increase the system's efficiency when the plates do not have the same size.

4.1 Varying Distance Between Capacitive Plates

Firstly, the distance between Tx- and Rx-Plates is analyzed, while keeping all the other parameters of the system constant. Thus, in this case, $L_{Comp_1} = L_{Comp_2} = 40\ \mu$H. The capacitors C_2 and C_3 are maintained at 1 nF, which was the best simulated result in Section 3.2. Fig. 4.1 contains the obtained peak S21 simulation and measurement results, over different distances between the plates. Again, discrepancies when comparing measurements and simulations can be explained as described in Section 3.5.
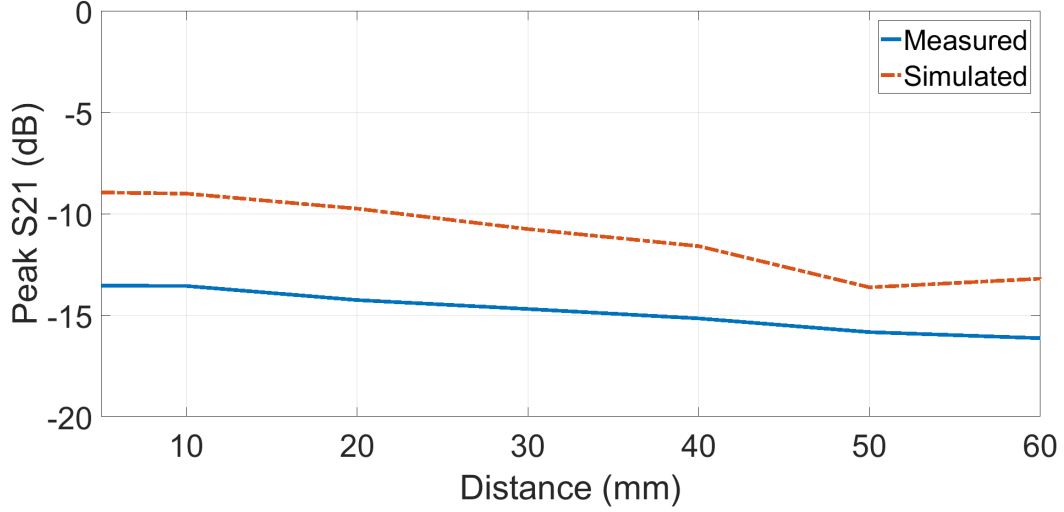
Figure 4.1: Peak S21 of the simulated system varying distance between plates. The inductors L_{Comp_1} and L_{Comp_2} are kept as 40 μH, while C_2 and C_3 are equal to 1 nF

Since no component was changed in the system, as the distance between plates increases, the efficiency drops. In order to improve this value, it is necessary to redesign the components of the system based on the fact that C_{Plates} decreases as the plates are placed farther apart. However, these is a limit to the improvement possible due to variation in the system's components.

4.2 Smaller Receiver Plate

When the receiver plate has its dimensions reduced, the capacitance C_{Plates} will decrease based on Eq. (2.14), which means that the resonance frequency will increase if no component is changed. Fig. 4.2 illustrates the system with asymmetric capacitive plates. The receiver plate is conceived as a 20x20 cm plate, while the size of the transmitter plate is varied to understand the system's behavior.
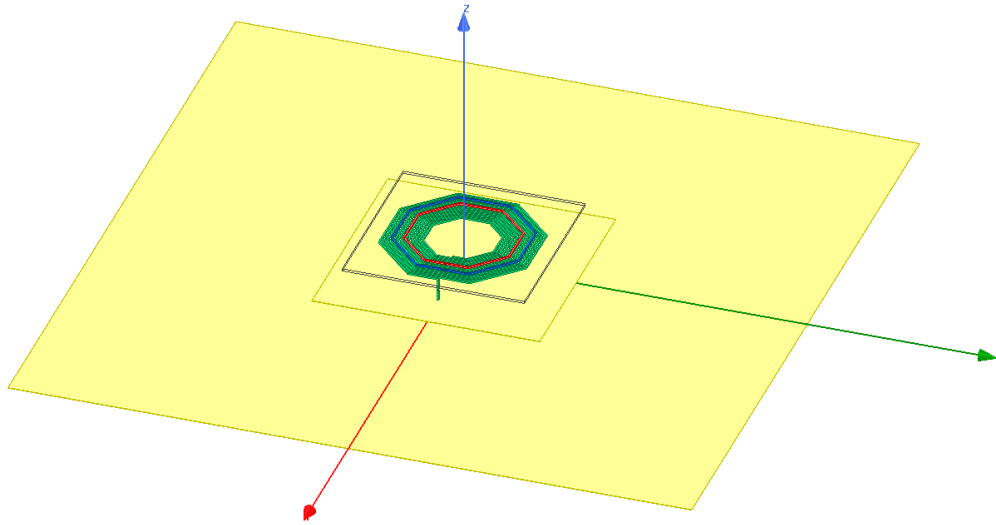
Figure 4.2: Simulated system with asymmetric plates. The receiver plate has dimensions of 20x20 cm, while the transmitter plate will be varied

Fig. 4.3 presents the simulation results for the system provided in the previous image. In this simulation, the inductors were kept constant at L_{Comp_1} = L_{Comp_2} = 40 μH, while $C_2 = C_3 = 1.5$ nF. Then, the transmitter plate had its dimensions increased equally in the x and y directions, always resulting in a Tx-Plate with a square shape. Moreover, for simplicity, these simulation results do not take into consideration the resistance added by the compensation inductors.
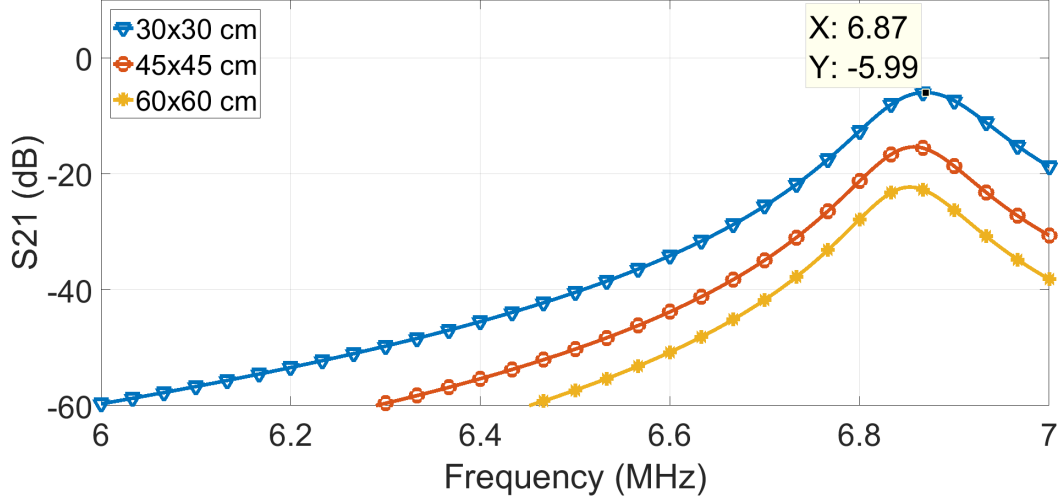
Figure 4.3: Simulation of the system with asymmetric plates. The receiver plate is kept with 20x20 cm, while the dimensions of the Tx-Plate are varied. The compensation inductors L_{Comp_1} and L_{Comp_2} are kept with 40 μH, and the resonant capacitors are $C_2 = C_3 = 1.5$ nF

In the previous image, it is visible that the smaller capacitance between the plates resulted in a higher resonant frequency for the system. Additionally, if no other part of the system is changed, it is noticeable that a bigger plate on the transmitter side will only impact the efficiency of the system, not changing its frequency response. This happens because the overlapping area between the plates is constant in all these cases, not altering C_{Plates}.

In order to adjust the system to the new value of C_{Plates}, the inductors L_{Comp_1} and L_{Comp_2} must be changed to compensate for this variation. Fig. 4.4 shows the impact of changing the compensation inductors. When the Rx-Plate is reduced, the capacitance between the plates decreases, which means that higher compensation inductors are required to achieve resonance at the desired frequency. However, there is a limit of improvement in the S21 that can be achieved with this approach. Again, the capacitors C_2 and C_3 are maintained as 1.5 nF. The receiver plate is kept with 20x20 cm, as in the previous example, while the transmitter plate has the greatest dimensions ever simulated (60x60 cm). Again, the resistance added by the compensation inductors is not considered in these results.
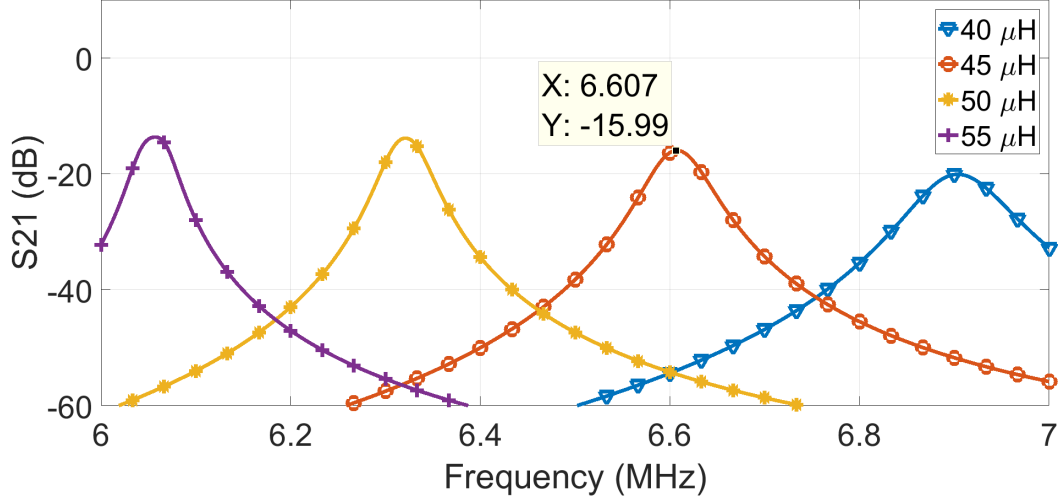
Figure 4.4: Simulation of the system with asymmetric plates. The receiver plate is kept with 20x20 cm, while the dimensions of the Tx-Plate are maintained as 60x60 cm. The compensation inductors L_{Comp_1} and L_{Comp_2} are varied simultaneously, and the resonant capacitors are $C_2 = C_3 = 1.5$ nF

The improvement limit achievable by adjusting the compensation inductors happens because of the electric fields that close the circuit (represented as $C_{Parasitic}$) flowing between the transmitter and receiver open-ends of the fragments of resonator. As bigger the transmitter plate gets when compared to the receiver, the longer the path that electric fields must overcome to close the circuit, which means that more losses will occur in the system due to minimized closed field lines.

Fig. 4.5 depicts an example of electric field comparison. The image 4.5a shows the fields for a system where both plates have the same size (45x45 cm). It is visible that the fields go around the plates and close the circuit, guaranteeing the higher efficiency in this case. The image 4.5b shows a system with the same conditions of the first one, but now the receiver plate is reduced to 20x20 cm. From this case, it is obvious that the magnitude of the field that reaches the receiver is smaller than the previous case.
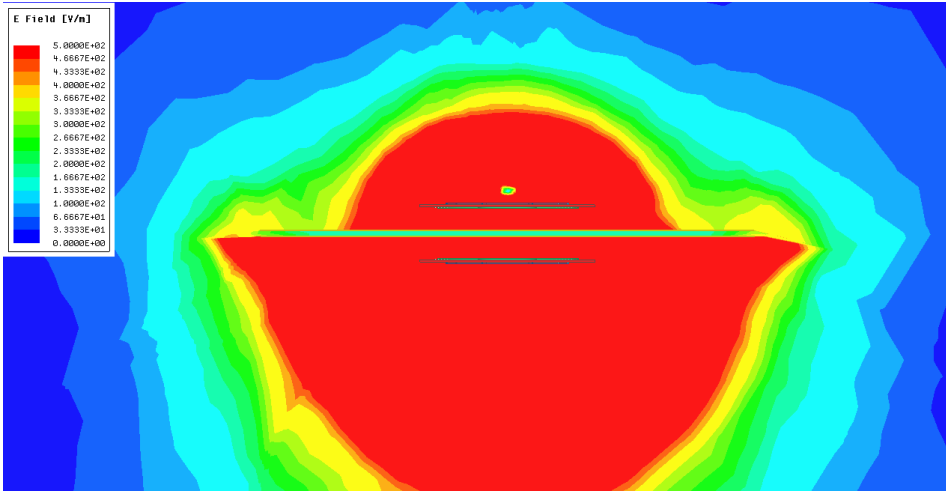
(a) Symmetric plates
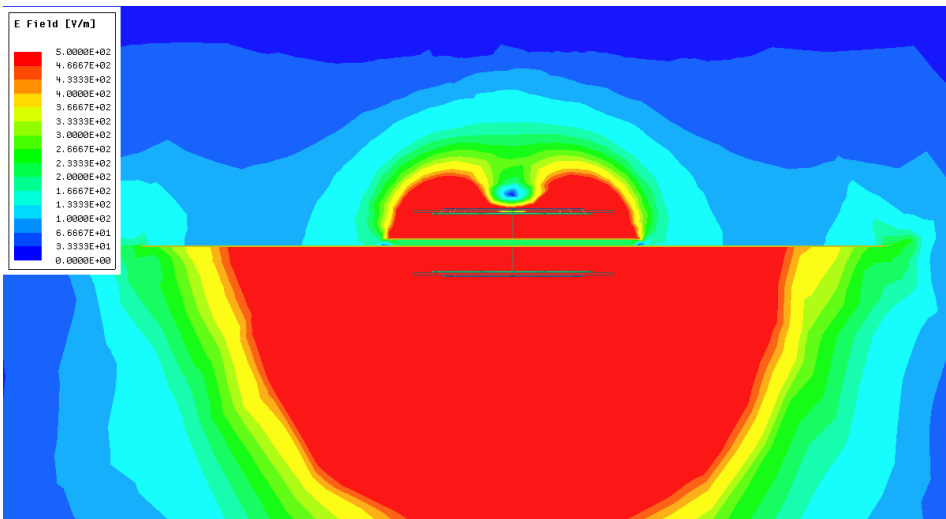
(b) Asymmetric plates

Figure 4.5: Electric field comparison between symmetric and asymmetric plates

Therefore, in order to have a high efficient system with a transmitter significantly larger than the receiver, a different approach must be used. One option to overcome this problem is presented in the next section.

4.3 Transmitter Plate Conceived as Multiple Transmitter Cells

In this section, a different structure is proposed in order to allow the use of a transmitter plate that is relatively larger than the receiver one, while keeping the efficiency similar to the case when both plates have the same size. The transmitter was divided into multiple Tx-Cells, with gaps between them to allow the field to pass through the middle of the plate, as depicted in Fig. 4.6.
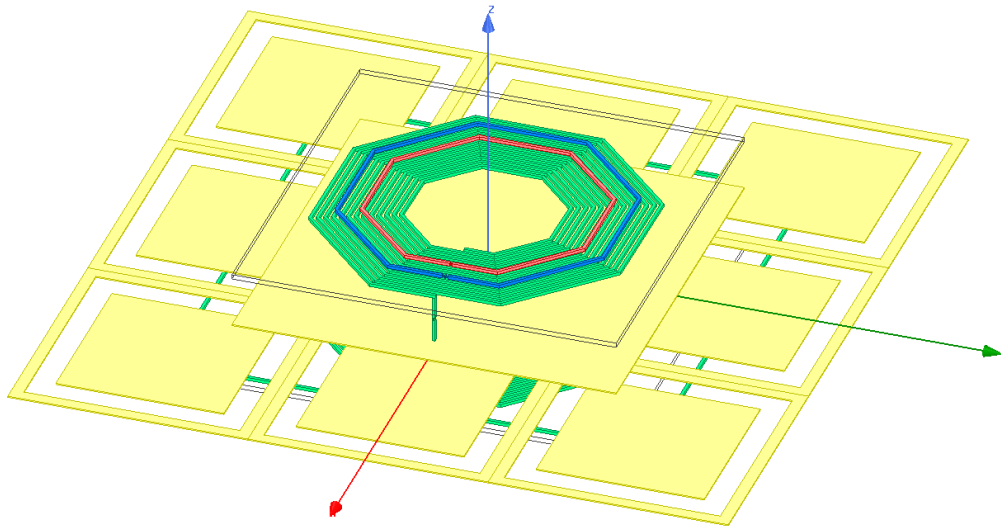
Figure 4.6: Simulated system with multiple Tx-Cells in a 3x3 configuration. Each Tx-Cell has a 10x10 cm capacitive plate, with a 1 cm gap to a metallic ring of 5 mm width

In the previous image, a transmitter composed of multiple cells is presented. Each one of these cells is composed of a 10x10 cm metallic plate. Then, each plate is surrounded by a metallic ring that has 5 mm of width, having an air gap of 10 mm between the ring and the plate.

The theory behind this system is that the capacitive plates are responsible for transferring the forward electric field, while return electric field (generated

by the parasitic capacitance $C_{Parasitic}$) will be guided by the metallic rings to pass through the placed air gaps [56]. This allows a shorter return path to the fields, increasing the system's efficiency. In the system proposed in Fig. 4.6, the fragment of resonator SC_1 is connected in series with the compensation inductor L_{Comp_1}. This inductor is then directly connected to all the plates of each Tx-Cell, in a parallel configuration.

At the beginning, this system variation is conceived using the previously defined values of $L_{Comp_1} = L_{Comp_2} = 40\ \mu$H, and $C_2 = C_3 = 1.5$ nF, without taking into account the resistance added by the inductors. Then, the inductance of the system is varied (as depicted in Fig. 4.7). Since the capacitance between the plates C_{Plates} is smaller now, an increase in the compensation inductors is expected.
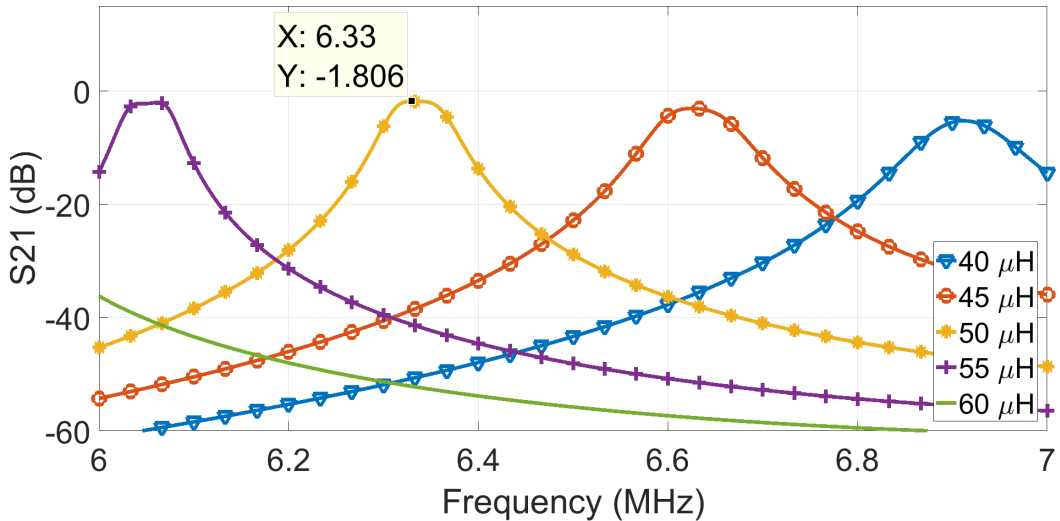
Figure 4.7: Varying compensation inductors of the 3x3 structure, while keeping the resonating capacitors fixed at 1.5 nF

From the previous image, it is visible that the best efficiency occurred when the compensation inductors were equal to 50 μH, resulting in a S21 = -1.806 dB. However, the resonant frequency is slightly lower than desired. Thus, further variation of parameters is performed with the system by adjusting the resonating capacitors C_2 and C_3, as shown in Fig. 4.8.
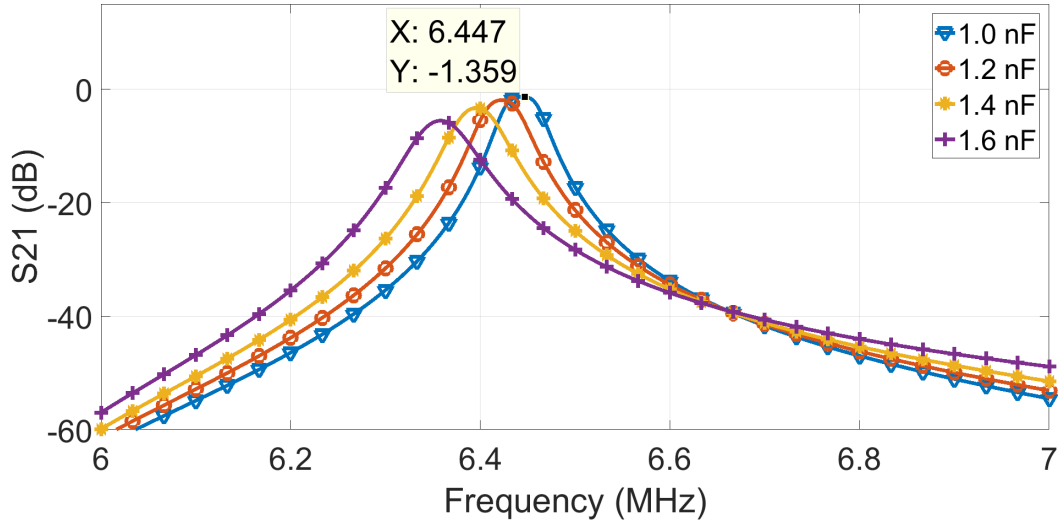
Figure 4.8: Varying resonating capacitors of the 3x3 structure, while keeping the compensation inductors fixed at 50 μH

The previous simulation results show that resonating capacitors of $C_2 = C_3$ = 1nF are able to increase the S21 of the system to -1.359 dB, while shifting the frequency towards the desired one.

4.3.1 Increasing Quantity of Transmitter Cells

Since the 3x3 system, containing nine transmitter cells in total, was able to efficiently transfer power to the receiver, an increase in the number of transmitter cells is performed. Now, a 5x5 system will be analyzed, containing 25 transmitter cells. In this version of the system, all the transmitter cells are exactly identical to the ones described in the previous section. Fig. 4.9 depicts the simulated 5x5 system.
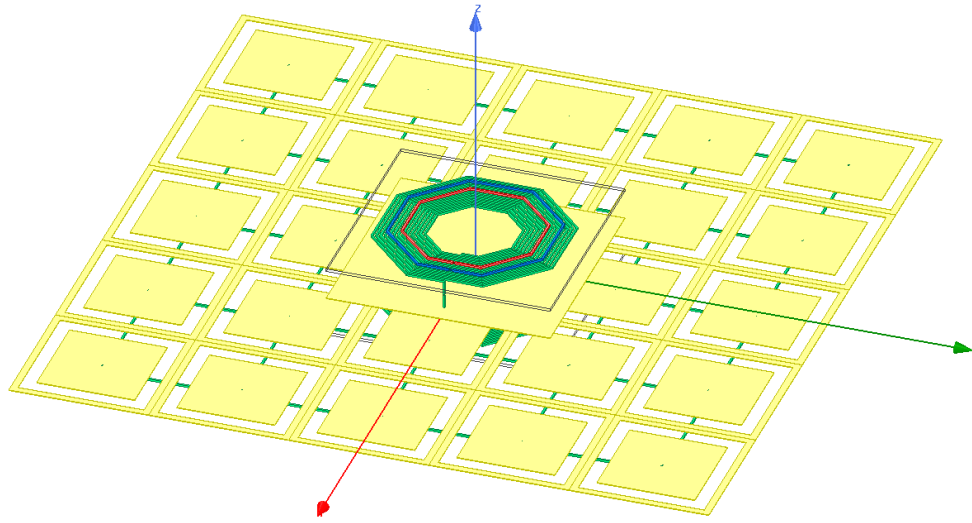
Figure 4.9: Simulated system with multiple Tx-Cells in a 5x5 configuration. Each Tx-Cell has a 10x10 cm capacitive plate, with a 1 cm gap to a metallic ring of 5 mm width

Fig. 4.10 contains the preliminary simulation results for the system with 25 transmitter cells. Firstly, as in the previous section, only the compensation inductors are changed, while keeping the capacitors C_2 and C_3 constant at 1 nF, which was the best capacitor value obtained for the previously explained 3x3 system.
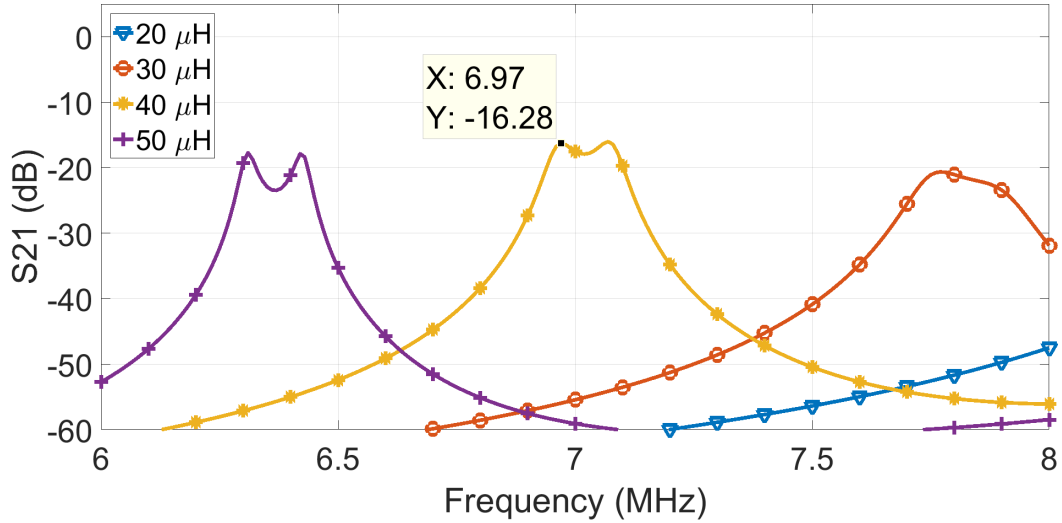
Figure 4.10: Varying compensation inductors of the 5x5 structure, while keeping the resonating capacitors fixed at 1 nF

In the previous image, it is visible that the efficiency dropped to values that cannot be improved by only changing the inductors and capacitors in the system. Similarly to the system with a solid plate, the electric field has to travel a significant distance to reach the other side of the system, creating losses. Thus, variations on the capacitor will not be showed, since it was already proven previously that changing this component alone would not be enough to bring the efficiency back up.

Adding Multiple Compensation Inductors

In order to overcome the losses still present in the 5x5 topology, a new approach to the same system is tested. Before, only one single compensation inductor L_{Comp_1} was connected to all Tx-Cells. This makes the receiver resonant with all of these structures simultaneously. Therefore, the electric field still travels to the end of the edge of the transmitter structure.

Thus, one can assume that if the receiver is only resonant to the transmitter cells that are placed immediately below it, the fields would not propagate to the very last cell of the transmitter unit. In order to achieve such goal, the compensation inductor L_{Comp_1} is fragmented into multiple compensation inductors, one for each Tx-Cell.

Then, simulations are performed in order to determine the best value for these new multiple compensation inductors on the transmitter side, while maintaining the receiver inductance as before ($L_{Comp_2} = 40 \ \mu$H). These results are provided in Fig. 4.11. It is important to clarify that both resonant capacitors C_2 and C_3 are always altered simultaneously. The compensation inductors are only evaluated separately in the present section.
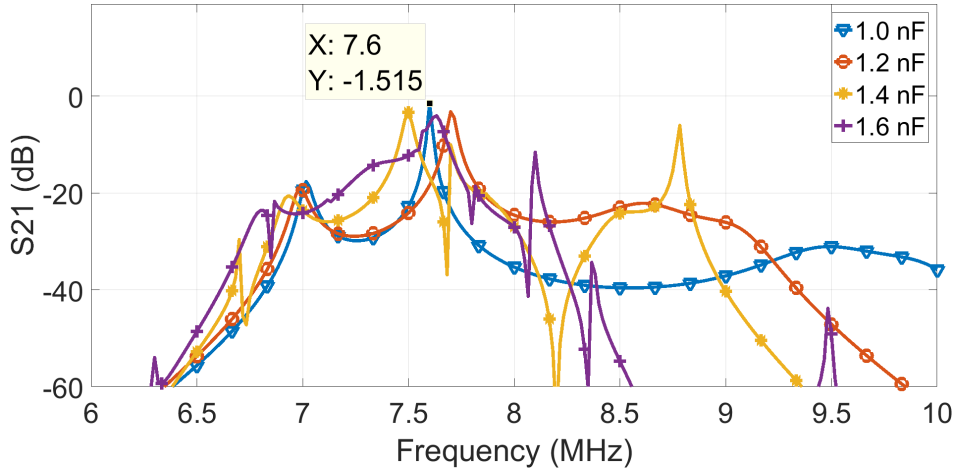
(a) Inductance of each one of the multiple compensation inductors is equal to 30 μH
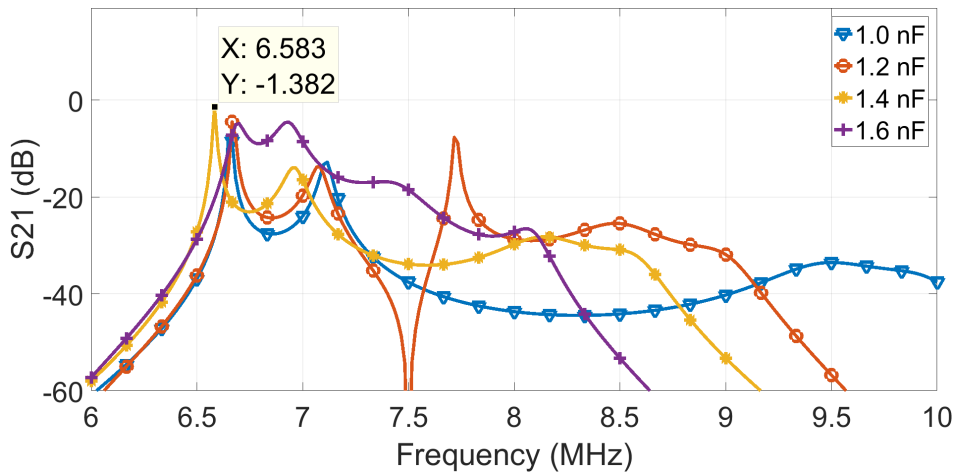
(b) Inductance of each one of the multiple compensation inductors is equal to 40 μH

Figure 4.11: Simulations of the 5x5 system, fragmenting L_{Comp_1} into multiple compensation inductors. Both resonant capacitors are varied simultaneously, while the compensation inductor $L_{Comp_2} = 40 \ \mu$H

These results evidentiate that it is possible to achieve high efficiency with

a transmitter structure significantly larger than the receiver device. Also, in the future, the desired frequency of 6.78 MHz can be easily obtained by fine tuning the values of the compensation inductors and resonant capacitors to values between the ones provided in Fig. 4.11a and Fig. 4.11b.

Additionally, it is important to mention that although the efficiency of the 5x5 system with multiple compensation inductors is impressive, this result does not take into consideration the resistance added by the inductors to the system. Since the quantity of inductors increases significantly, and their values would result in a high ESR at this frequency, in reality, the performance of the system would be remarkably worse than the ideal case.

4.4 Varying Position of Receiver

The final analysis of the capacitive resonant single-conductor system presented in this document is the variation of the receiver structure positioning on top of a transmitter unit significantly larger than the receiver device.

Such investigation is made using the 3x3 Tx-Cells transmitter structure obtained in Section 4.3, and the 5x5 Tx-Cells transmitter structure using multiple inductors obtained in 4.3.1.

4.4.1 3x3 Structure

The position of the receiver device is simulated in this section for the 3x3 transmitter structure. Considering the center of the middle cell as the origin of the system, the center of the receiver is varied from this point. In Fig. 4.12, the farthest simulated position from the origin is depicted. In this case, the distance from the center of the receiver to the system's origin is 70 mm.
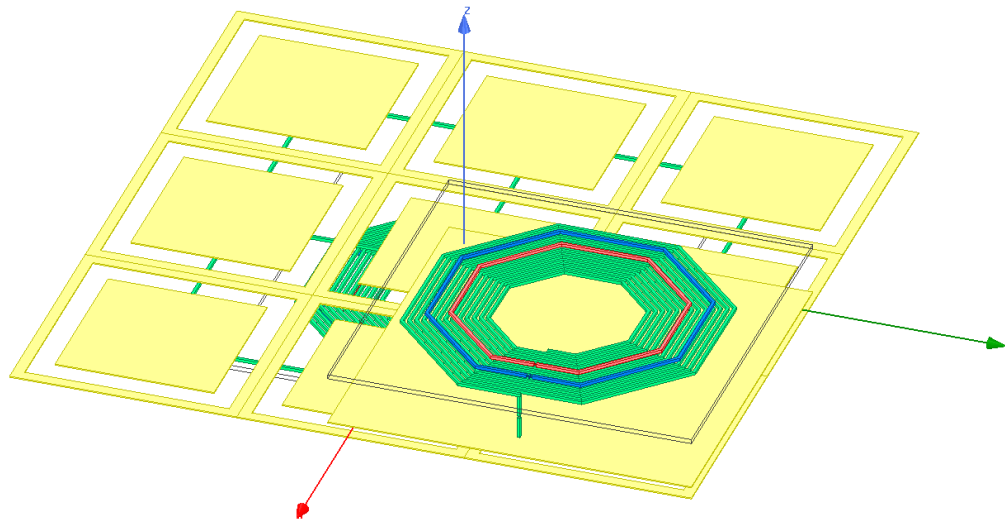
Figure 4.12: Simulation of the 3x3 system, varying the receiver's position

Fig. 4.13 shows the simulated results obtained over the entire distance from the system's origin to its edge, in a diagonal manner. In other words, when the receiver is moved, it will have a placement delta equal in the x and y directions simultaneously.
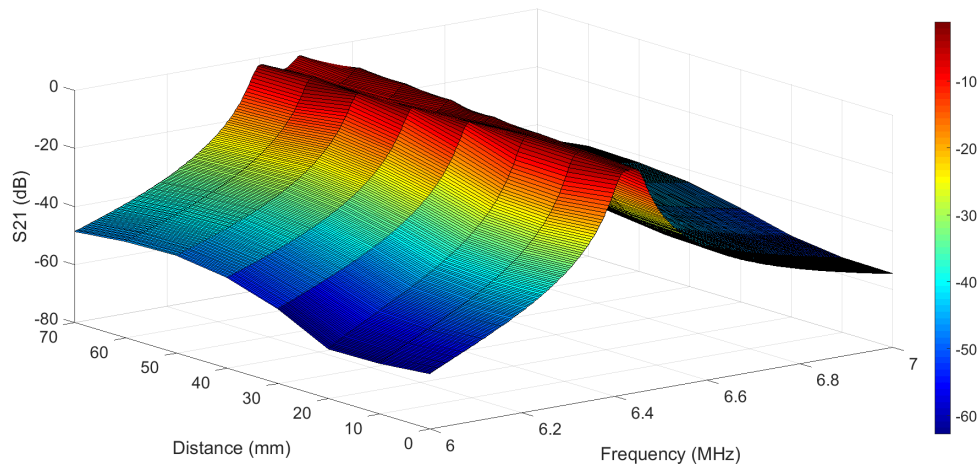
Figure 4.13: 3x3 System Varying Receiver Position

The previous result proves that no matter the distance that the receiver is placed from the center, its efficiency will remain significantly high.

4.4.2   5x5 Structure With Multiple Inductors

Now, the same analysis made for the 3x3 system is performed for the 5x5 system, using multiple compensation inductors.

The receiver is moved in the same fashion of the previous section. The maximum variation (illustrated in Fig. 4.14) corresponds to a delta of 150 mm in the x and y directions, simultaneously.
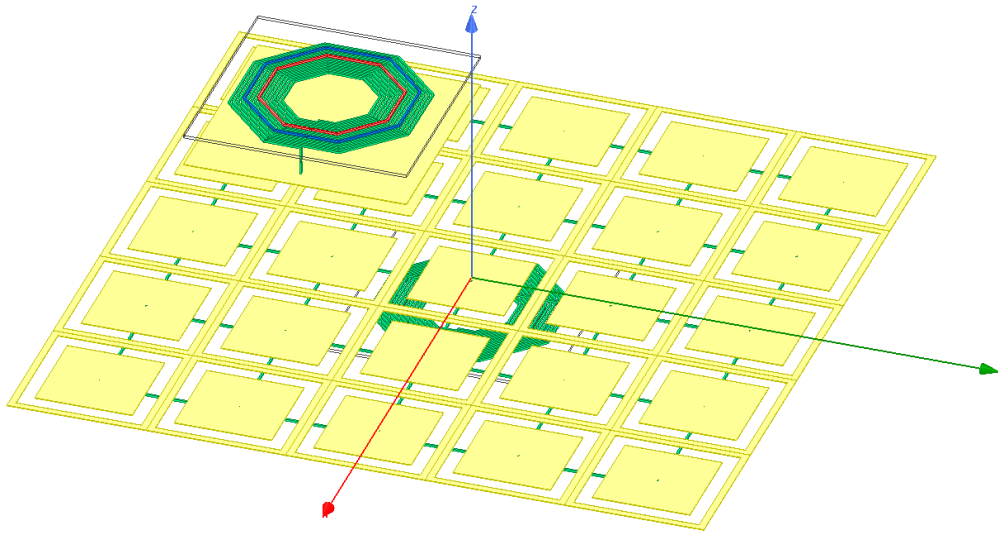
Figure 4.14: Simulation of the 5x5 system with multiple compensation inductors, varying the receiver's position

Fig. 4.15 shows the simulated results obtained over the distance from the system's origin to its edge, in a diagonal manner. Again, it is noticeable that the receiver can be placed anywhere on top of the transmitter structure, and still be able to receive a significant amount of power.
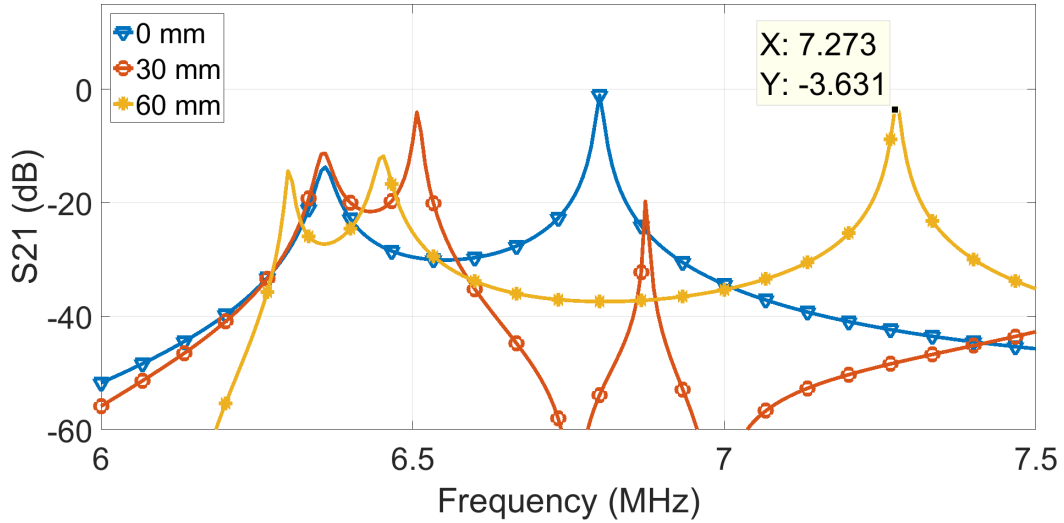
Figure 4.15: 5x5 System Varying Receiver Position

However, as visible in the previous image, different locations on top of the 5x5 structure create changes in the resonant frequency of the system. This is due to the fact that depending on where the receiver is standing, it will be on top of a different quantity of transmitter cells, which would change C_{Plates}. Therefore, an adaptive matching circuit is of interest to bring the resonance back to the desired one. This circuit will be explained in the next chapter, and applied to a regular 2-coil inductive link, to show its behavior.

4.5 Chapter Summary

Further variations of the capacitive resonant single-conductor structure were performed in this chapter. Firstly, the distance between the capacitive plates was altered, in order to demonstrate the drop in efficiency as this gap increases.

Then, the system was tested using asymmetric plates, having a receiver device much smaller than the transmitter. These results show that the structure is not capable of maintaining a high efficiency in this case, due to the fact that the electric fields around the system would have to transpose a larger distance to close the circuit, generating losses on the way.

In order to allow efficient power transfer using asymmetric plates, a different approach is explored. The transmitter plate is redesigned as multiple

transmitter cells in parallel. Such structures have air gaps that permit a shorter path for the electric field.

Furthermore, the addition of multiple compensation inductors is studied in the case where multiple Tx-Cells are used. These inductors allow the receiver to only resonate with the transmitter cells that are directly bellow it, so that the electric fields would not have to travel all the way to the edge of the transmitter unit.

Chapter 5

Adaptive Impedance Matching

In order to develop a more efficient WPT system, it is desirable to utilize matching and tuning circuits. However, the source, load and coils impedance might change depending on a variety of conditions, such as: different receiver devices loading the system, strange objects in the vicinity of the structure, user touching the system, etc. Thus, an adaptive matching circuit is of interest.

5.1 Developed Circuit

Most of adaptive matching circuits are composed of a bank of capacitors activated by switches, like MOSFET's or relays. Although such approaches provide relatively low complexity, there are a few disadvantages in using them. First, in order to obtain a system highly adaptable, multiple capacitor values and switches are required [57], generating a circuit that occupies a significant PCB area [58]. Additionally, switches, relays and MOSFET's [57]–[59] usually have a limited lifetime, which is not desired for real applications. Finally, these components rarely provide good efficiency, while working at medium and high power and at the MHz frequency range [57].

Additionally, varactors are widely used to perform adaptive matching and tuning. Varactors are voltage controlled components, that change their capacitance based on the voltage that is applied to them. However, such components have extremely limited capacitance ranges, are not able to handle significant amounts of power, and cannot be used in wide frequency ranges [60], [61]. Thus, a different approach using transistors is going to be explored in this

thesis.

Transistor-controlled variable capacitors (TCVC's) were recently presented in literature [62]. However, this technology has only been explored as a way to create a variable-controlled oscillator (VCO). Therefore, a circuit adaptation is going to be proposed in order to apply the concept provided by [62] to perform coils matching and tuning.

The developed circuit is provided in Fig. 5.1. One can observe that due to the reduced number of components in the circuit, its complexity and size are relatively minimized. Furthermore, such technique provides continuous variation in the capacitance, opposed to the flat steps of variation provided by regular switching capacitor banks.
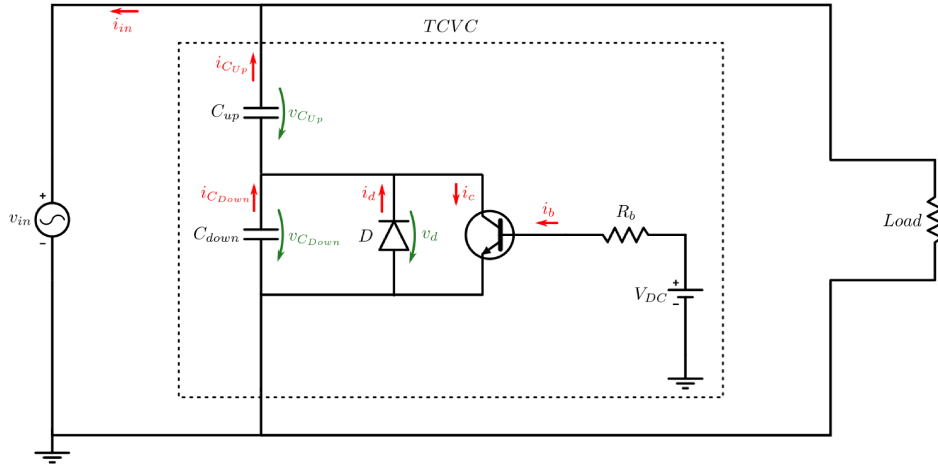
Figure 5.1: TCVC Schematic

Basically, the capacitance variation is obtained by changing the equivalent capacitance (C_{Eq}) that the TCVC circuit provides, by changing the amount of time that the transistor is conducting current. As the base voltage V_{DC} increases, the amount of time that the transistor conduces also increases, if this component is working on its active region. When the applied voltage reaches a level that corresponds to the maximum collector current, the overall capacitance of the TCVC circuit will be maximum, which means that $C_{Eq} = C_{up}$. If V_{DC} is reduced to bellow its cut-off region, the transistor will not conduct at any time, which makes C_{Eq} equal to C_{up} and C_{down} in series. Therefore, the higher the control voltage is, the larger C_{Eq} becomes.

75

5.1.1 Theoretical Modeling of the Adaptive Matching Circuit

In the proposed adaptive matching circuit, it is desirable to establish the relation between the continuous voltage V_{DC} applied to the base of the transistor and the equivalent capacitance C_{Eq} that this voltage will create on the circuit. In order to find the relationship between these two variables, a method similar to the one used in [62] will be utilized.

Firstly, it is important to determine that the transistor must be working on its active region in order for this circuit to work. Therefore, the following equations can be used:

$$I_b = \frac{V_{BB} - V_{BE}}{R_B} = \frac{V_{DC} - V_{BE}}{R_B} \tag{5.1}$$

$$I_c = \beta I_b = \beta \frac{V_{DC} - V_{BE}}{R_B} \tag{5.2}$$

In the previous equations, I_b and I_c are the currents applied to the base and collector of the transistor, respectively. V_{BB} is the voltage applied to the base of the transistor, which will be related to the continuous voltage V_{DC} and the base resistor R_B. The voltage V_{BE} is the one across the base and the emitter of the transistor. Lastly, β is the current gain between the collector and the base of this component.

The proposed circuit has basically two possible states: when the diode is on, and when the diode is off. Fig. 5.2 shows the equivalent circuit of both cases.
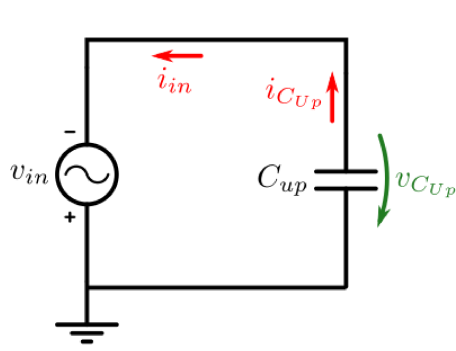
(a) TCVC schematic when the diode is on
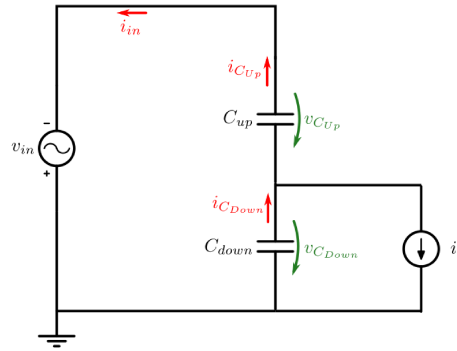
(b) TCVC schematic when the diode is off

Figure 5.2: TCVC schematic in both states of the circuit

Because the diode is conducting during the negative cycle of the AC source, the voltage v_{in} is inverted to account for this case in the previous images.

Fig. 5.3 displays the typical waveforms for different voltages over the circuit presented in Fig. 5.1.
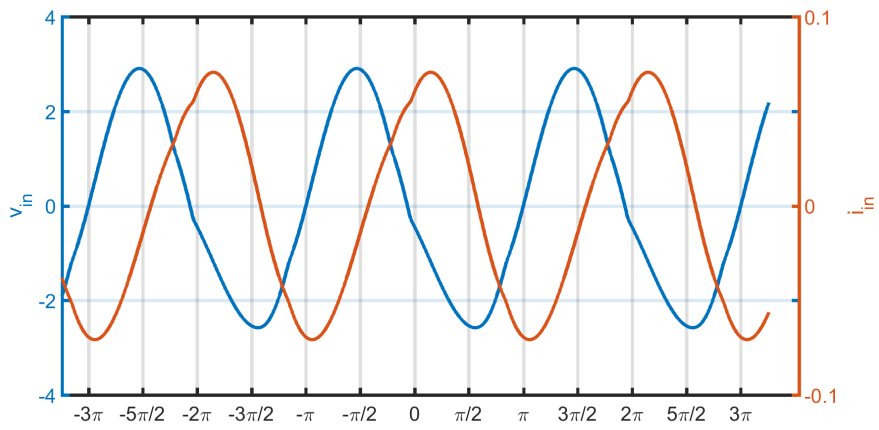
(a) Voltage (v_{in}) and current (i_{in}) provided by the AC source
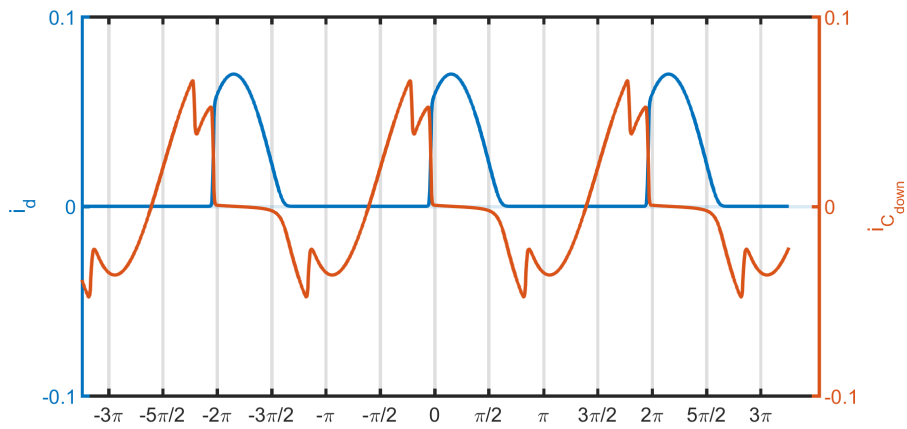
(b) Currents over the diode (i_d) and over the capacitor C_{down} ($i_{C_{down}}$)
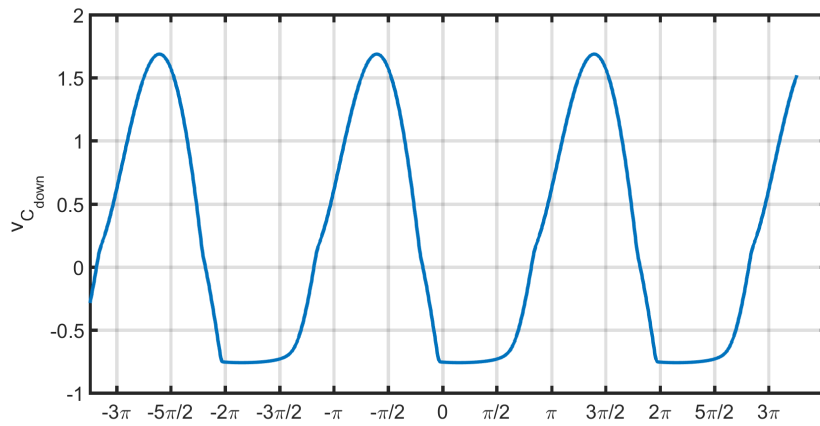
(c) Voltage over the capacitor C_{down} (v_{down})

Figure 5.3: Typical Waveforms of the Circuit

From the previous waveforms and circuits, one can observe that the diode will stop conducting when i_{in} reaches zero; this will occur when v_{in} achieves its minimum at $t = \pi/2\omega$. The total time that the diode conducts is expressed by Eq. (5.3).

$$T_{con} = t_{off} - t_{on} \tag{5.3}$$

When the diode is off (as in Fig. 5.2b), the transistor is modeled as a current source on the circuit. Assuming that $v_{in}(t) = -A_{in}sin(\omega t)$, the following equations can be obtained:

$$v_{in}(t) = v_{C_{up}}(t) + v_{C_{down}}(t) \quad \therefore \quad \frac{dv_{in}(t)}{dt} = \frac{dv_{C_{up}}(t)}{dt} + \frac{dv_{C_{down}}(t)}{dt} \tag{5.4}$$

$$\frac{dv_{in}(t)}{dt} = \omega(-A_{in})cos(\omega t) \tag{5.5}$$

$$i_{C_{down}}(t) = i_{in}(t) + i_c(t) \tag{5.6}$$

$$\frac{dv_{C_{down}}(t)}{dt} = \frac{i_{in}(t) + i_c(t)}{C_{down}} \quad \therefore \quad i_{in}(t) = \frac{dv_{C_{down}}(t)}{dt}C_{down} - i_c(t) \tag{5.7}$$

$$\frac{dv_{C_{up}}(t)}{dt} = \frac{i_{in}(t)}{C_{up}} = \frac{dv_{C_{down}}(t)}{dt}\frac{C_{down}}{C_{up}} - \frac{i_c(t)}{C_{up}} \tag{5.8}$$

Substituting equations (5.5) and (5.8) in Eq. (5.4), one can obtain the following equation:

$$\frac{dv_{C_{down}}(t)}{dt} = \frac{\omega A_{in}cos(\omega t)C_{up} + i_c(t)}{C_{up} + C_{down}} \tag{5.9}$$

Integrating the previous equation, gives the following expression:

$$v_{C_{down}}(t) = \frac{A_{in}sin(\omega t)C_{up}}{C_{up} + C_{down}} + \frac{I_c}{C_{up} + C_{down}}t + K \tag{5.10}$$

Now, it is necessary to determine the value of the constant K in the previous equation. Since the diode is off at this stage, from the waveforms presented

79

in Fig. 5.3, one can observe that for this condition $v_{C_{down}} = 0$ and $t = -3\pi/2\omega$. This gives the following expression:

$$K = \frac{-A_{in}C_{up} + I_c(3\pi/2\omega)}{C_{up} + C_{down}} \tag{5.11}$$

In order to find when the diode starts to conduct (t_{on}), it will be necessary to apply the Taylor series to Eq. (5.10), which gives that $sin(\omega t_{on}) = \omega t_{on}$. Additionally, the voltage $v_{C_{down}}$ will be equal to zero at this stage as well. This gives the following expression:

$$t_{on} \approx -\frac{K(C_{up} + C_{down})}{A_{in}\omega C_{up} + I_c} \tag{5.12}$$

Substituting equation (5.12) and $t_{off} = \pi/2\omega$ on Eq. (5.3), one can obtain the following relationship:

$$T_{con} \approx \frac{K(C_{up} + C_{down})}{A_{in}\omega C_{up} + I_c} + \frac{\pi}{2\omega} \tag{5.13}$$

Substituting equations (5.11) and (5.2) in the previous equation, the relation between T_{con} and V_{DC} can be established as follows:

$$T_{con} \approx \frac{-\frac{A_{in}C_{up}R_b}{V_{DC}-V_{BE}} + \frac{\beta 3\pi}{2\omega}}{\frac{A_{in}C_{up}R_b\omega}{V_{DC}-V_{BE}} + \beta} + \frac{\pi}{2\omega} \tag{5.14}$$

Now, it is necessary to identify the relationship between the time that the diode in conducting (T_{con}) and the final equivalent capacitance of the circuit (C_{E_q}).

Firstly, the absolute value of the electric charge and discharge of the matching circuit is derived $(|\Delta Q_{TCVC}|)$ based on the waveforms provided in Fig. 5.3.

$$|\Delta Q_{TCVC}| = |\Delta Q_{D_{ON}}| + |\Delta Q_{D_{OFF}}| \tag{5.15}$$

In the previous equation $|\Delta Q_{D_{ON}}|$ and $|\Delta Q_{D_{OFF}}|$ are the values of the electric charge and discharge of the circuit when the diode is on and off, respectively. From Fig. 5.3, it can be seen that the diode will be on from ωt_{on} to $\pi/2$, with v_{in} decreasing. Therefore, $|Q_{D_{ON}}|$ can be obtained as follows.

$$|\Delta Q_{D_{ON}}| = -\int_{\omega t_{on}}^{\pi/2} C_{on}(-A_{in}sin(\omega t))'d(\omega t) \tag{5.16}$$

$$|\Delta Q_{D_{ON}}| = C_{on}A_{in}(1 - sin(\omega t_{on})) \tag{5.17}$$

Meanwhile, the capacitor is off from $-3\pi/2$ to ωt_{on}, which is divided into two parts: from $-3\pi/2$ to $-\pi/2$, and from $-\pi/2$ to ωt_{on}, with v_{in} increasing and decreasing, respectively. Additionally, the value of the electric charge and discharge caused by the current source i_c must be added to obtain the final $|\Delta Q_{D_{OFF}}|$. This gives the following equations:

$$\begin{aligned}|\Delta Q_{D_{OFF}}| = &\int_{-3\pi/2}^{-\pi/2} C_{off}(-A_{in}sin(\omega t))'d(\omega t) \\ &-\int_{-\pi/2}^{\omega t_{on}} C_{off}(-A_{in}sin(\omega t))'d(\omega t) \\ &+\left(i_c\frac{\omega t_{on} + 3\pi/2}{\omega}\right)\end{aligned} \tag{5.18}$$

$$|\Delta Q_{D_{OFF}}| = C_{off}A_{in}(3 + sin(\omega t_{on})) + \left(i_c\frac{\omega t_{on} + 3\pi/2}{\omega}\right) \tag{5.19}$$

Substituting (5.17) and (5.19) into (5.15), the following result can be obtained:

$$\begin{aligned}|\Delta Q_{TCVC}| = &A_{in}\left[3C_{off} + C_{on} + (C_{off} - C_{on})sin(\omega t_{on})\right] \\ &+ \left(i_c\frac{\omega t_{on} + 3\pi/2}{\omega}\right)\end{aligned} \tag{5.20}$$

Additionally, it is necessary to establish the values for C_{on} and C_{off}.

$$C_{on} = C_{up} \tag{5.21}$$

$$C_{off} = \frac{C_{up}C_{down}}{C_{up} + C_{down}} \tag{5.22}$$

81

Now, one must determine the value of the electric charge and discharge of the equivalent capacitance (C_{E_Q}) on the system.

$$|\Delta Q_{C_{E_q}}| = \int_{-3\pi/2}^{-\pi/2} C_{E_q}(-A_{in}sin(\omega t))'d(\omega t) \tag{5.23}$$

$$- \int_{-\pi/2}^{\pi/2} C_{E_q}(-A_{in}sin(\omega t))'d(\omega t)$$

$$|\Delta Q_{C_{E_q}}| = 4C_{E_q}A_{in} \tag{5.24}$$

Finally, by equating (5.24) and (5.20), one can obtain the relation between C_{E_q} and t_{on}.

$$C_{E_q} = \frac{3C_{off} + C_{on} + (C_{off} - C_{on})sin(\omega t_{on})}{4} + \frac{i_c(t_{on} + 3\pi/2\omega)}{4A_{in}} \tag{5.25}$$

By substituting (5.2) into the previous equation, the following relation can be obtained:

$$C_{E_q} = \frac{3C_{off} + C_{on} + (C_{off} - C_{on})sin(\omega t_{on})}{4}$$
$$+ \frac{\beta(t_{on} + 3\pi/2\omega)(V_{DC} - V_{BE})}{4A_{in}R_b} \tag{5.26}$$

With these equations, the final circuit components can be chosen, so that the system can work at 6.78 MHz, and the final equivalent capacitance can be calculated based on these electronic components.

5.1.2 Built Circuit

Using the previously obtained equations, and the values of components as presented in Table 5.1, the relation between V_{DC} and C_{E_q} can be calculated, simulated and measured (Fig. 5.4).

The calculations were performed as explained in the previous section, while the simulations were made using the Keysight ADS software. The measurements were done utilizing a Keysight DSOX3034A oscilloscope, a RIGOL

DG4102 signal generator, and a Ct-2 current probe. In simulations and measurements, the current on the diode (i_d) is utilized to obtain the conduction time of the diode (T_{con}). Then, this time is used to obtain the equivalent capacitance of the circuit, following Eq. (5.26).

Table 5.1: Parameters of the Matching Circuit

C_{up}	1 nF
C_{down}	680 pF
R_b	12 kΩ
$Diode$	HSMS-2820
$Transistor$	2SD1623S-TD-E
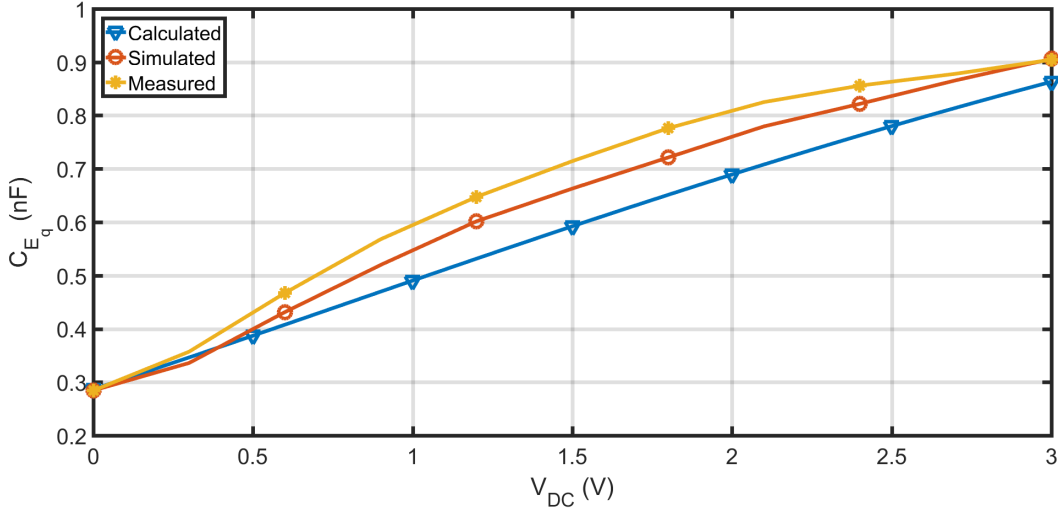
Figure 5.4: Comparison between calculated, simulated and measured results

The previous image demonstrates that the built circuit follows the same curve obtained from simulations and calculations. Small variations are due to the current gain of the transistor (β), which varies among similar components. Furthermore, the fact that the conduction time of the diode is slightly larger in the simulation and measurements also affects the equivalent capacitance of the entire circuit (C_{E_q}), resulting in the presented discrepancies.

From Fig. 5.4 one can observe that the equivalent capacitance to the TCVC varies between 0.3 nF and 0.9 nF, as expected from the provided theory.

83

Additionally, the 10% tolerance of the used capacitors [30] also affects the final results.

The following figure depicts the simulated waveforms of the circuit, using the real models of the components mentioned in Table 5.1, with $V_{DC} = 2.1$ V. It is visible that the main difference between the real case (Fig. 5.5) and the ideal case (Fig. 5.3) is that, in reality, the current on the capacitor C_{down} will not drop instantaneously to zero as soon as the diode starts to conduct. This occurs because of the characteristics of the diode, which creates small variations in T_{con}, also contributing to the capacitance discrepancies previously presented in Fig. 5.4.
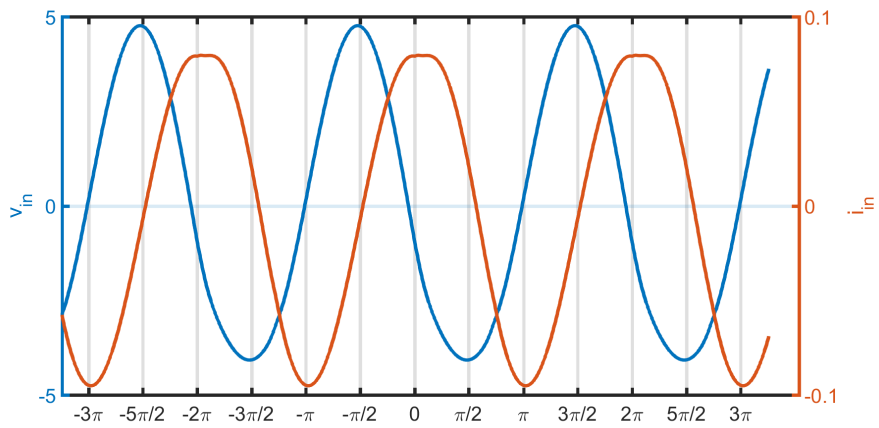
(a) Voltage (v_{in}) and current (i_{in}) provided by the AC source
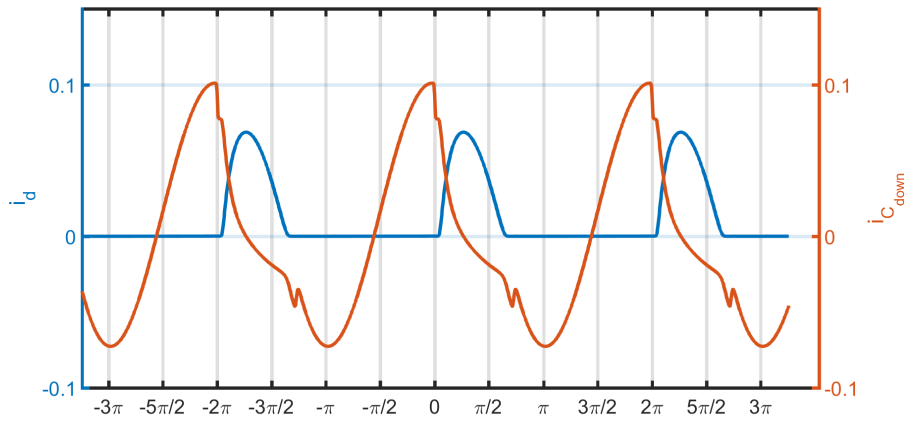
(b) Currents over the diode (i_d) and over the capacitor C_{down} ($i_{C_{down}}$)
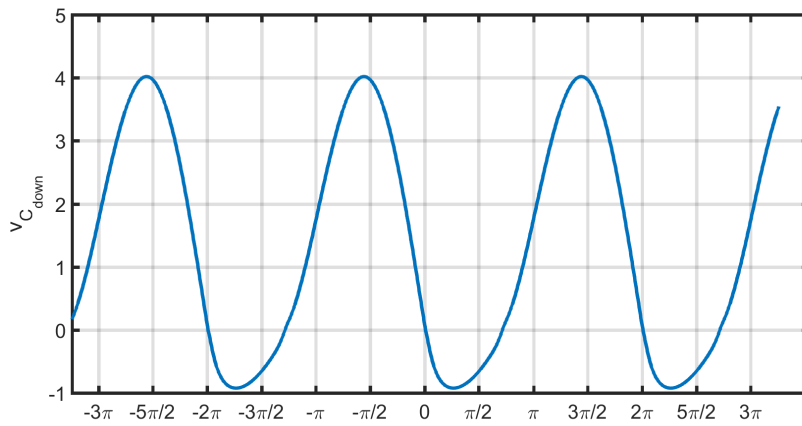
(c) Voltage over the capacitor C_{down} (v_{down})

Figure 5.5: Waveforms of the simulated circuit, with $V_{DC} = 2.1$ V

85

5.2 Adaptive Matching Applied to Regular 2-Coil Inductive Power Transfer

Finally, the designed circuit is applied to an inductive link. Since the designed capacitive resonant single-conductor system cannot operate with enough power to test the adaptive matching circuit, a regular low-Q resonant inductive topology is used instead. This system (as depicted in Fig. 5.6), is comprised of a parallel-parallel tuning configuration of capacitors added to the coils.

The capacitor C_1 on the transmitter coil is kept constant at 1.47 nF, while the receiver capacitor C_2 is placed in parallel with the proposed adaptive matching. The coils have the following characteristics: D = 120 mm, d = 1.29 mm and N = 1, while maintaining 20 mm of distance between Tx and Rx devices. It was decided to place the adaptive circuit on the receiver side of the system due to the fact that the resonance of the receiver coil is the one that dictates the behavior of the entire system [63]. In other words, the peak efficiency of the system always occurs at the resonance of the receiver device.
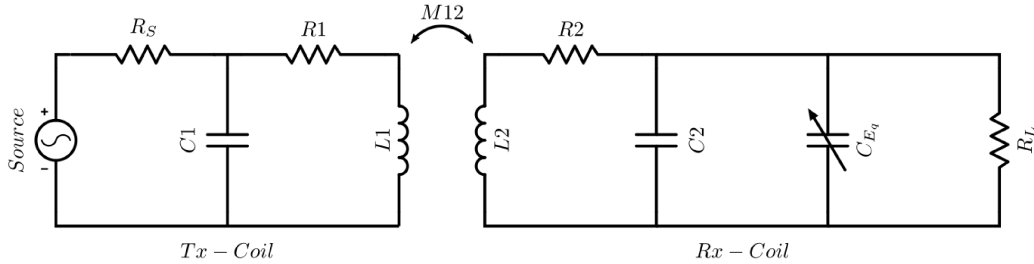
Figure 5.6: Schematic of the adaptive matching circuit applied to a regular low-Q inductive topology

When the voltage V_{DC} of the adaptive matching is varied, the equivalent capacitance C_{E_q} changes. The previous system is simulated with the obtained capacitance range presented in Fig. 5.4, in order to demonstrated its ability to shift the resonant frequency of the entire system, as well as improve the link's efficiency.
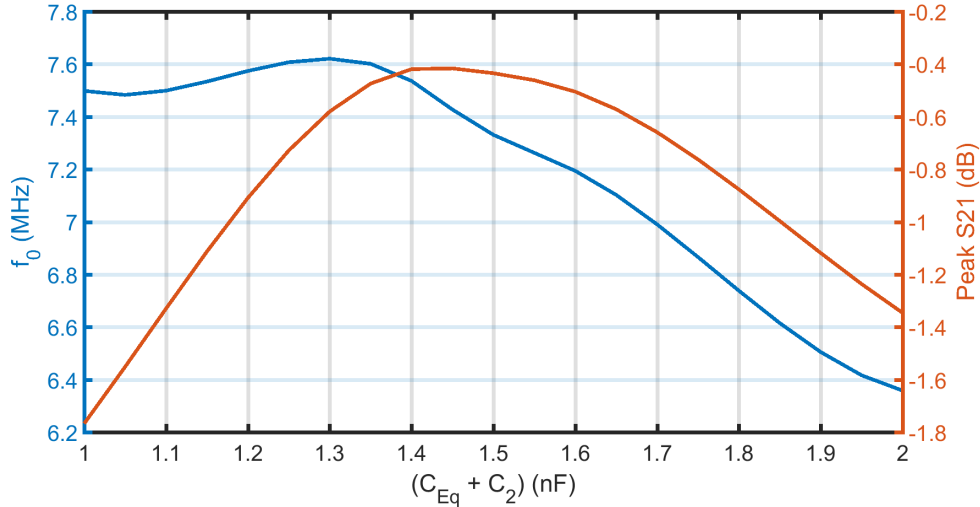
Figure 5.7: Simulated efficiency and resonance of a regular low-Q inductive topology with the proposed adaptive matching circuit

From the previous image it is visible that when the parallel association of C_{E_q} and C_2 reaches values close to 1.47 nF, the efficiency of the link is maximum, since the transmitter and receiver would be working at the same frequency (approximately 7.4 MHz in this case). This means that C_{E_q} would be equal to 0.47 nF, which can be obtained by applying a base voltage of V_{DC} = 0.6 V to the transistor of the adaptive matching circuit.

5.3 Chapter Summary

In this chapter, an adaptive matching circuit is proposed using transistor-controlled variable capacitors. In this topology, a capacitor is added in parallel to a transistor. As the base voltage of the transistor increases, the time that this component is conducting also rises, as long as it is working on its active region. By changing the duration that the transistor's conduction, the amount of time that the capacitor has current passing through it also varies, which modifies the overall capacitance of the circuit.

Firstly, equations are derived in order to determine the relationship between the base voltage of the transistor and the equivalent capacitance of the system. Then, simulations are performed to confirm the calculations. Finally, the circuit is built and measured in reality, demonstrating that such circuit is

capable of varying its capacitance in the desired way.

Furthermore, the adaptive matching circuit is applied to a regular 2-coil IPT system, in order to show that this circuit is able to change the resonance of the inductive link, by varying the resonant capacitor of the receiver coil. Consequently, improving the efficiency of the power transmission.

Chapter 6

Conclusion

Current existing inductive and capacitive power transfer technologies lack the ability to properly power a device with a solid metallic case. Therefore, this thesis proposes a mixture of these methods, combined with a single-conductor topology, in order to allow such feat. Each of these technologies is briefly introduced in Chapter 1, explaining why they are not suitable alone to charge an electronic device with a metallic cover. Furthermore, a first overview of the proposed system (the capacitive resonant single-conductor) is presented in the same chapter.

In Chapter 2 each component of the capacitive resonant single-conductor system is individually analyzed in details. This chapter contains all the justifications for the design decisions made in this project. Moreover, the system utilizes a high-Q resonant inductive topology composed of one coil and one resonator on each side of the system. These parts will be responsible to efficiently transfer the power to the capacitive resonant single-conductor structure.

The capacitive resonant single-conductor structure, as a whole, is finally analyzed in Chapter 3. All parameters of the final system are theoretically deducted, simulated and measured. It is visible that the designed system is able to provide significantly high power transfer efficiency, in theory. However, because extremely large inductors are required to achieve resonance, the ESR that they add to the system is responsible for drastically decreasing the efficiency in reality.

Chapter 4 contains possible variations to the system presented in Chapter

3. The distance between capacitive plates is analyzed, as well as the use of asymmetric plates in the system. Since the current version was not able to provide high efficiency power transfer when the transmitter plate was much larger than the receiver plate, a new topology is presented. The transmitter plate is fragmented into multiple smaller Tx-Cells, allowing the electric field to pass through the middle of the plate. Additionally, multiple compensation inductors were also tested, willing to achieve resonance between the receiver unit and only the transmitter cells that are directly positioned beneath it.

Finally, in Chapter 5, an adaptive matching circuit is proposed, so that the system would be able to self-adjust its resonance in the future, in order to compensate for impedance variations. The proposed circuit is composed of a transistor-controlled variable capacitor. This circuit provides a simpler and smaller design, when compared to regular switching and varactor approaches, due to the fact that it can vary the overall capacitance of the system by changing the amount of time that the transistor is conducting. This is performed by changing the base voltage of such component, which allows a linear capacitance variation in the circuit.

6.1   Future Work

Although the entire analysis of a WPT system capable of transmitting power to an electronic device with a metallic cover was performed, it is visible that the proposed system requires improvements in order to be recommendable for high power commercial applications. This is due to two main concerns: the significantly high electric field intensity around the system, and the impressive losses added by the ESR of the required compensation inductors in the system.

In the future, reductions in the electric field intensity can be performed by changing some parameters of the proposed system. For example, if the capacitance between the open-ends of the fragments of resonator increases, this field will be reduced. Additionally, shielding techniques might also be applied to the system.

Furthermore, in order to reduce the ESR added by the compensation in-

ductors, smaller inductances are required. To achieve this, coils with higher self-inductances can be designed, so that the single-conductor structure will not require such high compensation values in order to resonate at the desired frequency. Also, some techniques may be employed to adjust the capacitance between the plates, to achieve this goal as well.

Even though the system outlined in this thesis has improvements to be made, it is a remarkable advance in the current field, by providing a system capable of powering electronic devices with a metallic embodiment, and by allowing significant misalignment between transmitter and receiver units.

References

[1] Statista, *Semiconductor sales revenue worldwide from 1987 to 2019 (in billion u.s. dollars)*, 2018.   1

[2] X. Lu, P. Wang, D. Niyato, D. I. Kim, and Z. Han, "Wireless charging technologies: Fundamentals, standards, and network applications," *IEEE Comm. Surv. & Tut.*, vol. 18, no. 2, pp. 1413–1452, Nov. 2015.   1

[3] R. Jegadeesan, Y. Guo, and M. Je, "Overcoming coil misalignment using magnetic fields of induced currents in wireless power transmission," *IEEE MTT-S IMS Digest*, Jun. 2012.   1

[4] T. Kawajiri and H. Ishikuro, "Open loop dynamic transmitter voltage scaling for fast response and wide load range power efficient wpt system," *IEEE MTT-S IMS Digest*, Jun. 2017.   1

[5] M. P. Theodoridis, "Effective capacitive power transfer," *IEEE Trans. Power Electron.*, vol. 27, no. 12, pp. 665–675, Dec. 2012.   1, 27, 43

[6] H. Zhang, F. Lu, H. Hofmann, W. Liu, and C. C. Mi, "Six-plate capacitive coupler to reduce electric field emission in large air-gap capacitive power transfer," *IEEE Trans. Power Electron.*, vol. 33, no. 1, pp. 665–675, Jan. 2018.   1, 26, 27

[7] R. Johari, J. V. Krogmeier, and D. J. Love, "Analysis and practical considerations in implementing multiple transmitters for wireless power transfer via coupled magnetic resonance," *IEEE Trans. Ind. Electron.*, vol. 61, no. 4, pp. 1774–1783, Apr. 2014.   1

[8] L. Zhao, D. J. Thrimawithana, and U. K. Madawala, "Hybrid bidirectional wireless ev charging system tolerant to pad misalignment," *IEEE Trans. Ind. Electron.*, vol. 64, no. 9, pp. 7079–7086, Sep. 2017.   1

[9] H. Feng, T. Cai, S. Duan, X. Zhang, H. Hu, and J. Niu, "A dual-side detuned series-series compensated resonant converter for wide charging region in wireless power transfer system," *IEEE Trans. Ind. Electron.*, vol. 65, no. 3, pp. 2177–2188, Mar. 2018.   1

[10] F. Lu, H. Zhang, H. Hofmann, and C. Mi, "A double-sided lclc-compensated capacitive power transfer system for electric vehicle charging," *IEEE Trans. Power Electron.*, vol. 30, no. 11, pp. 6011–6014, Nov. 2015.   1

92

[11] S. Lee, G. Jung, S. Shin, Y. Kim, B. Song, J. Shin, and D. Cho, "The optimal design of high-powered power supply modules for wireless power transferred train," *2012 Electrical Systems for Aircraft, Railway and Ship Propulsion*, pp. 1–4, Oct. 2012.   2

[12] X. Shi, C. Qi, and S. Ye, "Effects of obstacle sizes on wireless power transfer via magnetic resonance coupling," *2015 IEEE PELS Workshop on Emerging Technologies: Wireless Power (2015 WoW)*, pp. 1–5, Jun. 2015.   2

[13] N. Sakai, D. Itokazu, Y. Suzuki, S. Sakihara, and T. Ohira, "One-kilowatt capacitive power transfer via wheels of a compact electric vehicle," *2016 IEEE Wireless Power Transfer Conference (WPTC)*, pp. 1–3, May 2016.   2, 27

[14] T. Komaru and H. Akita, "Positional characteristics of capacitive power transfer as a resonance coupling system," *2013 IEEE Wireless Power Transfer (WPT)*, pp. 218–221, May 2013.   2

[15] S. V. de C. de Freitas, F. C. Domingos, R. Mirzavand, A. Maunder, P. Naseri, and P. Mousavi, "A novel method for data and power transmission through metallic structures," *IEEE Trans. Ind. Electron.*, vol. 64, no. 5, pp. 4027–4036, May 2017.   3, 28, 29, 33, 53

[16] S. V. de C. de Freitas, A. Maunder, F. C. Domingos, and P. Mousavi, "Method and system for wireless and single-conductor power and data transmission," *IEEE Wireless Power Transfer Conf. (WPTC)*, May 2016.
       3, 28, 29, 33

[17] G. Goubau, "Single-conductor surface-wave transmission lines," *Proc. of the IRE*, vol. 39, no. 6, pp. 619–624, Jun. 1951.   3, 28, 33

[18] A. Sharma, A. T. Hoang, and M. S. Reynolds, "A coplanar vivaldi-style launcher for goubau single-wire transmission lines," *IEEE Ant. and Wir. Prop. Letters*, vol. 16, pp. 2955–2958, Sep. 2017.   3

[19] S. M. Amjadi and K. Sarabandi, "A compact single conductor transmission line launcher for telemetry in borehole drilling," *IEEE Trans. Geoscience and Rem. Sens.*, vol. 55, no. 5, pp. 2674–2681, May 2017.   3, 28, 29

[20] B. L. Cannon, J. F. Hoburg, D. D. Stancil, and S. C. Goldstein, "Magnetic resonant coupling as a potential means for wireless power transfer to multiple small receivers," *IEEE Trans. Power Electron.*, vol. 24, no. 7, pp. 1819–1825, Jul. 2009.   8

[21] H. Ali, T. J. Ahmad, and S. A. Khan, "Mathematical modeling of an inductive link for optimizing efficiency," *2009 IEEE Symposium on Industrial Electronics & Applications*, pp. 831–835, 2009.   9–11

93

[22] C.-C. Hou, B.-Y. Chen, K.-J. Lee, H.-Y. Ku, P.-C. Chang, and T.-J. Chen, "Resonant and non-resonant inductive power transfer systems based on planar spiral coils," *2017 IEEE 3rd International Future Energy Electronics Conference and ECCE Asia (IFEEC 2017 - ECCE Asia)*, pp. 428–433, Jun. 2017.   9

[23] G. Simard, M. Sawan, and D. Massicotte, "High-speed oqpsk and efficient power transfer through inductive link for biomedical implants," *IEEE Transactions on Biomedical Circuits and Systems*, vol. 4, no. 3, pp. 192–200, Jun. 2010.   10

[24] R. Jegadeesan and Y. X. Guo, "A study on the inductive power links for implantable biomedical devices," *2010 IEEE Antennas and Propagation Society International Symposium*, pp. 1–4, Jul. 2010.   10

[25] C. Yang and C. Yang, "Analysis of inductive coupling coils for extending distances of efficient wireless power transmission," *2013 IEEE MTT-S International Microwave Workshop Series on RF and Wireless Technologies for Biomedical and Healthcare Applications (IMWS-BIO)*, pp. 1–3, Dec. 2013.   11

[26] D. V. Wageningen and T. Staring, "The qi wireless power standard," *14th International Power Electronics and Motion Control Conference (EPE/PEMC)*, 2010.   12

[27] A. Alliance, "A4wp wireless power transfer system baseline system specification (bss) v 1.2.1," 2014.   12, 33

[28] F. W. Grover, *Inductance Calculations: Working Formulas and Tables.* New York, NY, USA: Dover, 1946.   12

[29] A. Kumar, W. A. Edelstein, and P. A. Bottomley, "Noise figure limits for circular loop mr coils," *Magn. Reson. Med.*, vol. 61, pp. 1201–1209, 2009.   13, 27

[30] A. RF, "Rf/microwave mlc's - sq series ultra low esr mlc," *Datasheet*, 2017.   15, 19, 53, 84

[31] A. L. Bloom, D. J. Innes, R. C. Rempel, and K. A. Ruddock, "Octagonal coil systems for canceling the earth's magnetic field," *Journal of Applied Physics*, vol. 36, no. 8, pp. 2559–2565, Aug. 1965.   15

[32] A. P. Sample, D. A. Meyer, and J. R. Smith, "Analysis experimental results and range adaptation of magnetically coupled resonators for wireless power transfer," *IEEE Trans. Ind. Electron.*, vol. 58, no. 2, pp. 544–554, Feb. 2011.   16

[33] W. Niu, J. Chu, W. Gu, and A. Shen, "Exact analysis of frequency splitting phenomena of contactless power transfer systems," *IEEE Transactions on Circuits and Systems I: Regular Papers*, vol. 60, no. 6, pp. 1670–1677, Jun. 2013.   16

[34] H. Kudo, K. Ogawa, N. Oodachi, N. Deguchi, and H. Shoki, "Detection of a metal obstacle in wireless power transfer via magnetic resonance," *2011 IEEE 33rd International Telecommunications Energy Conference (INTELEC)*, pp. 1–6, Oct. 2011. 26, 44

[35] C. Liu, A. P. Hu, G. A. Covic, and N.-K. C. Nair, "Comparative study of ccpt systems with two different inductor tuning positions," *IEEE Trans. Power Electron.*, vol. 27, no. 1, pp. 294–306, Jan. 2012. 27, 43

[36] H. Zhang, F. Lu, H. Hofmann, W. Liu, and C. C. Mi, "A four-plate compact capacitive coupler design andlcl-compensated topology for capacitive power transfer in electric vehicle charging application," *IEEE Transactions on Power Electronics*, vol. 31, no. 12, pp. 8541–8551, Dec. 2016. 27

[37] G. Goubau, "Surface waves and their application to transmission lines," *J. Applied Physics*, vol. 21, pp. 1119–1128, 1950. 28

[38] A. Ishimaru, J. D. Rockway, and L. Seong-Woo, "Sommerfeld and zenneck wave propagation for a finitely conducting one-dimensional rough surface," *IEEE Trans. Antennas Propag.*, vol. 48, pp. 1475–1484, 2000. 28

[39] E. H. Scheibe, B. G. King, and D. L. V. Zeeland, "Loss measurements of surface wave transmission lines," *J. Applied Physics*, vol. 25, pp. 790–797, 1954. 28

[40] S. R. Rengarajan and J. E. Lewis, "The elliptical surface wave transmission line," *IEEE Trans. Microw. Theory Techn.*, vol. 28, pp. 1089–1095, 1980. 28

[41] M. King and J. C. Wiltse, "Surface-wave propagation on coated or uncoated metal wires at millimeter wavelengths," *IRE Trans. Antennas Propag.*, vol. 10, pp. 246–254, 1962. 28

[42] T. Zarifi, K. Moez, and P. Mousavi, "Impedance matching network for ground eliminated open-ended resonant coil structure in distributed wireless power transmission systems," *IET Sci. Measur. Tech.*, vol. 11, no. 7, pp. 856–860, Oct. 2017. 28, 29

[43] C. W. V. Neste, J. E. Hawk, A. Phani, J. A. J. Backs, R. Hull, T. Abraham, S. J. Glassford, A. K. Pickering, and T. Thundat, "Single-contact transmission for the quasi-wireless delivery of power over large surfaces," *Wireless Power Transfer*, vol. 1, pp. 75–82, 2014. 28, 29

[44] T. Sun, X. Xie, G. Li, Y. Gu, X. Li, and Z. Wang, "A wireless energy link for endoscopy with end-fire helix emitter and load-adaptive power converter," *2010 IEEE Asia Pacific Conference on Circuits and Systems*, pp. 32–35, 2010. 28, 29

[45] A. Kurs, A. Karalis, R. Moffatt, J. D. Joannopoulos, P. Fisher, and M. Soljacic, "Wireless power transfer via strongly coupled magnetic resonances," *Science*, vol. 317, pp. 83–86, Jul. 2007. 28, 29, 54

[46] S. V. de C. de Freitas, F. C. Domingos, R. Mirzavand, and P. Mousavi, "Contactless power transfer using capacitive resonant single-conductor structure," *Wireless Power Transfer Conference (WPTC)*, 2018.   32

[47] J. C. Maxwell, *A Treatise on Electricity & Magnetism*, 3rd ed. New York, NY, USA: Dover, 1954, vol. 2.   36, 38

[48] L. V. King, "On some new formulæ for the numerical calculation of the mutual induction of coaxial circles," *Proceedings of the Royal Society of London A: Mathematical, Physical and Engineering Sciences*, vol. 100, no. 702, pp. 60–66, 1921.   37

[49] X. Nan and C. R. Sullivan, "An improved calculation of proximity-effect loss in high-frequency windings of round conductors," *IEEE 34th Annual Conference on Power Electronics Specialist, 2003. PESC '03.*, vol. 2, pp. 853–860, Jun. 2003.   38

[50] R. G. Medhurst, "H.f. resistance and self-capacitance of single-layer solenoids," *GEC Research Labs.*, pp. 80–92, Mar. 1947.   46

[51] M. Rao and K. Sarabandi, "A tunable, high gain, very low-profile composite monopole antenna for low-frequency applications," *IEEE Transactions on Antenna and propagation*, vol. 66, no. 7, pp. 3286–3294, Jul. 2018.   50

[52] Macom, "Mabaes0060 - rf 1:1 flux coupled transformer," *Datasheet*, vol. 8, 2013.   50

[53] W. F. Andress and D. Ham, "Standing wave oscillators utilizing wave-adaptive tapered transmission lines," *IEEE Journal of Solid-State Circuits*, vol. 40, no. 3, pp. 638–651, Mar. 2005.   53

[54] M. C. Hegg and A. V. Mamishev, "Influence of variable plate separation on fringing electric fields in parallel-plate capacitors," *Conference Record of the 2004 IEEE International Symposium on Electrical Insulation*, pp. 384–387, Sep. 2004.   54

[55] G. Zhu and R. D. Lorenz, "Achieving low magnetic flux density and low electric field intensity for an inductive wireless power transfer system," *2017 IEEE Energy Conversion Congress and Exposition (ECCE)*, pp. 4022–4029, Oct. 2017.   54

[56] M. P. Biginton, A. P. Hibbins, J. R. Sambles, and I. J. Youngs, "Microwave transmission through an array of ring slots in a metal sheet capped with concentric metal rings," *IEEE Transactions on Antennas and Propagation*, vol. 61, no. 1, pp. 458–461, Jan. 2013.   64

[57] M. G. E. Din, B. Geck, and H. Eul, "Adaptive matching for efficiency enhancement of switching mode and nonlinear microwave power amplifiers," *2010 IEEE Radio and Wireless Symposium (RWS)*, pp. 192–195, Jan. 2010.   74

[58] D. G. Seo, S. H. Ahn, J. H. Kim, W. S. Lee, S. C. Khang, S. C. Chae, and J. W. Yu, "Power transfer efficiency for distance-adaptive wireless power transfer system," *2018 International Applied Computational Electromagnetics Society Symposium (ACES)*, pp. 1–2, Mar. 2018. 74

[59] F. Rodes, M. Zhang, R. Deniéport, and X. Wang, "Optimization of the power transfer through human body with an auto-tuning system using a synchronous switched capacitor," *IEEE Transactions on Circuits and Systems II: Express Briefs*, vol. 62, no. 2, pp. 129–133, Feb. 2015. 74

[60] Y. Jung and B. Lee, "Design of adaptive optimal load circuit for maximum wireless power transfer efficiency," *2013 Asia-Pacific Microwave Conference Proceedings (APMC)*, pp. 1221–1223, Nov. 2013. 74

[61] S. Rezayat, C. Baylis, R. J. Marks, and E. Viveiros, "Measurement of load-pull performance in the power smith tube using a tunable varactor matching network," *2017 Texas Symposium on Wireless and Microwave Circuits and Systems (WMCS)*, pp. 1–4, Mar. 2017. 74

[62] J. Tian and A. P. Hu, "A dc-voltage-controlled variable capacitor for stabilizing the zvs frequency of a resonant converter for wireless power transfer," *IEEE Transactions on Power Electronics*, vol. 32, no. 2, pp. 2312–2318, Mar. 2017. 75, 76

[63] Y. H. Sohn, B. H. Choi, E. S. Lee, G. C. Lim, G. Cho, and C. T. Rim, "General unified analyses of two-capacitor inductive power transfer systems: Equivalence of current-source ss and sp compensations," *IEEE Transactions on Power Electronics*, vol. 30, no. 11, pp. 6030–6045, Nov. 2015. 86